



저작자표시-비영리-변경금지 2.0 대한민국

이용자는 아래의 조건을 따르는 경우에 한하여 자유롭게

- 이 저작물을 복제, 배포, 전송, 전시, 공연 및 방송할 수 있습니다.

다음과 같은 조건을 따라야 합니다:



저작자표시. 귀하는 원저작자를 표시하여야 합니다.



비영리. 귀하는 이 저작물을 영리 목적으로 이용할 수 없습니다.



변경금지. 귀하는 이 저작물을 개작, 변형 또는 가공할 수 없습니다.

- 귀하는, 이 저작물의 재이용이나 배포의 경우, 이 저작물에 적용된 이용허락조건을 명확하게 나타내어야 합니다.
- 저작권자로부터 별도의 허가를 받으면 이러한 조건들은 적용되지 않습니다.

저작권법에 따른 이용자의 권리는 위의 내용에 의하여 영향을 받지 않습니다.

이것은 [이용허락규약\(Legal Code\)](#)을 이해하기 쉽게 요약한 것입니다.

[Disclaimer](#)

공학박사 학위논문

**Magnetic Vortex Based Magnons in One-  
dimensional Periodic Arrays of Soft  
Ferromagnetic Nanodisks**

일차원 강자성 나노 디스크 배열구조에서 자기소  
용돌이 기반의 마그논 연구

2014 년 2 월

서울대학교 대학원

공과대학 재료공학부

한 동 수

**Magnetic Vortex Based Magnons in One-  
dimensional Periodic Arrays of Soft  
Ferromagnetic Nanodisks**

**A THESIS  
SUBMITTED TO THE FACULTY OF SEOUL  
NATIONAL UNIVERSITY  
BY**

**Dong-Soo Han**

Supervised by  
**Prof. Sang-Koog Kim**

**IN PARTIAL FULFILLMENT OF THE  
REQUIREMENTS FOR THE DEGREE OF DOCTOR  
OF PHILOSOPHY**

**February 2014**

*Department of Materials Science and Engineering  
Graduate School  
Seoul National University*

**Magnetic Vortex Based Magnons in  
One-dimensional Periodic Arrays of  
Soft Ferromagnetic Nanodisks**

지도 교수 김상국

이 논문을 공학박사 학위논문으로 제출함  
2014년 02월

서울대학교 대학원  
재료공학부  
한 동 수

한동수의 박사 학위논문을 인준함  
2014년 01월

위원장 \_\_\_\_\_ 황 철 성



부위원장 \_\_\_\_\_ 김 상 국



위 원 \_\_\_\_\_ 김 미 영



위 원 \_\_\_\_\_ 한 승 우



위 원 \_\_\_\_\_ 민 병 철



# **Abstract**

## **Magnetic Vortex Based Magnons in One-dimensional Periodic Arrays of Soft Ferromagnetic Nanodisks**

Dong-Soo Han

Department of Materials Science and Engineering  
Seoul National University

Lattice vibration modes are collective excitations in periodic arrays of atoms or molecules. These modes determine novel transport properties in solid crystals. Analogously, in periodical arrangements of magnetic vortex-state disks, collective vortex motions and vortex gyration mediated signal transport have been predicted. In this thesis, in particular, we focus on magnetic vortex-based magnonic behavior in one-dimensional (1D) periodic arrays of soft ferromagnetic nanodisks, and also provide a foundation for manipulation of the vortex-gyration based signal transfer.

We, for the first time, experimentally demonstrate wave modes of collective vortex gyration in 1D periodic arrays of magnetic disks by using time-resolved scanning transmission x-ray microscopy. The observed modes are interpreted based on micromagnetic simulation and numerical calculation of coupled Thiele equations. Dispersion of the modes is found to be strongly affected by vortex polarization, chirality ordering, dimensional

parameters of the constituent disk, and interdistance between neighboring disks.

The effects of change in the primitive unit cells of 1D vortex arrays on collective vortex-gyration dispersion are also investigated through micromagnetic numerical and analytical calculations. As the primitive basis, we consider alternating constituent materials (NiMnSb vs. Permalloy) and alternating dimensions including constituent disk diameter and thickness. In the simplest case, that of one vortex-state disk of given dimensions and single material in the primitive cell, only a single branch of collective vortex-gyration dispersion appears. By contrast, two constituent disks' different alternating materials, thicknesses and diameters yield characteristic two-branch dispersions the band widths and gaps of which differ in each case.

Furthermore, we propose and demonstrate an efficient way to control coupled-vortex dynamics by means of an external perpendicular bias field. The results reveal that the dynamics properties, such as the eigenfrequencies and dispersion relations, of coupled-vortex arrays can be manipulated by the strength and direction of bias field. More interestingly, for antiparallel polarization ordering case, a single branch splits into two distinct branches under the non-zero bias field, and thus resulting in bandgap opening.

This substantial work offers potential implementation into vortex- gyration based information processing devices with the advantages of endless endurance of switchable vortex states and vortex-gyration propagation, low-power signal input through resonant excitation of vortex gyrations, and low energy dissipation.

**Keywords: magnetic vortex, vortex dynamics, coupled dynamics, spin dynamics, magnonic crystal, spin waves**

**Student number: 2008-20696**

# Contents

<b>Abstract .....</b>	<b>ii</b>
<b>Contents.....</b>	<b>v</b>
<b>List of Figures .....</b>	<b>ix</b>
<b>List of Tables .....</b>	<b>xii</b>
<b>Chapter 1 Introduction .....</b>	<b>1</b>
<b>Chapter 2 Research Background .....</b>	<b>5</b>
2.1. Micromagnetics .....	6
2.1.1. Micromagnetic Energy .....	6
2.1.2 Magnetic Equilibrium and Brown's Equations .....	12
2.1.3 Equation of motion of magnetization .....	14
2.2. Magnetic Vortex.....	17
2.2.1 What is a Magnetic Vortex?.....	17
2.2.2 Dynamics of a Magnetic Vortex .....	23
2.2.3 Coupled Magnetic Vortex .....	25
<b>Chapter 3 Method.....</b>	<b>29</b>
3.1 X-ray Magnetic Imaging Technique.....	30
3.1.1 X-ray Magnetic Circular Dichroism (XMCD) .....	31
3.1.2 Full-field magnetic transmission soft X-ray microscopy (MTXM).....	34

3.1.3 Scanning Transmission soft X-ray Microscopy (STXM).....	37
3.1.4 Time-resolved measurement (pump-probe technique).....	39
3.3 Micromagnetic simulations .....	40
<b>Chapter 4 Collective Vortex Oscillation Modes in a 1D chain</b>	
<b>Consisting of a Single-component Constituents.....</b>	<b>42</b>
4.1 Sample preparation and experimental setup.....	43
4.2 Vortex-core gyration propagation along dipolar-coupled disks.....	46
4.3 Numerical calculation of $N$ coupled Thiele equations for $N$ coupled vortex gyrations .....	49
4.4 Discrete wave modes of collective vortex gyration in finite number of disks.....	53
4.4.1 Discrete wave modes for $N$ coupled-vortex dynamics.....	53
4.4.2 Discrete wave modes in real sample.....	57
4.5 Dispersion relations of collective vortex gyration in 1D arrays of finite number of disks .....	61
4.6 Dispersion relation in 1D magnetic vortex-based magnonic crystal of infinite or semi infinite number of disks .....	65
4.7 Phase relation of the net in-plane magnetizations between the NN disks and dispersion relations.....	70
<b>Chapter 5 Collective Vortex Oscillation Modes in a 1D Chain</b>	
<b>Consisting of Bi-component Constituents .....</b>	<b>73</b>

5.1 Model geometry.....	74
5.2 Vortex-core gyration propagation in the 1D chain consisting of bi-component constituents .....	77
5.3 Dispersion relations in the 1D chain consisting of Bi-component Constituents .....	80
5.3.1 Micromagnetic simulations results.....	80
5.3.2 Analytical derivation of dispersion relations .....	83
5.4 Spatial profiles of coupled core motions for specific collective gyration modes .....	86
5.5 Different types of basis and their dispersion relations .....	89
<b>Chapter 6 Bias field control of <math>N</math>-body coupled vortex oscillation.....</b>	<b>92</b>
6.1 Perpendicular bias field effect on an isolated disk .....	94
6.2 Dipolar interaction and interaction integrals under the influence of perpendicular bias field .....	97
6.3 Normal modes in two coupled vortex oscillator under the influence of perpendicular bias field .....	100
6.4 Dispersion relation of 1D arrays of coupled vortex oscillators under the influence of perpendicular bias field .....	107
<b>Chapter 7 Summary .....</b>	<b>110</b>
<b>Appendix A. Experimental Setup.....</b>	<b>112</b>

A.1 Thin film deposition .....	112
A.2 Lithography .....	114
A.3 Electrical measurement setup .....	118
<b>Bibliography.....</b>	<b>122</b>
<b>Publication List.....</b>	<b>131</b>
<b>Patent List .....</b>	<b>135</b>
<b>International Conference Presentations.....</b>	<b>136</b>
<b>Domestic Conference .....</b>	<b>139</b>

## List of Figures

2.1	Schematic illustration of magnetization precession motion .....	16
2.2	Schematic illustration of the magnetic vortex structure .....	19
2.3	Direct measurements of a magnetic vortex structure .....	20
2.4	Energetically equivalent four different states of a magnetic vortex according to the vortex core polarization and the chirality .....	22
2.5	Experimental demonstration of dipolar coupled vortex dynamics .....	28
3.1	Schematic illustration for X-ray magnetic circular dichroism spectroscopy and absorption spectra at the Co $L_{2,3}$ edge .....	32
3.2	Schematics of the full-field magnetic transmission soft X-ray microscope (MTXM) at ALS BL 6.1.2 .....	36
3.3	Photograph of experimental setup of MTXM at ALS BL 6.1.2 .....	36
3.4	Schematic illustration of the scanning transmission X-ray microscope (STXM) .....	38
4.1	SEM image and magnetization contrast for five-disk array .....	45
4.2	Experimentally measured and simulated time-resolved trajectories of gyrating vortices .....	48

4.3	Numerically calculated discrete vortex-gyration modes in $N$ -disk arrays .....	56
4.4	Discrete vortex-gyration modes in the real sample .....	60
4.5	Dispersion relations of collective vortex-gyration modes in a chain of five Py disks .....	64
4.6	Dispersion curves for parallel and antiparallel ordering of polarization and chirality as well as characteristic dynamic dipolar interaction energy density for $k=0$ and $k=k_{BZ}$ cases .....	69
5.1	Model geometry for micromagnetic simulation of 1D chains comprised of a single and alternating materials .....	76
5.2	Propagation of vortex gyration gyrating in 1D chains comprised of a single and alternating materials .....	79
5.3	Dispersion relations of 1D chains comprised of a single and alternating materials .....	82
5.4	Spatial profiles of coupled core motions for specific collective gyration modes .....	88
5.5	Dispersion relations of 1D chains comprised of alternating dimensions .....	91
6.1	Perpendicular field effect on an isolated vortex-state disk .....	96
6.2	Schematic representation of contrasting response to the	

	perpendicular bias field in the coupled-vortex system .....	102
6.3	The angular frequency difference $\Delta\omega$ (top panel) and the energy exchange rate $\tau_{\text{ex}}$ (bottom panel) in dipolar-coupled two vortex oscillator .....	106
6.4	Dispersion relations of collective vortex gyration in 1D chain under the influence of perpendicular field .....	109
A.1	Picture of cluster chamber system .....	113
A.2	Scanning electron measurement and Transmission electron measurement images of disk-shaped patterning .....	117
A.3	Dispersion relations of collective vortex gyration in 1D chain under the influence of perpendicular field .....	113
A.4	Photograph of probe station .....	120
A.5	Photograph of DC and microwave electronics .....	121

## List of Tables

A.1	Typical electron-beam lithography procedure for a disk-shaped patterning .....	116
-----	---	-----

# Chapter 1

## Introduction

Recent advances in nano-lithography technologies[1, 2] as well as growth techniques of high quality thin films have renewed interests in research on nanomagnetism. In parallel to these developments, the discovery of giant magneto-resistance (GMR)[3, 4], tunnel magneto-resistance (TMR)[5, 6] and spin transfer torque (STT)[7, 8] effect has launched a new era of spintronics[9-11]. The spintronics, refers to the electronics correlated with spin degree of freedom of electrons, have attracted particular attention, owing to possible implementations in future information storage[12] and processing devices[13, 14] with high-store density, faster data-processing speed, and less power consumption. A significant number of spintronics devices, for example, the magnetic domain-motion wall race-track memory[15, 16], magnetic random access memory[17, 18], and magneto-resistive head in hard disk drivers[19, 20], have been proposed and demonstrated intensively during past decades. However, these spintronic devices have common limitations of conventional electronics in that the spintronics is based on the movement of spin, like charge flow.

Collective spin excitations (spin waves) in nano-scale magnetic elements have grown in popularity as a relatively recent research topic[1, 21, 22]. Spin waves, of which behaviors are analogous to lattice vibrations in solid-state materials, has been proposed as a promising candidates for future information-signal processing technologies[23-29]. Information in magnonics is carried by collective excitation of localized spin rather than the flow of electron as in conventional electronics and spintronics. This technological advantage led to a rich variety of fundamental and applied spin-wave studies.

In particular, collective spin excitation in artificial metastructures with a spatially periodic variation of magnetic parameters, called as magnonic crystals (MCs), have been intensively studied from the both fundamental and technical point of view. In these MCs, like conventional metastructures, i.e., photonic crystals, phononic crystals, and plasmonic crystals, magnonic band structures including band widths and gaps can, in principle, be controlled and varied through their constituent materials and the isolated elements' dimensions and separation distance. A wide variety of MCs, such as one-dimensional (1D) strips[30-38], two-dimensional (2D) arrays of magnetic nanoelements[39-41], and anti-dot lattices of periodic holes having a circular or rectangular shape in 2D continuous films[21, 42], has been proposed and explored.

Very recently, interest in the information-signal transfer[43-56] and logic operation[57] via stimulated vortex gyration through dipolar interaction between physically separated magnetic disks is rapidly growing, after Shibata *et al*'s first intriguing finding on dynamics of dipolar-coupled vortices in magnetic disks[43]. The information processing based on the mechanism has new functionalities and advantages with respect to the conventional magnon-based signal transferring method, thanks to the possibility of selective manipulation of its magnetic configurations[49, 51, 52, 54], i.e., polarization( $p$ ) and chirality( $C$ ), through an external magnetic field or current. Also, in contrast to the conventional magnon-based signal transferring system, where a static external magnetic field is usually required to obtain a saturated magnetic ground state, the vortex configuration can be easily achieved in the absence of the external field, since a magnetic vortex forms by nature in submicron sized magnetic disk. In order to realize the vortex-gyration-based information devices, one should be able to control the signal, and this can be accomplished by designing magnonic band structures with periodic 1D or 2D arrays of magnetic disks, which is analogous to the conventional MCs. In this case, the magnonic band structures including band widths and gaps can, in principle, be controlled and varied through their constituent materials and the isolated elements' dimensions and separation distance as well as its magnetic configurations.

In this thesis, we address the main achievements in collective vortex-gyration modes in a variety of 1D magnetic arrays with the magnetic vortex state and their control by means of the constituent materials of those structures, the dimensions of the isolated dots, their separation distance, magnetic configurations as well as an external magnetic field.

This thesis is organized as follows. In Chapter 2, the theoretical background on micromagnetics and historical reviews on magnetic vortex structure will be provided. In Chapters 3, we deal with the experimental methods and the micromagnetic simulation tool, used for investigation of dynamics of dipolar-coupled magnetic vortex. In Chapter 4 and 5, the results on the collective vortex-gyration modes in 1D arrays of magnetic disks consisting of a single- and bi-components constituents will be presented. In Chapter 6, we investigate the effect of perpendicular bias field on dipolar-coupled vortex dynamics, and also propose an efficient way for dynamic manipulation of the dispersion relations. In the last Chapter 7, we summarize this thesis.

## **Chapter 2**

### **Research Background**

In this chapter, the theoretical background to understand the physics relevant to coupled vortex dynamics will be presented. In the first section, we provide introductory information on micromagnetism and Brown's equation, which are the basic principle of the modern magnetics. Next, we give a short overview of the static and dynamic magnetic properties of magnetic vortex in a submicron disk. In the last section, we highlight recent key results on the coupled vortex gyration.

## 2.1. Micromagnetics

The history of micromagnetics start from Landau and Liftshitz[58] and developed mainly by Brown[59]. The micromagnetics provide information on the static magnetization configuration at equilibrium, as well as, make it possible to predict the time evolution of the magnetic configuration. Therefore, the micromagnetics, nowadays, are used as the most powerful tool for understanding of static and dynamic behavior of spins in confined magnetic media. This section consists of three parts. In the first and second part, the general formalism of micromagnetics and its equilibrium criteria will be introduced. Next, in the last part, we offer some basic information on an equation of motion of magnetization in magnetic materials.

### 2.1.1. Micromagnetic Energy

Ferromagnetic materials exhibit the important property of long range magnetic order. Fundamentally, this arises from a quantum mechanical effect so-called *exchange interaction*, which forces neighboring atomic spins to be aligned in parallel under certain circumstances. From the

Heisenberg model[60], the exchange interaction between neighboring atomic spins can be expressed as

$$H_{exch} = -2 \sum_{i>j} J_{i,j} \mathbf{S}_i \cdot \mathbf{S}_j \quad (2.1)$$

where  $J_{i,j}$  is referred to as the exchange integral and  $\mathbf{S}_{i,j}$  denotes spin operator acting on  $i$  and  $j$ th atoms. The sign of  $J$  depends on the interatomic distances and can be positive or negative, being responsible for the parallel or antiparallel spin alignment. Such exchange integral involves the overlap between wave functions, and its strength decreases very rapidly with increasing distance between ions. Accordingly, this energy, in principle, is effective on a length scale of subnanometers.

The Heisenberg Hamiltonian is isotropic, then, magnetic properties should also be isotropic. However, in a real crystal, due to coupling between electron orbital and spin, the spins prefer to be aligned in parallel along certain crystallographic axes. Such direction-dependent energy, originated from spin-orbit coupling, is called as *magnetocrystalline anisotropy energy*. Meanwhile, there exists a classical interaction among dipoles, called as *magnetostatic interaction*. In contrast with the exchange interactions, which dominate only in a short range, the magnetostatic interactions between magnetic dipoles play important roles in long-range characteristics within the ferromagnet.

In the realistic model, since the static and dynamic behavior of magnetic materials is determined by competition between those energy terms, those all three energy terms should be taken into account. However, there is a major problem when relating fundamental atomic spin model to macroscopic magnetic moment[59]: for the case of exchange interaction, atomic spin model is adequate but, for the case of magnetostatic interaction, this approach is unsuitable. The micromagnetics provides a way to overcome this gap between two different frameworks, the macroscopic-scale Maxwell's theory of electromagnetics and atomic-level quantum theory, by assuming atomic spins as a vector magnetization  $M$  whose direction angles varies continuously with position vector. Then, the Eq. (2.1) should be replaced as

$$E_{exch} = -2JS^2 \sum_{i>j} \phi_{i,j} \quad (2.2)$$

where  $\phi_{i,j}$  is the angle difference between two neighboring magnetization. Here, if we use the continuous variable  $m=M/M_s$  for the magnetization, we get for small angles

$$|\phi_{i,j}| \approx |m_i - m_j| \approx |(r_i \cdot \nabla)m|. \quad (2.3)$$

Changing summation over  $i$  to an integral over the volume, the exchange interaction can be rewritten as

$$E_{exch} = \int_V A [(\nabla m_x)^2 + (\nabla m_y)^2 + (\nabla m_z)^2] d^3r \quad (2.4)$$

where  $A$  is referred to exchange constant, which is give as  $A = nJS^2/a$ . Here,  $a$  is the lattice parameter,  $n$  is 1, 2, and 4 for a simple cubic, body-centered, face-centered structure, respectively.

There are several kinds of magnetic anisotropy according to their origins. The most common type of anisotropy is the magnetocrystalline anisotropy. The magnetocrystalline anisotropy results from the spin-orbit coupling, and this, in general, can be expressed in terms of a series expansion of the directional cosine of local magnetization moment,  $\mathbf{m}=(m_x, m_y, m_z)$ , relative to the crystalline axis in a lattice[61]. In hexagonal crystals, for example, the direction of easy magnetization, *easy axis*, is given as  $c$ -axis, and all direction in the basal plane are equally hard. Then, the anisotropy energy depends only on one parameter, the angle between the magnetization and the  $c$ -axis. This type of anisotropy is usually called as *uniaxial*. Then, the magnetocrystalline anisotropy of the system can be given by

$$E_{ani} = \int_V K_0' + K_1' \cos^2 \theta + K_2' \cos^4 \theta dV \quad (2.5)$$

Putting the relation,  $\cos^2 \theta = 1 - \sin^2 \theta$ , one can rewrite the Eq.(2.5) into the typical form of

$$E_{ani} = \int_V K_0 + K_1 \sin^2 \theta + K_2 \sin^4 \theta dV \quad (2.6)$$

Here,  $K_0$ ,  $K_1$  and  $K_2$  are anisotropy constants for particular materials at a given temperature.

In cubic crystal system, the magnetocrystalline anisotropy energy density is given by

$$E_{ani} = \int_V K_0 + K_1 (\alpha_1^2 \alpha_2^2 + \alpha_2^2 \alpha_3^2 + \alpha_3^2 \alpha_1^2) + K_2 \alpha_1^2 \alpha_2^2 \alpha_3^2 dV \quad (2.7)$$

where  $\alpha_1$ ,  $\alpha_2$ ,  $\alpha_3$  are the directional cosine of local magnetization  $m$ .

The magnetostatic interaction can be understood as the interaction of local magnetization with the magnetic field, called as *demagnetizing field*, produced by its magnetization distribution. The magnetostatic interaction energy can be simply derived from the basic differential laws of magnetostatics,

$$\nabla \cdot \mathbf{B} = 0 \quad (2.8)$$

$$\nabla \times \mathbf{H} = \mathbf{J} \quad (2.9)$$

where  $\mathbf{J}$  is current density inside the material. If the current density  $\mathbf{J}$  vanishes in some finite region, the right side in Eq. (2.9) becomes zero. Then, we can introduce a magnetic scalar potential,  $\mathbf{H} = -\nabla\phi$ . Substituting the magnetic scalar potential into Eq. (2.8), a magnetostatic Poisson equation analogous to that in electrostatic can be derived in the form of

$$\nabla^2 \phi = -\rho \quad (2.10)$$

Here,  $\rho = -\nabla \cdot \mathbf{M}$  is defined as *magnetic volume charge density*.

Then, the magnetostatic potential energy is

$$\phi = \frac{1}{4\pi} \int_{all} \frac{\rho(\mathbf{r}')}{|\mathbf{r}-\mathbf{r}'|} dV' \quad (2.11)$$

If the system has a finite volume  $V$ , the system should meet a particular boundary condition at surfaces. The boundary conditions can be derived from application of the divergence and stokes theorem to Eq.(2.8) and (2.9), respectively, and this reveals that there exist the effective magnetic surface charges as defined as,  $\sigma = \mathbf{n} \cdot \mathbf{M}$ , where  $\mathbf{n}$  is the unit vector normal to the surface of element. Then, total magnetostatic potential energy for the system with a finite volume  $V$  and surface  $S$  can be re-expressed as

$$E_{magneto} = \frac{1}{4\pi} \int_V \frac{\rho(\mathbf{r}')}{|\mathbf{r}-\mathbf{r}'|} dV' + \frac{1}{4\pi} \int_S \frac{\sigma(\mathbf{r}')}{|\mathbf{r}-\mathbf{r}'|} dS' \quad (2.12)$$

The Eq. (2.12) reveals that the magnetostatic energy increases with increasing magnetic surface and volume charge density. Therefore, the magnetostatic interaction leads to a state with less magnetic surface and volume charges following the magnetic charge and the pole-avoidance principle.

In the presence of the external magnetic field  $\mathbf{H}_a$ , there exist another type of interaction between the magnetic moment,  $\mathbf{m}$ , and the field. Then, the applied field makes the magnetic moment to be aligned along the applied field direction. This interaction between the external magnetic field

and magnetic moment is called as *Zeeman interaction*. This type of interaction can be simply expressed as

$$E_{Zeeman} = -\mu_0 \int_V \mathbf{M} \cdot \mathbf{H}_a dV \quad (2.13)$$

### 2.1.2 Magnetic Equilibrium and Brown's Equations

The magnetic equilibrium state is realized by minimizing the total energy of the system which can be written as follows[59]

$$E_{total} = \int_V \left[ A(\nabla \mathbf{m})^2 + E_{ani} - \mu_0 \mathbf{M} \cdot \mathbf{H}_a - \frac{1}{2} \mu_0 \mathbf{M} \cdot \mathbf{H}_d \right] dV + \int_S \frac{1}{2} K_S (\mathbf{n} \cdot \mathbf{m})^2 dS \quad (2.14)$$

where  $H_a$  and  $H_d$  denotes the applied magnetic and demagnetizing field, respectively, and  $E_{ani}$  is the magnetic anisotropy energy. The second integral of right side in Eq. (2.14) represents the surface anisotropy energy, where  $\mathbf{n}$  denotes the surface normal and  $K_S$  is a surface anisotropy constant[62].

For equilibrium state, since the total energy is at the stationary point, the functional variation of total energy should be zero. Then, the first-order functional variation of the total energy should be

$$\delta E_{total} = \int_V \left[ 2\nabla \cdot (A\nabla \mathbf{m}) - \frac{\partial E_{ani}}{\partial \mathbf{m}} + \mu_0 M_S \mathbf{H}_a + \mu_0 M_S \mathbf{H}_d \right] \cdot \delta \mathbf{m} dV + \int_S \left[ 2A \frac{\partial \mathbf{m}}{\partial \mathbf{n}} + K_S \mathbf{n} \cdot \mathbf{m} \mathbf{n} \right] \cdot \delta \mathbf{m} dS = 0 \quad (2.15)$$

Since the variation  $\delta\mathbf{m}$  should satisfy the constraint of  $|\mathbf{m} + \delta\mathbf{m}| = 1$ , the possible variation  $\delta\mathbf{m}$  is  $\delta\mathbf{m} = \mathbf{m} \times \delta\vec{\theta}$ , where  $\delta\vec{\theta}$  denotes a small vector rotation. Then, with simple vector calculus, Eq. 2.15 can be rewritten as

$$\begin{aligned} \delta E_{total} = \int_V \mathbf{m} \times \left[ 2\nabla \cdot (A\nabla\mathbf{m}) - \frac{\partial E_{ani}}{\partial \mathbf{m}} + \mu_0 M_S \mathbf{H}_a + \mu_0 M_S \mathbf{H}_d \right] \cdot \delta\vec{\theta} dV \\ + \int_S \mathbf{m} \times \left[ -2A \frac{\partial \mathbf{m}}{\partial \mathbf{n}} - K_S \mathbf{n} \cdot \mathbf{m}\mathbf{n} \right] \cdot \delta\vec{\theta} dS = 0 \end{aligned} \quad (2.16)$$

For arbitrary  $\delta\vec{\theta}$ , Eq. (2.16) can be zero only if

$$\begin{aligned} \mathbf{m} \times \left[ 2\nabla \cdot (A\nabla\mathbf{m}) - \frac{\partial E_{ani}}{\partial \mathbf{m}} + \mu_0 M_S \mathbf{H}_a + \mu_0 M_S \mathbf{H}_d \right] = 0 \quad \text{in } V \\ \mathbf{m} \times \left[ -2A \frac{\partial \mathbf{m}}{\partial \mathbf{n}} - K_S \mathbf{n} \cdot \mathbf{m}\mathbf{n} \right] = 0 \quad \text{on } S \end{aligned} \quad (2.17)$$

From Eq. (2.17), we can define an effective field as

$$\begin{aligned} \mathbf{H}_{eff} = \frac{2}{\mu_0 M_S} \nabla \cdot (A\nabla\mathbf{m}) - \frac{1}{\mu_0 M_S} \frac{\partial E_{ani}}{\partial \mathbf{m}} + \mathbf{H}_a + \mathbf{H}_d \\ \mathbf{H}_{eff}^S = -2A \frac{\partial \mathbf{m}}{\partial \mathbf{n}} - K_S \mathbf{n} \cdot \mathbf{m}\mathbf{n} \end{aligned} \quad (2.18)$$

Rewriting the Eq. (2.17), finally, we can obtain the Brown's equation in the form of

$$\begin{aligned} \mathbf{m} \times \mathbf{H}_{eff} = 0 \quad \text{in } V \\ \mathbf{m} \times \mathbf{H}_{eff}^S = 0 \quad \text{on } S \end{aligned} \quad (2.19)$$

### 2.1.3 Equation of motion of magnetization

The dynamics of the local magnetization in ferromagnetic materials can be describe by

$$\frac{d\mathbf{m}}{dt} = -\gamma\mathbf{m} \times \mathbf{H}_{eff} \quad (2.20)$$

where  $\gamma$  is gyromagnetic ratio,  $\mathbf{H}_{eff}$  is effective field arising from exchange, anisotropic, and dipolar coupling as well as the external field.

If the system reaches at the equilibrium state releasing its internal energy, the local magnetization is collinear along the effective field direction, then, the torque on the magnetization vanishes, as described in Eq. (2.19). This dissipation process can be simply taken into account by adding a dissipation term into right-hand side of Eq. (2.20) as proposed *Landau and Lifshitz*[58]:

$$\frac{d\mathbf{M}}{dt} = -\gamma\mathbf{M} \times \mathbf{H}_{eff} - \frac{\gamma\lambda}{M_S^2}\mathbf{M} \times (\mathbf{M} \times \mathbf{H}_{eff}) \quad (2.21)$$

where  $\lambda$  is a dissipation parameter.

There are several processes which contribute to dissipation process in a magnetic material due to intrinsic origin, i.e., magnon-phonon interaction, and interaction between 3d and 4s electrons, as well as extrinsic origin. *Gilbert* proposed a phenomenological damping term combining all

damping effects in with a damping constant. Finally, the equation of motion, called as *Landau-Lifshitz Gilbert* equation[63], is

$$\frac{d\mathbf{M}}{dt} = -\gamma\mathbf{M}\times\mathbf{H}_{eff} - \frac{\alpha}{M_s}\mathbf{M}\times\frac{d\mathbf{M}}{dt} \quad (2.22)$$

with a dimensionless parameter  $\alpha = \lambda/M_s$ ,

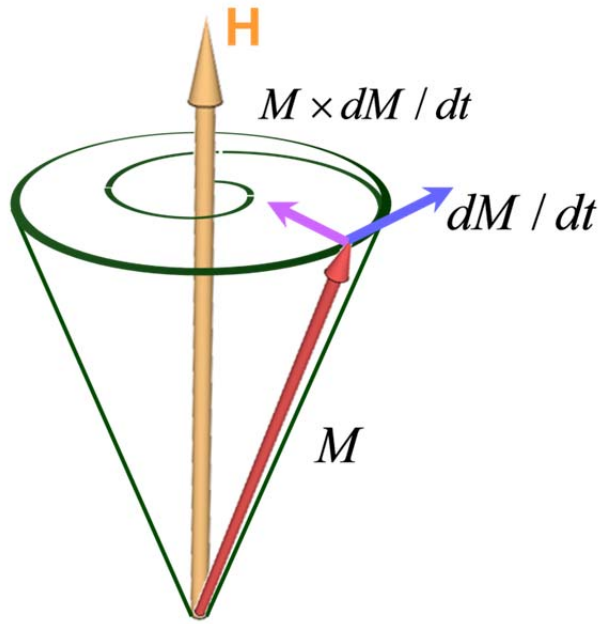


**FIG. 2.1** Magnetization precession motion with damping (as adopted from Ref. [2])

## 2.2. Magnetic Vortex

This section offers some information on the static and dynamic properties of magnetic vortex. In the first part, a brief overview of magnetic vortex and its historical review is given. In second part, the coupled vortex dynamics, the main issue of this thesis, is introduced.

### 2.2.1 What is a Magnetic Vortex?

The magnetic properties of ferromagnetic elements depend not only on the crystallographic nature of the system but also on their geometry of the patterned structure. For example, samples with large dimension usually exhibit a multi-domain structure as a remanence state. In a submicron-sized soft ferromagnetic disk, the competition between the short-range exchange energy, which favors parallel spin configuration, and long-range dipole-dipole interactions, which prefer to have closure spin configuration to avoid magnetic surface charge, allows a stable magnetic configuration called as *magnetic vortex*. The magnetic vortex is a unique magnetic configuration with curling in-plane component of magnetization and the out-of component of magnetization pointing perpendicularly to the disk plane within the ~10 nm size vortex core[64] (see FIG. 2.2).

Though, the magnetic vortex structure has been predicted much long before in theory, the experimental evidence of the vortex structure has been reported quite later, due to the limitation of imaging techniques. The first direct imaging of in-plane curling structure of a magnetic vortex was done by M. S. Cohen by means of Lorentz microscopy[65]. After several decades, the in-plane magnetic structure was reconfirmed through other various imaging techniques, i.e., low-angle electron diffraction[66], soft X-ray magnetic microscopy[67]. One experiment among the first observations of the out-of structure of the magnetic vortex core is provided by Shinjo with the help of magnetic force microscopy (MFM)[68]. However, the lateral resolution of MFM is limited to  $\sim 20\text{nm}$ , the result could not provide the detailed internal structure in a magnetic vortex core. A few years later, the details of spin structure of magnetic vortex core were investigated by A. Wachowiak *et al*, through the sophisticated spin-polarized scanning tunneling microscopy[64].

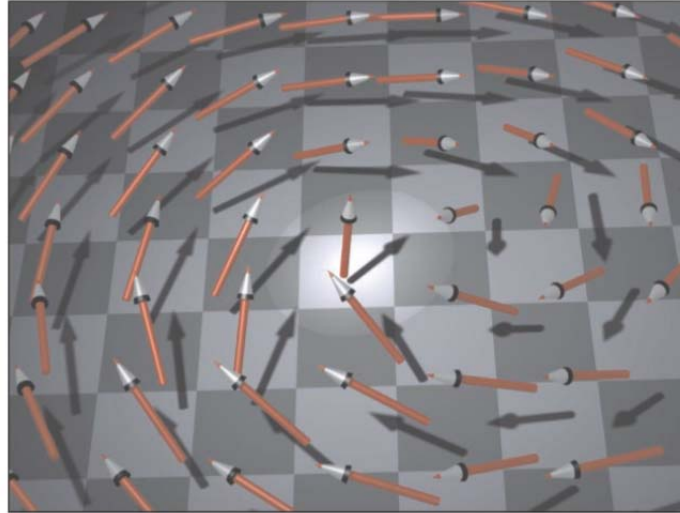


**FIG. 2.2** Schematic illustration of magnetic vortex: the in-plane magnetization continuously curls around the center. In the center of the structure (highlighted region), the magnetization is perpendicular to the plane (adapted from A. Wachowiak *et al.*[64]).

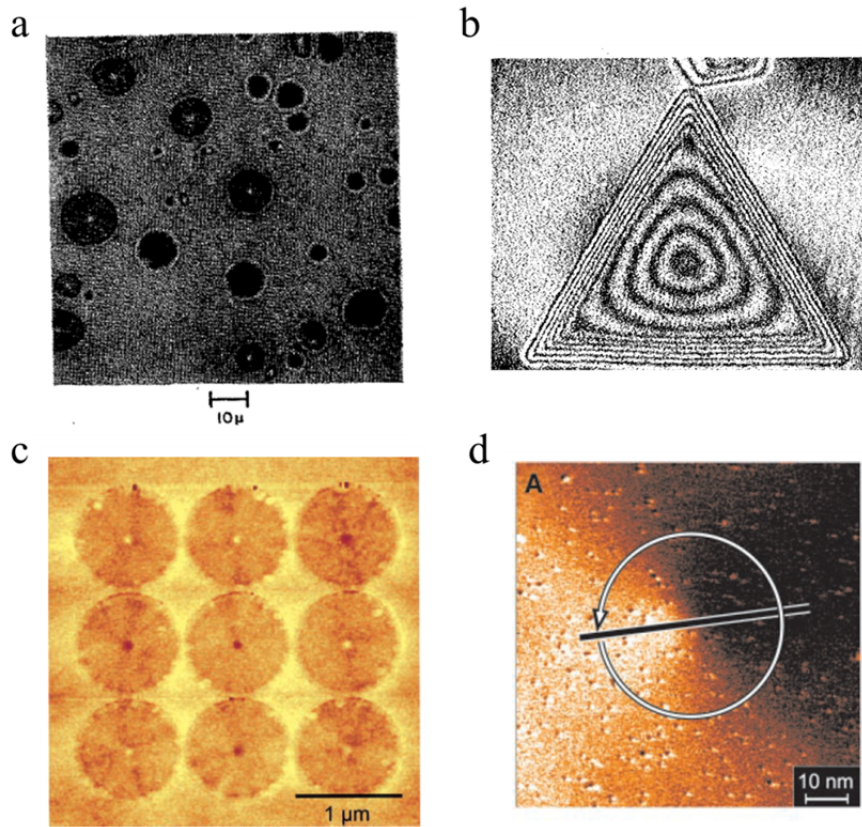


**FIG. 2.3** Direct measurement of magnetic vortices as obtained from Lorentz microscopy[65] (a), low-angle electron diffraction[66] (b), MFM[68] (c), and spin-polarized scanning tunneling microscopy[64] (d).

This magnetic vortex can be characterized by two different parameters: chirality ( $C$ ) and polarization ( $p$ ). The polarization indicates the orientation of vortex-core ( $p=1$  and  $-1$  for up and down, respectively) and chirality are the rotation sense of in-plane magnetization ( $C=1$  for counterclockwise and  $-1$  for clockwise). There are four different energetically equilibrated states according to the combination of its chirality and polarity of magnetic configuration (see FIG. 2.4)

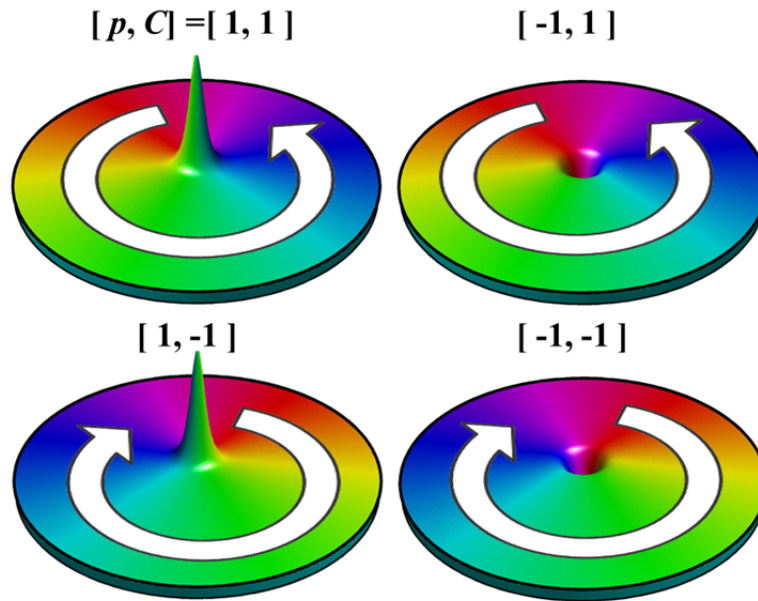


**FIG. 2.4** Four energetically equivalent magnetic configurations of the magnetic vortex as denoted by the combination of vortex core polarization  $p$ , and the chirality  $C$ . The height and color indicate the local out-of- and in-plane magnetization components, respectively.

### 2.2.2 Dynamics of a Magnetic Vortex

The magnetic vortex in a submicron-sized disk carries a rich frequency spectrum of spin excitations, including the low-frequency translational mode (gyrotropic mode)[69-75] and the various high-frequency radial and azimuthal spin waves modes[71, 76-79], which are originated from symmetry and topological characteristics of the magnetic configuration. In particular, the gyrotropic mode which displays a spiral motion of vortex core with a characteristic eigenfrequency at the sub-GHz range, has been intensively studied due to its possible application to the vortex based memory device and microwave generator.

The gyrotropic motion of vortex, in general, can be described by a collective variable theory developed by Thiele in 1973[80]. According to the theory, by assuming a magnetic domain at steady-state motion, the LLG equation, which describes the dynamics of a single magnetic moment, can be transformed into the force balance equation of a magnetic solitary structure, where each term is determined by the initial magnetic configuration and the position vector of the magnetic soliton. Then, the Thiele's equation is

$$-\mathbf{G} \times \frac{d\mathbf{X}}{dt} - D \frac{d\mathbf{X}}{dt} + \frac{\partial W}{\partial \mathbf{X}} = 0 \quad (2.23)$$

where  $X = (X, Y)$  is the position vector of the magnetic soliton. The first term indicates a gyrotropic force, a Magnus-type force, perpendicular to a velocity vector of the magnetic soliton, the second term is the damping force, and the last term is the restoring force as approximated to the first derivative of total magnetic energy  $W$  with respect to the position of the magnetic soliton.

The  $G$  and  $D$  values for a magnetic vortex structure has been estimated theoretically for various systems. The first attempt to adopting the Thiele's formalism into the magnetic vortex structure was done by D. L. Huber[81] assuming a 3D vortex magnetization in 2D planar magnetic system. In 1993, Usov and Peschany calculated the  $G$  and  $D$  with a simple variational function for magnetic vortex structure in a cylindrical magnetic disk with a finite thickness and radius[82].

The restoring forces, for a finite structure, are mainly attributed to magnetostatic interaction induced by the displacement of vortex core from its equilibrium position. This restoring force of the magnetic vortex in a cylindrical disk can be evaluated based on two distinct models describing the field evolution of magnetic vortex structure in the disk: the *rigid vortex model* [83] and *two vortex model (side-surface charge free model)* [75, 83, 84]. The first model assumes that the magnetization distribution is shifted without change of their structure, and thus, magnetic surface charge induced side surfaces of the cylinder gives the main contribution to the

magnetostatic interaction energy. This model is adequate for describing the static problem of the magnetic vortex. In contrast to that, the two vortex model assumes the deformation of magnetization distribution when it shifts from the center of disk to avoid the generation of magnetic surface charge. Then, the magnetostatic interaction is only attributed to the magnetic volume charge. Then, this model is more realistic for the dynamic problem than the rigid vortex model.

### **2.2.3 Coupled Magnetic Vortex**

For the case of physically separated but dipolar-coupled elements, the dipolar interaction between neighboring elements gives rise to collective spin excitations in their spin configurations. This dipolar coupling mediated collective spin excitation has been studied in the various spin system. In particular, dipolar-coupled vortex dynamics has been recently proposed and demonstrated through the theoretical studies[43-45, 50, 85, 86], micromagnetic simulation [48-50, 55] as well as experiments[46, 47, 51-54, 57, 87]. The first theoretical attempt to the dipolar-coupled vortex gyration was done by Shibata *et al.*[43]. In the work, they theoretically derived the collective modes and their eigenfrequencies of vortex core motion in latterly coupled two magnetic disks for the variable polarization and chirality configurations. For a rigid vortex model, the interaction energy

between magnetic disks, which is mainly originated from the interaction between magnetic surface charges, has the simple form of

$$W_{\text{int}} = \frac{C_1 C_2}{R^2} (\eta_x x_1 x_2 - \eta_y y_1 y_2) \quad (2.24)$$

Here  $\eta_x$  and  $\eta_y$  represent the interaction strength along the  $x$  and  $y$  axes, respectively, which depend on the geometrical parameters, i.e., the thickness and inter-distance between disks, and material parameters, and the  $x_{1,2}$  and  $y_{1,2}$  denotes the  $x$  and  $y$  component of vortex core position in the each disk. Based on the explicit form of the dipolar coupling between vortices, they found four different translational modes which depend only on the relative polarization ordering in dipolar-coupled two vortices.

In 2005, dynamics of vortices which are physically separated via non-magnetic layer but vertically dipolar-coupled was theoretically predicted by Guslienko *et al.*[88]. The study reveals that the magnetostatic coupling between the vortices is proportional to the inner product between in-plane volume magnetization vectors induced by the shifted vortices from the center of each disk, and this coupling between layers leads to two coupled-vortex gyration.

Very recently, some experimental evidence for dipolar-coupled vortex dynamics were revealed through various experimental techniques, i.e., X-ray imaging technique[46, 51-53, 56, 89], ferromagnetic resonance (FMR)[47], and electrical measurement[54, 90]. Vogel *et al.*[47], for

example, investigated a dependence of the eigenfrequency of vortex-core motion within arrays of magnetic disks on the interdistance between neighboring disks. Jung *et al.*[46], for the first time, directly measured coupled-vortex gyration in a pair of magnetic disks through the full-field magnetic transmission soft x-ray microscopy. Suqimoto *et al.*[54], experimentally demonstrated the gyration modes of coupled vortices in a pair of disks with the help of homodyne detection method.

This robust mechanism for energy transfer via coupled vortex gyration is expected to provide the advantages of a fast and tunable energy transfer rate that is a function of disk interdistance and interaction strength, and also of low-power consumption through the resonant vortex excitation. As a mean of manipulating the vortex-based signal transfer, 1D and 2D arrays of ferromagnetic disks with vortex states, similar to conventional magnonic crystals, has been proposed[44, 85, 86]. However, direct measurement of collective behaviors in those kinds of magnonic crystals has still not been achieved.

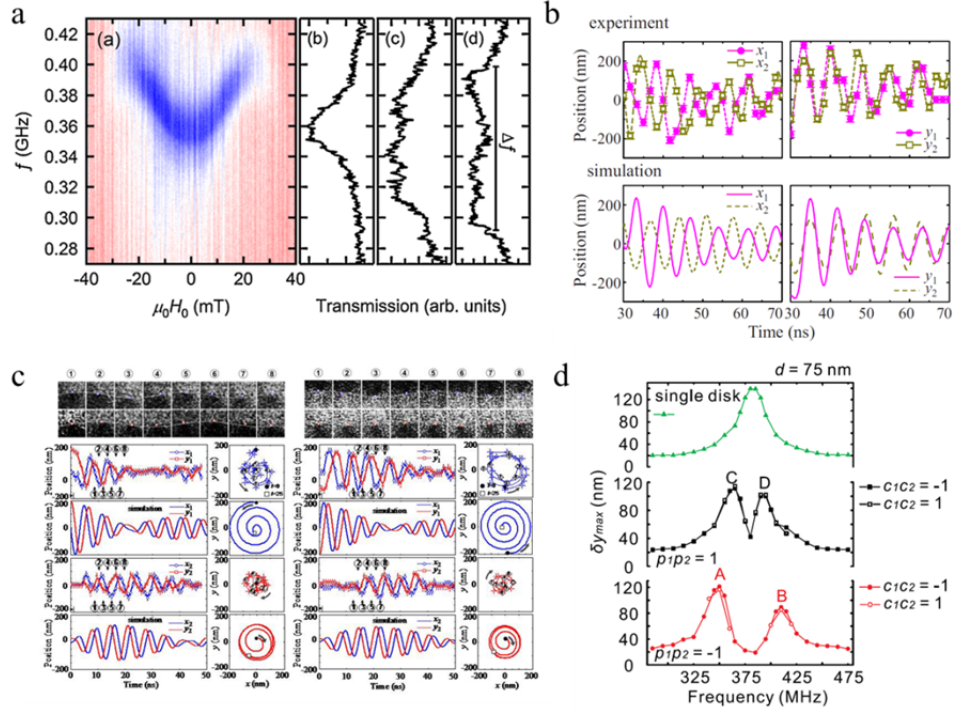


**FIG. 2.5** Experimental demonstration of coupled-vortex dynamics by using ferromagnetic resonance[47] (a), magnetic soft X-ray microscopy[46, 51] (b), c) and electrical method[54] (d).

## **Chapter 3**

### **Method**

This chapter deals with the experimental methods used for direct observation of dynamics of dipolar-coupled magnetic vortex gyration and the micromagnetic simulation tool for investigation of the relevant physics. Section 3.1 gives an introduction to the X-ray magnetic dichroism (XMCD), which is a basic principle in X-ray magnetic imaging techniques, and information on the detailed setup for full-field magnetic transmission soft X-ray microscopy (MTXM) and scanning transmission soft X-ray Microscopy (STXM). In section 3.2, the numerical method for micromagnetic simulations is informed.

### **3.1 X-ray Magnetic Imaging Technique**

Direct imaging of magnetic structures has led to our present level of understanding of micromagnetic phenomena. Nowadays, a number of modern imaging techniques are commonly used to investigate magnetic structures in magnetic materials. In particular, magnetic imaging techniques based on X-ray has drawn much interest because of its element-selectivity characteristics. This element-selective technique can offer the unique possibility to achieve layer-resolved images of magnetic multilayer samples and also quantitative understanding on micromagnetic coupling mechanism between magnetic layers. There are several techniques for measurement of magnetic domain structure by using X-ray, i.e., x-ray photoelectron emission microscopy (X-PEEM), magnetic transmission soft X-ray microscope (MTXM), and scanning X-ray transmission microscopy (STXM). In the following section, we, especially, focus on two measurement techniques, MTXM and STXM, which are used in this thesis for the investigation of the coupled vortex dynamics, and also briefly introduce fundamentals of X-ray magnetic circularly dichroism (XMCD).

### 3.1.1 X-ray Magnetic Circular Dichroism (XMCD)

The concept of XMCD was pioneered by Schutz *et al.*[91] For  $3d$  transition ferromagnetic materials, the  $d$  shell has a net spin moment, which results from the imbalance in density of states (DOS) of electrons or holes with up and down spin [see FIG. 3.1 (a)]. The difference in the number of unoccupied spin-up and down state can be measured by spin-dependent X-ray absorption process by using right circularly polarized (RCP) or left circularly polarized (LCP) photons[92, 93]. When the RCP (LCP) photons are injected to the materials, the photons transfer their angular momentum,  $+\hbar$  ( $-\hbar$ ), to the excited photoelectrons, and these photoelectrons carry the momentum as a spin or an angular moment. Consequently, the excited photoelectrons exhibit a certain spin polarization, and the spin polarization of the photoelectrons is determined solely by the helicity of injected photons because spin-flip process is not allowed during the transition of photoelectrons from  $2p$  to  $3d$  shell. Then, since the transition intensity is proportional to the number of unoccupied  $d$  state, accordingly, a difference in X-ray absorption intensity occurs depending on the helicity of photon for ferromagnetic materials [see FIG. 3.1 (b)].

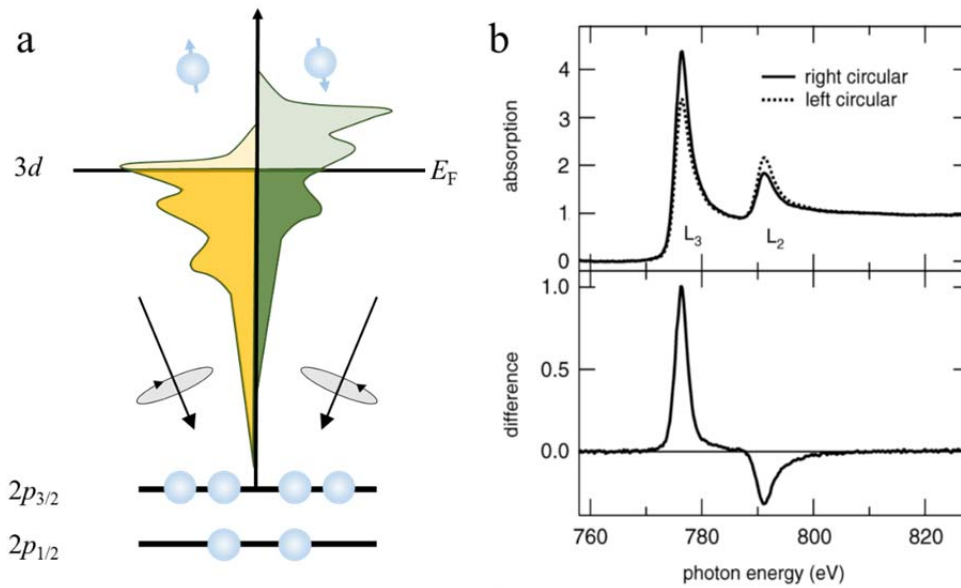


**FIG. 3.1** (a) Schematic illustration for X-ray magnetic circular dichroism spectroscopy. (b) Example of an experimental XMCD spectrum of a thin Co film on Cu(001). Top panel: Absorption spectra at the Co  $L_{2,3}$  edge for right (continuous line) and left circular polarization (dotted line) of the exciting X-rays. Bottom panel: Difference between the two spectra of upper figure[93].

The difference in absorption coefficients between two circularly polarized beams at certain energy,  $\Delta\mu(E)$  normalized with respect to the unpolarized absorption coefficient  $\mu_{|i\rangle}$  in an atomic core level  $|i\rangle$  is given by[94]

$$\frac{\Delta\mu}{\mu_{|i\rangle}}(E) = \frac{\sigma_c}{\sigma_{|i\rangle}}(E)(\mathbf{m} \cdot \hat{\mathbf{z}})P_c \quad (3.1)$$

where  $\mathbf{m} \cdot \hat{\mathbf{z}}$  denotes the projection of the magnetic moment  $\mathbf{m}$  onto the propagation direction  $\hat{\mathbf{z}}$  of the circularly polarized incoming photons.  $\sigma_c/\sigma_{|i\rangle}$  is the magnetic absorption cross section normalized with respect to the unpolarized atomic cross section, and  $P_c$  represents a degree of circular polarization of the incident photon. Then, the effect of dichroism is proportional to  $\cos \theta$ , where  $\theta$  denotes the angle between the injected photon's spin direction and the magnetization direction of ferromagnet. Therefore, the dichroism effect is maximum when the photon's spin direction is parallel and antiparallel to the magnetization direction.

### 3.1.2 Full-field magnetic transmission soft X-ray microscopy (MTXM)

We conducted preliminary experiments for coupled vortex gyrations in different five-disk array samples by using magnetic transmission x-ray microscopy (MXTM) at the XM-1 beamline (at Advanced Light Source, Lawrence Berkeley National Laboratory). The schematics of optical setup for the X-ray microscope is illustrated in FIG. 3.2. The MTXM used in the experiment is composed of following parts: a bending magnet source, a monochromator and illuminating assembly, Fresnel zone plate, a pinhole, a micro zone plate, and a CCD detector. The illumination is provided by the bending magnet which allows the synchrotron radiation. The illumination energy of the radiated waves can be manipulated by the linear monochromator composed of the Fresnel zone plate (condenser zone plate) and a pinhole near the sample plane. The resolution of illumination energy is determined by the dimension of condenser zone plate and the size of pinhole, which is typically  $E/\Delta E=500\sim 700$ . The high-resolution X-ray beam passing through the sample is projected through the micro zone plate, which magnifies the image taken by the focused beam, onto a CCD camera. The spatial resolution of the present setup is  $\sim 25\text{nm}$  and this can be improved up to  $\sim 15\text{nm}$  using a high-quality Fresnel zone plate. The CCD camera is a  $2048 \times 2048$  pixel array and the field of view of the MTXM is typically  $10$

micron. The position of the focused beam can be selected by using Zeiss Axioplan visible light microscope and sample stage with 2 micron of X-Y position accuracy. FIG. 3.3 shows the images for experimental setup of the full-field magnetic transmission soft X-ray microscope at ALS BL. 6.1.2. The inset image represents the sample stage consisting of a electromagnet, which can produce in-plane magnetic fields. In the measurement, we captured the in-plane magnetization tilting the sample  $60^\circ$  away from the propagation direction of the incident X-ray beam.

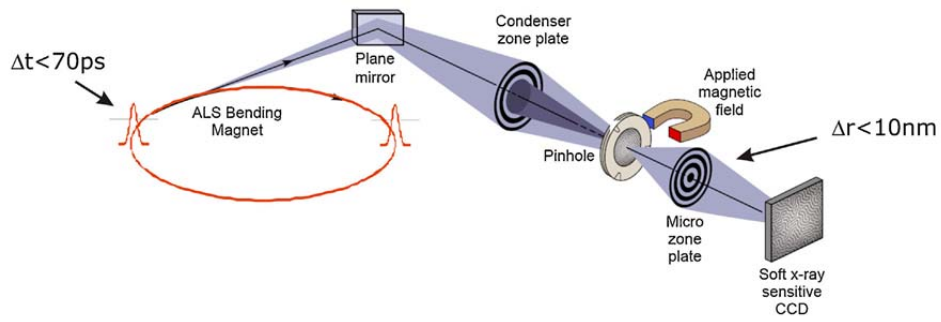


**FIG. 3.2** Schematics of the full-field magnetic transmission soft X-ray microscope at ALS BL 6.1.2 used for magnetic imaging.

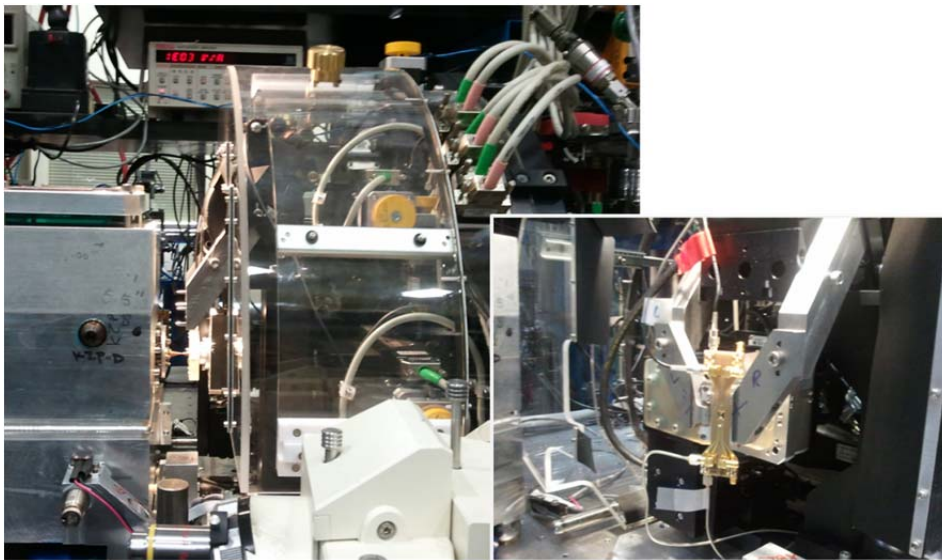


**FIG. 3.3** Experimental setup of the full-field magnetic transmission soft X-ray microscope at ALS BL 6.1.2. The inset image shows the sample stage with a electromagnet.

### **3.1.3 Scanning Transmission soft X-ray Microscopy (STXM)**

In this work, we measured trajectories of the core motions of all five disks using STXM by monitoring the out-of-plane core magnetizations at the MAXYMUS beamline (BESSY II; Helmholtz-Zentrum Berlin, Germany)[95]. FIG. 3.4 shows the schematic setup of the STXM. The monochromatic beam passing through the zone plate is focused to smallest spot size, and forms a microprobe which is used for scanning the sample. The scanning process is achieved by moving either the sample or the zone plate. The spatial resolution of the measurement is mainly determined by the spot size of X-ray beam, which can be tuned by grazing incidence mirrors and the zone plate. The intensity of transmitted X-ray through the sample is measured with a fast detector. The amplitude contrast of the images from STXM is, in general, lower about one order of magnitude than those from MTXM, because the STXM setup does not contain the micro zone plate for magnification. In contrast to the MTXM which has a limited field view of ~20 micron, images of arbitrary dimensions can be acquired in the STXM by connecting multiple images together in the computer.

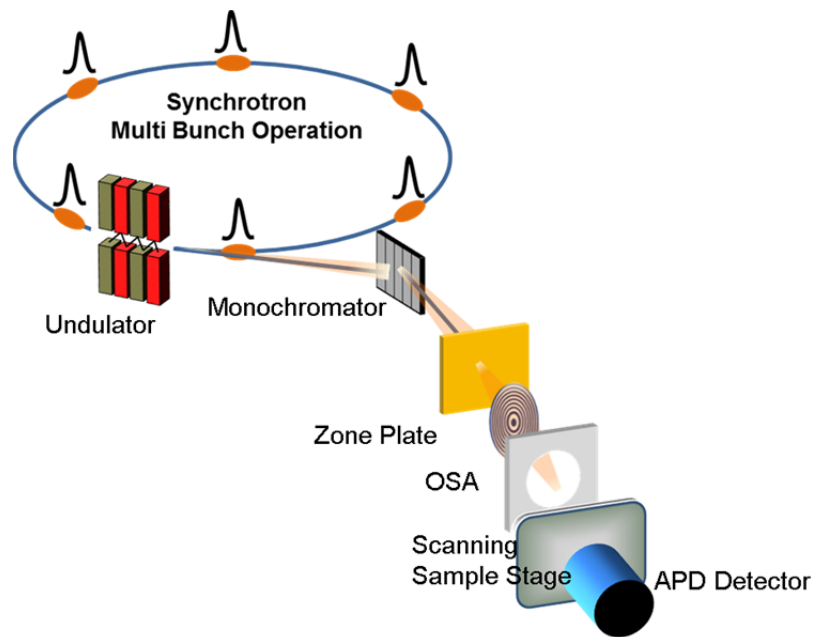


**FIG. 3.4** Schematic illustration of the scanning transmission X-ray microscope (STXM).

### **3.1.4 Time-resolved measurement (pump-probe technique)**

The time-resolved magnetic imaging is achieved by means of pump-and probe spectroscopic techniques. Pump-probe experiment measure the averaged, repeatable dynamics of a given system using a short pump pulse, which stimulates the dynamics in the system, and a probe pulse which measures the state of the given time. The measured time of dynamics by the probe can be chosen manipulating the delay between pump and probe. Then, the time-resolution of the measurement technique is determined by the limitation of the length or rise time of both pulses. In both MTXM and STXM, the current pulse or magnetic field is used for excitation (pump) which modulates the initial state, and the X-ray is used for measurement (probe) of the instant magnetic state. The temporal resolution of both measurement technique is set by inherent pulse duration of X-ray beam source, and is given by  $\sim 70\text{ps}$  ( for MTXM at ALS) and  $\sim 35\text{ps}$  ( for STXM at BESSY II).

### 3.3 Micromagnetic simulations

The spin dynamics in magnetic materials can be described by LLG equation, as introduced in Chapter 2.1. There are, in general, two different numerical approaches adopted to solve the partial differential equation: the finite element method (FEM) combined with the boundary element method and the finite difference method (FDM). The FDM-based simulators are known to be in general faster and need less memory, but have larger surface roughness than FEM-based tools. In the present works, we adopted FDM-based *Object Oriented MicroMagnetic Framework* (OOMMF)[96] as a simulation tool, which is the most commonly used code for micromagnetic simulation developed by Mike Donahue and Don Porter in national institute of standards and technology (NIST).

The code utilizes an LLG equation of 3D spins in 2D regular mesh of squares. The effective field in the LLG equation at each time step is calculated from the derivative of each interaction energy term, i.e., exchange, anisotropy, Zeeman, and dipolar energy, with respect to the local magnetization. The anisotropy energy is calculated assuming the constant magnetization in each cell. The exchange energy is calculated only for the coupling between the 8 nearest-neighboring cells. For the calculation of magnetostatic energy, the discrete convolution method and the fast Fourier

transform (FFT) implemented with a zero-padding technique are used to reduce total simulation time.

The integration of LLG ordinary differential equation (ODE) is achieved using an Adams predictor-corrector method, an algorithm consisting of two steps, prediction and correct steps. The predictor-corrector method uses an explicit technique to predict the solution at each step and an implicit technique to correct the value. In the simulator, a first-order forward Euler method or fourth order Runge-Kutta methods can be chosen as predictor-corrector solvers, and also used for a backup in case the process fails to find adequate value. Each step is accepted only if the total energy of the system decreases, and also the maximum error between the predicted and final  $\mathbf{M}$  is smaller than a nominal value[96].

## Chapter 4

### Collective Vortex Oscillation Modes in a 1D chain

#### Consisting of a Single-component Constituents

Recently, magnetic vortex-based magnonic crystal has drawn interests from both fundamental and practical point of view. However, due to the technical difficulties measuring collective vortex dynamics, still no experimental demonstration on the magnonic crystal composed of vortex-state-disk array has been reported.

In this chapter, we report on the first direct experimental demonstration, by means of state-of-the-art time-resolved scanning transmission x-ray microscopy (STXM), of quantized (or discrete) wave modes of collective vortex gyrations excited in five physically separated but dipolar-coupled disks in a permalloy (Py: Ni<sub>80</sub>Fe<sub>20</sub>) disk array. Also, we investigate the experimentally observed discrete modes and their dispersion relations with the help of numerical calculations of coupled linearized Thiele equation, micromagnetic numerical simulations, and analytical derivations.

## 4.1 Sample preparation and experimental setup

The sample studied in this chapter is prepared by Guido Meier's group in University of Hamburg. The five Py disk array is fabricated onto a 100-nm-thick silicon-nitride membrane using electron-beam lithography and lift-off techniques. Each disk has a thickness of 60 nm and a diameter of 2  $\mu\text{m}$ . The center-to-center distance between neighboring disks is 2.25  $\mu\text{m}$ . An 800-nm-wide Cu stripline of 120 nm thickness (with a gold cap of 5 nm thickness) is deposited onto the first disk. Figure 4.1 shows a scanning electron microscopy (SEM) image of the sample (FIG. 4.1a) as well as STXM images of out-of-plane core magnetizations (FIG. 4.1b) and in-plane curling magnetizations (FIG. 4.1c) in each of the five Py disks. Here, the polarization and chirality configurations of the array are  $p = [+1, -1, +1, -1, +1]$  and  $C = [-1, -1, -1, -1, +1]$ , respectively (see FIG. 4.1d), as obtained from the STXM images, where  $p = +1(-1)$  corresponds to upward (downward) core magnetization, and  $C = +1$  to counter-clockwise (CCW) and  $C = -1$  to clockwise (CW) in-plane curling magnetization. Note that the sample has the opposite core orientations between the NN disks.

Trajectories of the core motions of all five disks are directly observed using STXM by monitoring the out-of-plane core magnetizations at the MAXYMUS beamline (BESSY II; Helmholtz-Zentrum Berlin,

Germany). The magnetic contrast is provided via XMCD at the Ni  $L_3$  absorption edge (around 852.7 eV). The measurements showing the core polarization are performed using negative circular-polarized x-rays (where an upward/downward core appears as a dark/white spot), whereas the measurements showing the chirality configuration are performed with the sample tilted  $60^\circ$  with respect to the beam axis, using positive circular-polarized x-rays (where a CW/CCW curling magnetization leads to a dark/bright contrast in the lower part of the disk). In the dynamic measurements, snapshot images of the individual core motions scanned in lateral steps of 8 nm are taken in time increments of 400 ps over a period of 60.8 ns after application of the field pulse at zero time.

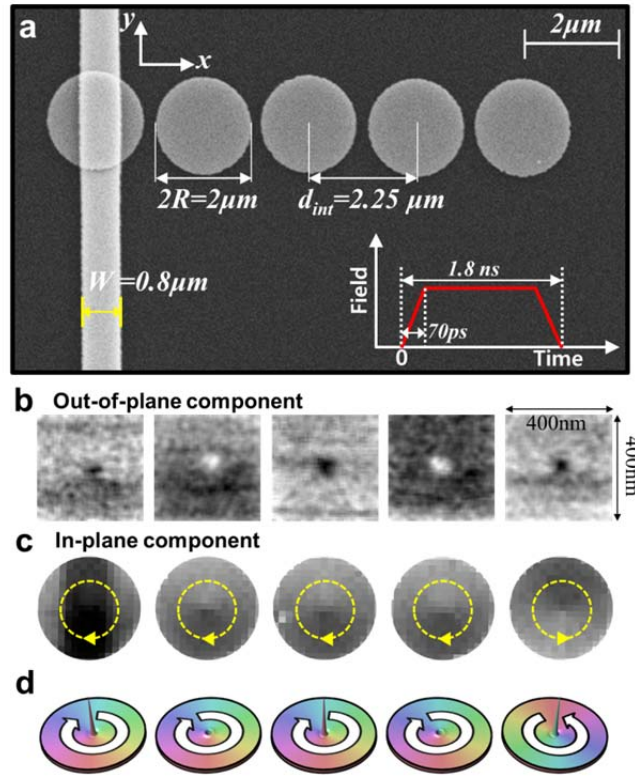


**FIG. 4.1** (a) SEM image of sample with a array of five Py disks of identical dimensions and center-to-center distance and with a stripline for application of local magnetic field pulses to the left-end disk. The sample is deposited onto a silicon nitride membrane. The inset shows a schematic drawing of the field pulse used in the experiment. (b) and (c) represent initial vortex states in the five individual disks, out-of-plane magnetizations (the bright and dark spots correspond to the down and upward core orientations, respectively) and in-plane curling magnetizations (the curling orientations are indicated by the dashed arrows), as obtained from STXM measurements, respectively. (d) is a schematic illustration of the initial states of the sample.

## 4.2 Vortex-core gyration propagation along dipolar-coupled disks

For the quantitative analysis, we extracted the position vector of vortex core in each disk, from the snapshot images of the individual vortex gyrations measured by STXM. Figure 4.2 shows the  $x$  (red color) and  $y$  (blue) components (FIG. 4.2a) of the displacements of the individual cores and their trajectories (Fig. 2b) in the disk plane, as measured by time-resolved STXM. The experimental results (top of 2a and 2b) are compared with the corresponding micromagnetic simulations (bottom of 2a and 2b) performed using the OOMMF code (version 1.2a4). In the simulations, we used the typical material parameters corresponding to Py as follows: saturation magnetization  $M_s = 780 \times 10^3$  A/m, exchange stiffness constant  $A_{\text{ex}} = 1.3 \times 10^{-11}$  J/m, and Gilbert damping constant  $\alpha = 0.01$ .

The characteristic beating patterns along with their modulation envelopes are observed in each of the five disks (FIG. 4.2a). Owing to the direct excitation of the first disk, a large-amplitude gyration in that disk is observed, and is then allowed to propagate towards the NN disk and beyond through the array. The vortex-gyration transfer to the next disk and its further propagation are evidenced by the increase of the gyration amplitude in the second and remaining disks along with the concomitant and remarkable decrease of the first disk's gyration amplitude. The ratio

between the maximum displacements in disk 5 and disk 1 is about 0.24. Since our pump-and-probe measurements are carried out within a time period of 60.8 ns, and the intrinsic damping of Py is not negligible but rather significant (as strong as  $\alpha \sim 0.01$ ), we cannot clearly observe backward propagation bounced at the last (5<sup>th</sup>) disk. However, the signature of weak reflection is evident by the increase of the gyration amplitude in the 4<sup>th</sup> disk at around 55 ns, as compared with the simulation result.

It has been reported that coupled gyrations in two-dipolar-coupled disks can be described by the superposition of the two normal modes[43, 50, 51, 53, 54]. Dipolar interaction between NN disks breaks the radial symmetry of the potential energy of each core, which depends on the disk pair's relative vortex-state configuration (both the polarization and chirality ordering). Analogously, for the case of the five-disk system used in this study, the beating patterns is the result of linear combinations of the five normal modes of coupled vortex gyration in the entire array

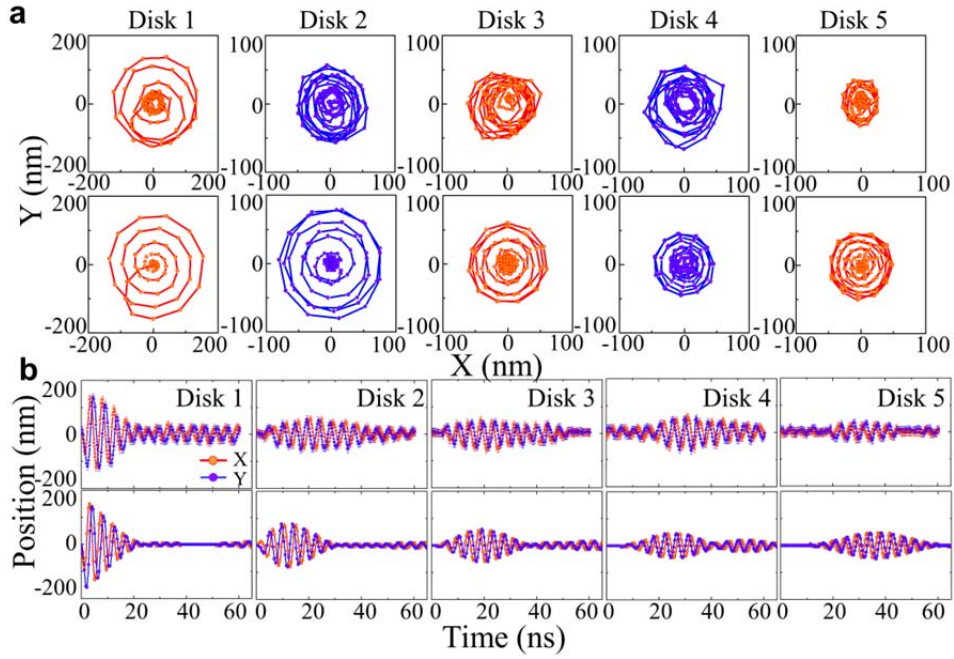


**FIG. 4.2** (a) Oscillatory  $x$  (red) and  $y$  (blue) components of vortex-core positions in individual disks as measured by STXM (upper row) and corresponding micromagnetic simulation data (bottom row). (b) The trajectories of the vortex-core motion under a pulsed magnetic field during the time period  $t = 0-60.8$  ns. Dotted arrows indicate the sense of gyration of the individual cores.

### 4.3 Numerical calculation of $N$ coupled Thiele equations for $N$ coupled vortex gyrations

To investigate the fundamental physics of the results as obtained from the experiments and micromagnetic simulations, we conducted further numerical calculations based on the linearized Thiele equations for one-dimensional (1D) dipolar-coupled disks of finite disk number  $N$ , taking into account the potential energy modified by dipolar interaction between only the next neighboring (NN) disks. The corresponding force-balance equation for the  $n^{\text{th}}$  disk is given as

$$-\mathbf{G}_n \times \dot{\mathbf{X}}_n - \hat{D}_n \dot{\mathbf{X}}_n + \partial W / \partial \mathbf{X}_n = 0, \quad (4.1)$$

where  $\mathbf{X}_n = (X_n, Y_n)$  is the core position vector in the  $n^{\text{th}}$  disk based on the collective coordinate ansatz.  $\mathbf{G}_n = -G p_n \hat{\mathbf{z}}$  is the gyrovector with its constant,  $G = 2\pi L M_s / \gamma > 0$  (the saturation magnetization  $M_s$ , the gyromagnetic ratio  $\gamma$ , and the thickness of individual disk  $L$ ), and  $\hat{D}_n = D \hat{I}$  is the damping tensor with the identity matrix  $\hat{I}$  and the damping constant  $D$ . The  $p_n$  represents the vortex core polarization in the  $n^{\text{th}}$  disk. The total potential

energy is given as  $W = \sum_{n=1}^N \left( W_n(0) + \frac{1}{2} \kappa |\mathbf{X}_n|^2 \right) +$

$\sum_{n=2}^{N-1} W_{\text{int}}(\mathbf{X}_{n-1}, \mathbf{X}_n, \mathbf{X}_{n+1}) + \sum_{n=1}^N W_{\mathbf{H},n}$ , where the first and second terms together

are the potential energy with the stiffness coefficient  $\kappa$  for isolated disks, and the third term  $W_{\text{int}}$  is the dipolar interaction energy between only the NN disks. The last one,  $W_{\mathbf{H},n} = -\mu_n (\hat{\mathbf{z}} \times \mathbf{H}_n) \cdot \mathbf{X}_n$ , is the Zeeman energy term due to a driving force, where  $\mu_n = \pi R L M_S \xi C_n$  (the radius of the individual disk  $R$ , the chirality of the vortex in the  $n^{\text{th}}$  disk  $C_n$ , and  $\xi = 2/3$ ).

The  $W_{\text{int}}$ , for a given  $n^{\text{th}}$  disk, can be written as

$$W_{\text{int}} = C_{n-1} C_n (\eta_{\parallel} X_{n-1} X_n - \eta_{\perp} Y_{n-1} Y_n) + C_n C_{n+1} (\eta_{\parallel} X_n X_{n+1} - \eta_{\perp} Y_n Y_{n+1}), \quad (4.2a)$$

for  $n = 2, 3, \dots, N-1$ ,

$$W_{\text{int}} = C_n C_{n+1} (\eta_{\parallel} X_n X_{n+1} - \eta_{\perp} Y_n Y_{n+1}), \quad (4.2b)$$

for  $n = 1$

$$W_{\text{int}} = C_{n-1} C_n (\eta_{\parallel} X_{n-1} X_n - \eta_{\perp} Y_{n-1} Y_n), \quad (4.2c)$$

for  $n = N$ .  $\eta_{\parallel}$  and  $\eta_{\perp}$  represent the interaction strength along the  $x$  and  $y$  axes (here  $x$  is the bonding axis), respectively. The asymmetry between  $\eta_{\parallel}$  and  $\eta_{\perp}$  is due to the breaking of the radial symmetry of the potential energy of the isolated disks by their dipolar interaction. Finally, the coupled force-balance equations for the entire system are given as

$$-p_n G(dY_n/dt) - D(dX_n/dt) + \kappa X_n + \eta_{\parallel} C_n (C_{n+1} X_{n+1} + C_{n-1} X_{n-1}) = -\mu_n H_{y,n}, \quad (4.3a)$$

$$p_n G(dX_n/dt) - D(dY_n/dt) + \kappa Y_n - \eta_{\perp} C_n (C_{n+1} Y_{n+1} + C_{n-1} Y_{n-1}) = \mu_n H_{x,n}, \quad (4.3b)$$

where  $n = 2, 3, \dots, N-1$ ,

$$-p_n G(dY_n/dt) - D(dX_n/dt) + \kappa X_n + \eta_{\parallel} C_n C_{n+1} X_{n+1} = -\mu_n H_{y,n}, \quad (4.4a)$$

$$p_n G(dX_n/dt) - D(dY_n/dt) + \kappa Y_n - \eta_{\perp} C_n C_{n+1} Y_{n+1} = \mu_n H_{x,n}, \quad (4.4b)$$

where  $n = 1$ , and

$$-p_n G(dY_n/dt) - D(dX_n/dt) + \kappa X_n + \eta_{\parallel} C_n C_{n-1} X_{n-1} = -\mu_n H_{y,n}, \quad (4.5a)$$

$$p_n G(dX_n/dt) - D(dY_n/dt) + \kappa Y_n - \eta_{\perp} C_n C_{n-1} Y_{n-1} = \mu_n H_{x,n}, \quad (4.5b)$$

where  $n = N$ .

In the numerical calculation, we set the values of  $H_{x,n}$  and  $H_{y,n}$  to zero, except for the case of the  $n^{\text{th}}$  disk, where an excitation of vortex gyration is triggered by an external field (i.e.,  $n=1$ , when triggered at the left disk,  $n = (N+1)/2$  (for odd  $N$ ) or  $N/2$  (for even  $N$ ), when triggered at the center of the array).

Note that the chirality dependence of the governing equation can be eliminated by multiplying  $C_n$  to the core position vector  $\mathbf{X}_n$  of a given  $n^{\text{th}}$  disk. For an arbitrary  $C$  configuration in a given chain, therefore, we can consider only the parallel and antiparallel  $p$  ordering between the nearest-neighbor (NN) disks. In this case,  $C_n \cdot X_n$  and  $C_n \cdot Y_n$  correspond physically to the  $-y$  and  $x$  components of the in-plane net magnetization, respectively, which is induced by the shift of the vortex core from its center position; Eqs. (4.3-4.5) can be regarded as the force-balance equations of the dipolar forces between the NN disks.

Using the above equations, for a certain value of  $N$ , we can

numerically calculate coupled vortex gyrations of  $N$  individual disks. The numerical values of  $\omega_0 = 2\pi \times 235 \text{ MHz}$ ,  $G = 1.77 \times 10^{-12} \text{ Js/m}^2$ ,  $\kappa = 2.62 \times 10^{-3} \text{ J/m}^2$ , and  $D = -4.66 \times 10^{-14} \text{ Js/m}^2$  are obtained from micromagnetic simulations performed on an isolated disk. We also obtain  $\eta_{\parallel} = 9.36 \times 10^{-5} \text{ J/m}^2$  and  $\eta_{\perp} = 2.56 \times 10^{-4} \text{ J/m}^2$  from further micromagnetic simulations performed on a coupled two-disk system of the same dimensions and interdistance as those used in this study, based on the relation<sup>S8</sup> of  $\Delta\omega_{p_1 p_2} = \omega_0(\eta_{\perp} - p_1 p_2 \eta_{\parallel})/\kappa$ , where  $\Delta\omega = 2\pi \times 30 \text{ MHz}$  for  $p_1 p_2 = -1$  and  $2\pi \times 15 \text{ MHz}$  for  $p_1 p_2 = 1$ .

## 4.4 Discrete wave modes of collective vortex gyration in finite number of disks

### 4.4.1 Discrete wave modes for $N$ coupled-vortex dynamics.

In order to clarify the collective behavior of the distinct modes of collective vortex-gyration excitation in a coupled disk chain of finite disk number  $N$ , we numerically calculate frequency spectra in the individual disks from fast Fourier transform (FFT) of vortex motions for the same dimensions and material parameters as those of the real sample, but with the zero-damping constant for three cases of  $N=2, 3$  and  $4$ , for example. As shown at the top of FIG. 4.3, for  $N=2$ , two distinct peaks appear in both disks, but for  $N=3$ , there are three peaks in disks 1 and 3 and only two peaks in disk 3. For  $N = 4$ , four peaks appear in all of the disks. These results clearly indicate that  $N$  normal modes appear for a coupled  $N$ -disk chain. Each mode is labeled by  $\omega_i$  with  $i = 1, 2, \dots, N$ . To see the collective behavior of each mode, we plotted the spatial distributions of the individual cores (top) and the corresponding displacement profiles of  $C_n Y_n$  (bottom, right) for the individual modes in a given system of  $N$ , as obtained from the inverse FFTs of all of the peaks of all the disks for a given  $\omega_i$  mode. The

$C_n Y_n$  component profiles (bottom, right) represent wave forms (red dotted or solid lines) of certain wave numbers. In accordance with the result for two dipolar-coupled vortex oscillators noted in earlier reports[50, 51, 53, 54], the lower-frequency mode shows in-phase motion of the  $C_n Y_n$  component between disks 1 and 2, whereas the higher-frequency mode reveals anti-phase motion of the  $C_n Y_n$  component between disks 1 and 2. These two normal modes perfectly agree with standing waves of  $k = \pi/(3d_{\text{int}})$  and  $k = 2\pi/(3d_{\text{int}})$ . For the case of  $N=3$ , there exists a standing-wave node (that is represented by no core motion in the middle disk) for the  $\omega_2$  mode. This no-motion results in the absence of the  $\omega_2$  mode's peak in the frequency spectra of disk 2. While, for the case of  $N=4$ , the disappearance of specific mode's peaks in the spectra does not happen. The reason is because any node is no longer located inside any disk of the entire chain. Note that the nodes can be observed only at the condition of  $\sin(\mathbf{k} \cdot \mathbf{R})=0$ , where  $\mathbf{R} = nd_{\text{int}} \hat{\mathbf{x}}$  and  $\mathbf{k} = m\pi/[(N+1)d_{\text{int}}] \hat{\mathbf{k}}$  with  $m = 1, 2, \dots, N$ . Thus, the nodes of standing waves are located inside the  $n^{\text{th}}$  disk for the case where the constraint of  $l\pi = nd_{\text{int}} \cdot [m\pi/\{(N+1)d_{\text{int}}\}]$  is satisfied, where  $l$  is an integer.

Strikingly, those coupled vortex-gyration modes in the 1D chains of a given finite disk number are in excellent agreement with standing-wave forms of wave numbers,  $k = m\pi/[(N+1)d_{\text{int}}]$ , where  $m = 1, 2, \dots, N$ . In the

numerical calculation of coupled vortex gyrations for a given  $N$ -disk system, although we do not assume a fixed boundary condition, all of the individual collective modes are completely pinned at both ends of the imaginary disks with the equal interdistance of  $d_{\text{int}}$ , (i.e., the  $0^{\text{th}}$  and  $N+1^{\text{th}}$  disk), so that we can adopt the fixed boundary condition of standing waves.

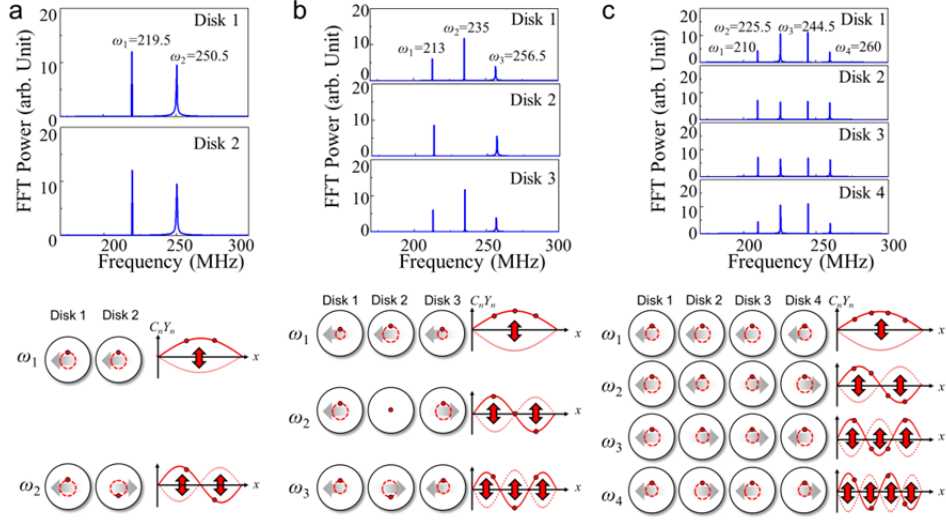


**FIG. 4.3.** Frequency spectra and corresponding spatial distributions of distinct normal modes of dipolar-coupled magnetic disks of given disk numbers (a,  $N=2$ , b,  $N=3$ , and c,  $N=4$ ). For all of the cases, the polarization ordering is indicated as  $p_n = (-1)^{n+1}$  while holding counter-clockwise chirality ( $C_n = +1$ ), where  $n$  indicates the  $n^{\text{th}}$  disk in a given chain. All the data are obtained from the FFTs of the  $C_n \mathbf{X}_n$  components of the collective oscillatory motions of the individual disks calculated using coupled linearized Thiele equations. The core trajectories are noted by the dashed lines inside the individual disks. Each dot on each trajectory represents the core position in the given disk. The wave profiles of the  $C_n Y_n$  components of the collective core motions are indicated by the red-colored solid ( $t=0$ ) and dashed ( $t=T/2$ , where  $T=2\pi/\omega$ ) lines.

#### 4.4.2 Discrete wave modes in real sample.

Based on the knowledge in the section 4.1.1, to illustrate the collective vortex-gyration modes excited in the real sample, we plot the frequency spectra (red circles) of core motions in the individual disks as obtained from fast Fourier transformation (FFT) of the core position vector  $\mathbf{X}_n$  multiplied by  $C_n$  in the  $n^{\text{th}}$  disk [See FIG. 4.4(a)]. We also compare the experimental results with micromagnetic simulation (green circles) for the five-disk model system and numerical calculation (blue circles) based on five coupled linearized Thiele equations. Because of the intrinsic damping of core gyration in isolated disks, the peaks are broadened and overlapped with neighboring peaks to an extent, that they cannot be separated. Further deviations between the experimental data and micromagnetic simulations as well as numerical calculations can be attributed to sample imperfections and the chosen time steps (400 ps) between the snapshot images taken by STXM. Specifically, with regard to disks 2 and 4, only one peak of wide width appears in the experimental data whereas two peaks appear in the simulations and numerical data. In contrast, two clear peaks and a very weak third peak appear in disks 1 and 3, which is in quantitative agreement with the micromagnetic simulation and numerical calculation.

In order to clarify the presence of fundamental discrete modes, we conduct further numerical calculation of coupled Thiele equation on a five-

disk model of the same dimensions and material parameters as those in the real sample, but with zero damping. The right panel of FIG. 4.4a shows the characteristic frequency spectrum of each disk. From disk 1 through disk 5, different peaks of contrasting FFT powers are observed. All of the five distinct peaks marked by  $\omega_i$  (where  $i = 1, 2, 3, 4, 5$ ) are shown in disks 1 and 5. By contrast, the  $\omega_3$  peak disappears in disks 2 and 4, while the  $\omega_2$  and  $\omega_5$  peaks disappear in disk 3. Each of the peaks of all of the modes is located at the same position in all of the disks.

From the inverse FFT of all of the peaks of each mode, we extracted the spatial correlations of core motions in the individual disks for each mode  $\omega_i$ . FIG. 4.4(b) shows the trajectories of the orbiting cores in motion in the individual disks along with the profiles of the  $C_n Y_n$  component of the core positions in the five-disk array. For all of the modes  $\omega_i$ , the individual core's gyration amplitudes are markedly distinct among the disks and modes. More interestingly, the collective motions of the individual cores in the whole array represent certain wave forms of different wavelengths. The gyration amplitudes for all of the modes are symmetric with respect to the center of the array, and are also completely pinned at imaginary disks at both ends, denoted disk 0 and disk 6 for the case of  $N = 5$ . These features represent a standing-wave form of a certain wavelength in terms of collective vortex-gyration motions, being quite analogous to a string, the ends of which are attached to the left and right walls respectively, thus having no displacement.

Based on the above results, we can interpret the collective and discrete wave modes as in the no-damping case, based on the fixed boundary condition in such a 1D array of finite disk number  $N$ . In this case, the boundary condition is given as  $\psi|_{x=0} = \psi|_{x=(N+1)d_{\text{int}}} = 0$ , where  $\psi$  denotes the displacement of beads,  $N$  is the number of elements, and  $d_{\text{int}}$  is the inter-distance between the elements. From this boundary condition, the wave vectors of the allowed modes can be expressed simply as  $k = m \cdot \pi / [(N+1)d_{\text{int}}]$ , where  $m = 1, 2, \dots, N-1$ , and  $N$ . Thus, the discrete (quantized) five modes' wave numbers of the collective vortex gyrations in the five-disk array are coincident with the values of  $k_m = m\pi/6d_{\text{int}}$ , where  $m=1, 2, 3, 4, 5$ .

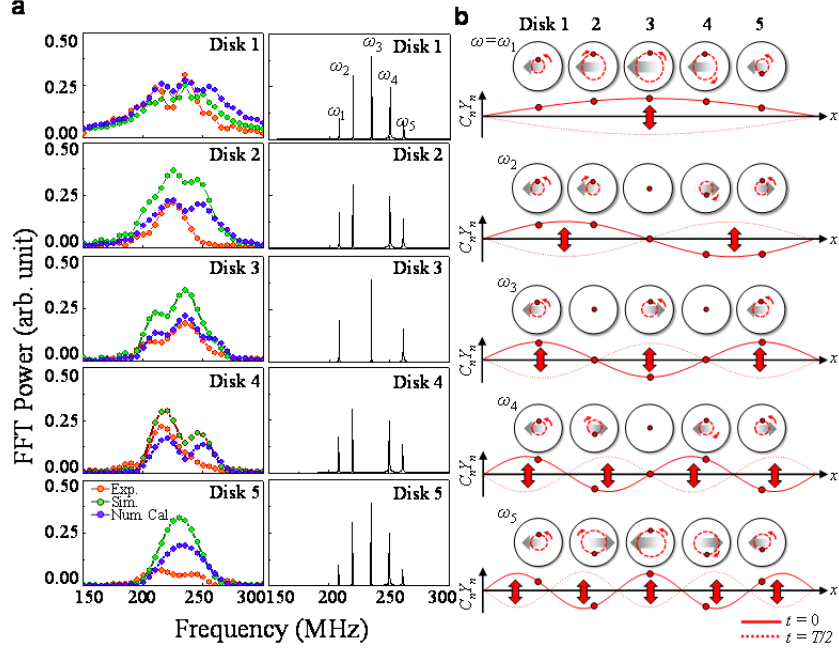


**FIG. 4.4** (a) Frequency spectra obtained from the experimental data, the micromagnetic simulation and the numerical calculation (FFTs of the numerically calculated oscillatory  $C_n \mathbf{X}_n$  of the individual disks). The right column shows the numerically calculated frequency spectra for zero damping ( $\alpha = 0$ ). (b), Spatial distributions of the individual disks' core positions for the five discrete modes. The core trajectories are noted by the dashed lines inside the individual disks. Each dot on each trajectory represents the core position in the given disk. Just below each mode, the corresponding profile of the  $C_n Y_n$  components is indicated by the solid line (for  $t = 0$ ) or dotted line ( $t = T/2$ ), where  $T = 2\pi / \omega$  is a time period for one cycle of gyration. In all of the FFTs, we applied the zero-padding technique to obtain 5 MHz resolution, except for  $\alpha = 0$ .

## 4.5 Dispersion relations of collective vortex gyration in 1D arrays of finite number of disks

In the previous section, we found that the collective vortex-gyration modes represent standing waves of discrete wavelengths (i.e., quantized  $k$  values). Then, we extract the dispersion relation ( $\omega - k$  relation) of all of the modes. For that, we perform FFTs of the collective core profiles for the individual modes according to  $k_m = m\pi/6d_{\text{int}}$  (where  $m=1, 2, 3, 4, 5$ ) with a fixed value of  $d_{\text{int}}=2250$  nm for the real sample. Figure 4.5 shows the FFT powers in the  $\omega$ - $k$  spectra obtained from the experimental data, micromagnetic simulation (for  $\alpha =0.01$ ) and numerical calculation of coupled Thiele equation (for both cases of  $\alpha =0.01$  and  $\alpha=0$ ). FFTs of each of the  $X_n$  and  $Y_n$ , multiplied by  $C_n$  (i.e.,  $C_n \cdot X_n$  and  $C_n \cdot Y_n$ ), are performed. Using such reduced parameters of  $C_n X_n$  and  $C_n Y_n$ , we can consider only the polarity ordering for comparison between experimental and numerical calculation data.

The overall shape of the dispersion from the experimental data qualitatively agrees well with those from the micromagnetic simulations and numerical calculation, though they show quantitative discrepancy in the frequency and FFT power between each mode. As already mentioned above, discrepancies might be associated with the chosen measurement parameters,

sample imperfections as well as a difference in the saturation magnetization between the experiment and micromagnetic simulations. The white solid lines indicate the result of an analytically derived explicit form for a 1D infinite array. As noted earlier, the intrinsic damping of vortex-core gyration in isolated disks causes the broadening of the  $\omega$  values (see FIG. 4.5). For the case of no-damping, five discrete quantized modes without the  $\omega$ -value broadening are distinctly shown in the spectra (right panel).

Next, note that the overall shape of dispersion is concave down, that is, a higher frequency at  $k=0$  and a lower frequency at  $k=\pi/d_{\text{int}}$  for the case of  $C_n X_n$ , and concave up (vice versa) for  $C_n Y_n$ . This reversal between  $C_n X_n$  and  $C_n Y_n$  can be understood in terms of the lattice-number-dependent phase difference between the  $x$  and  $y$  components of the vortex-core positions. Since the gyration's rotational sense is determined by the polarization  $p$  of a given disk, the phase difference between the  $x$  and  $y$  components of the core position vector in the  $n^{\text{th}}$  disk is given as the product of  $\pi/2$  and  $p_n$ . Accordingly, for the case of the antiparallel polarization between the NN disks as in the sample, the phase difference between the  $x$  and  $y$  components can be expressed as  $\mathbf{R} \cdot \left( \frac{\pi}{d_{\text{int}}} \hat{\mathbf{k}} \right) - \frac{\pi}{2}$ , where  $\mathbf{R} = nd_{\text{int}} \hat{\mathbf{x}}$ . This results in the shift of the  $k$ -vector in reciprocal space, as  $k' = k - \pi/d_{\text{int}}$ . Considering the real value of  $\pi/d_{\text{int}} = 1.3963 \mu\text{m}^{-1}$  for  $d_{\text{int}} = 2250 \text{ nm}$ , the experimental data

are fully consistent for the  $k$  shift by  $\pi/d_{\text{int}}$  between  $C_n X_n$  and  $C_n Y_n$ , as shown in FIG. 4.5

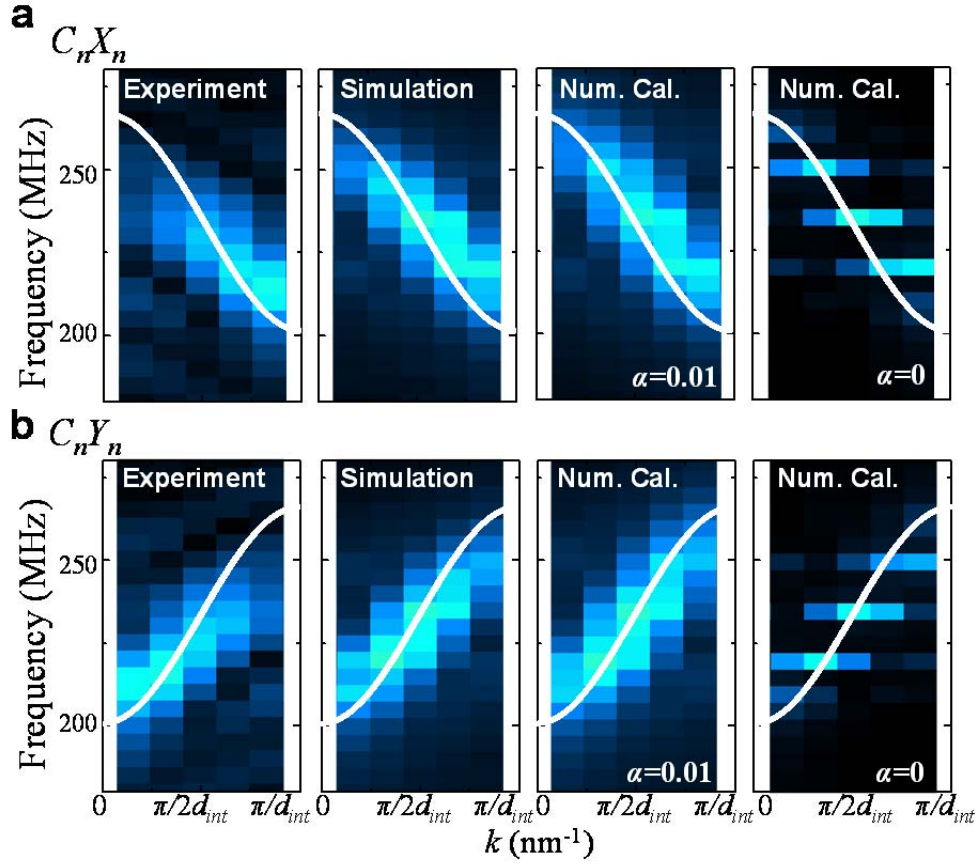


**FIG. 4.5** Dispersion relations for all excited collective modes, as extracted from FFTs of coupled oscillations of the vortex-core position vector  $\mathbf{X}_n$  multiplied by  $C_n$ , i.e. (a)  $C_n X_n$  and (b)  $C_n Y_n$ , obtained from experimental data, micromagnetic simulations, and numerical calculations with damping ( $\alpha = 0.01$ ) and without damping ( $\alpha = 0$ ). The white line indicates the analytically obtained dispersion curve for a 1D infinite array of the same dimensions and interdistance as in the simulations.

## 4.6 Dispersion relation in 1D magnetic vortex-based magnonic crystal of infinite or semi infinite number of disks

In this section, we derive an explicit analytical form of dispersion for a 1D infinite disk array using the linearized Thiele equation of motion[80, 81], taking into account the potential energy modified by dipolar interaction[43] between only the NN disks of parallel and antiparallel polarization and chirality ordering: Type I:  $[p_n, C_n] = [(-1)^{n+1}, 1]$  for the antiparallel  $p$  and parallel  $C$  ordering; Type II:  $[(-1)^{n+1}, (-1)^{n+1}]$  for the antiparallel  $p$  and  $C$  ordering; Type III:  $[1, 1]$  for the parallel  $p$  and  $C$  ordering, and Type IV:  $[1, (-1)^{n+1}]$  for the parallel  $p$  and antiparallel  $C$  ordering. For simplicity, here, we assume 1D arrays of infinite disk number.

Then, the governing equation for the  $n^{\text{th}}$  disk can be expressed as

$$-p_n G(dY_n/dt) - D(dX_n/dt) + \kappa X_n + \eta_{\parallel} C_n (C_{n+1} X_{n+1} + C_{n-1} X_{n-1}) = 0, \quad (4.6a)$$

$$p_n G(dX_n/dt) - D(dY_n/dt) + \kappa Y_n - \eta_{\perp} C_n (C_{n+1} Y_{n+1} + C_{n-1} Y_{n-1}) = 0, \quad (4.6b)$$

Considering the phase difference between  $X_n$  and  $Y_n$ , the general solutions can be expressed as  $X_n = \tilde{X} e^{i(ka_n - \omega t)}$  and  $Y_n = \tilde{Y} e^{i(ka_n - \omega t + \pi p_n / 2)}$  with  $a_n = n d_{\text{int}}$ ,

where  $d_{\text{int}}$  is the center-to-center distance. Here  $\tilde{X}$  and  $\tilde{Y}$  are constants to be determined, whose ratio will specify the relative amplitude and phase of the gyrating effective magnetization within a unit cell. Incorporating these general solutions into Eqs. (4.6a) and (4.6b) yields

$$\omega_0(1+D^2/G^2)\left[i\omega(D/G)/\left(\omega_0(1+D^2/G^2)\right)+1+C_n\left(C_{n+1}e^{ikd_{int}}+C_{n-1}e^{-ikd_{int}}\right)(\eta_{\parallel}/\kappa)\right]\tilde{X}-\omega\tilde{Y}=0 \quad (4.7a)$$

$$-\omega\tilde{X}+\omega_0(1+D^2/G^2)\left[i\omega(D/G)/\left(\omega_0(1+D^2/G^2)\right)+1-C_n\left(C_{n+1}p_n p_{n+1}e^{ikd_{int}}+C_{n-1}p_n p_{n-1}e^{-ikd_{int}}\right)(\eta_{\perp}/\kappa)\right]\tilde{Y}=0 \quad (4.7b)$$

with  $\omega_0 \equiv \kappa G / (G^2 + D^2)$ . According to the condition that the determinant of the  $2 \times 2$  matrix is zero, the dispersion is given as

$$\omega^2 = \omega_0^2(1+D^2/G^2)^2 \left[ 1 + i\omega(D/G) / \left( \omega_0(1+D^2/G^2) \right) + C_n \left( C_{n+1}e^{ikd_{int}} + C_{n-1}e^{-ikd_{int}} \right) (\eta_{\parallel}/\kappa) \right] \times \left[ 1 + i\omega(D/G) / \left( \omega_0(1+D^2/G^2) \right) - C_n \left( C_{n+1}p_n p_{n+1}e^{ikd_{int}} + C_{n-1}p_n p_{n-1}e^{-ikd_{int}} \right) (\eta_{\perp}/\kappa) \right]. \quad (4.8)$$

For the case of zero damping and for the given parallel and antiparallel  $p$  and  $C$  ordering, Eq. (4.8) can be rewritten as  $\omega^2 = \omega_0^2 \zeta_{\parallel}^2 \zeta_{\perp}^2$  with  $\zeta_{\parallel}^2 = 1 + 2C_n C_{n+1} (\eta_{\parallel}/\kappa) \cos(kd_{int})$  and  $\zeta_{\perp}^2 = 1 - 2C_n C_{n+1} p_n p_{n+1} (\eta_{\perp}/\kappa) \cos(kd_{int})$ .

In this case, the wave vector  $k$  has a continuous value due to the infinite number of existing modes in such an infinite 1D array. This explicit analytical form indicates that the dispersion relation is a function of an isolated disk's eigenfrequency  $\omega_0$  and the coupling strength between the NN disks, that is,  $\eta_{\parallel}$  and  $\eta_{\perp}$ , as well as those special  $p$  and  $C$  ordering.

From the Eq. 4.8, the group velocity is then given as

$$v_g = \partial\omega/\partial k = d_{int} \omega_0 C_n C_{n+1} \left[ p_n p_{n+1} (\eta_{\perp}/\kappa) (\zeta_{\parallel}/\zeta_{\perp}) - (\eta_{\parallel}/\kappa) (\zeta_{\perp}/\zeta_{\parallel}) \right] \sin kd_{int}. \quad (4.9)$$

For all of the  $p$  and  $c$  orderings, the group velocity is zero at  $k=0$  and  $k_{BZ}$ . All of the individual cores at  $k=0$  coherently move together, while for  $k=k_{BZ}$  standing-wave forms result in nodes at every disk. This analytical form

indicates that the group velocity can be manipulated by the selection of constituent materials, the dimensions of each disk, the separation distance as well as the  $p$  and  $C$  ordering.

The numerical calculation of the analytical form of  $\omega^2(k) = \omega_0^2 \zeta_{\parallel}^2(k) \zeta_{\perp}^2(k)$  for four different types of vortex-state ordering, noted above are displayed by the white lines in FIG. 4.6a, which are in excellent agreement with the dispersion spectrum from the FFTs of the  $X_n$  components of the individual disks, which are obtained from the numerical calculation of  $N$  coupled Thiele equations for the  $N=201$  system with damping ( $\alpha=0.01$ ). While performing the FFTs, we imposed a periodic boundary condition to describe such a semi-infinite system in terms of traveling waves. Accordingly, the resultant  $k$ -values are given as  $k = m \cdot (2\pi / Nd_{\text{int}})$ , where  $m$  is any integer value under the constraint of  $-\frac{\pi}{d_{\text{int}}} < k \leq \frac{\pi}{d_{\text{int}}}$ . All of the dispersion curves are symmetric with respect to  $k=0$ , because the gyration is supposed to propagate from the center towards both ends.

We stress here that the overall shape of dispersion is determined by the sign of  $p_n p_{n+1} C_n C_{n+1}$ ; such that concave up for  $p_n p_{n+1} C_n C_{n+1} = 1$ , and concave down for  $p_n p_{n+1} C_n C_{n+1} = -1$ . Also, the band width is wider for the case of the antiparallel  $p$  ordering than for the parallel  $p$  ordering. The band-

width variation in the  $p$  ordering reflects the fact that the opposite polarization between NN disks has a stronger dipolar interaction (resulting in large frequency splitting) than does the same polarization, as noted in earlier reports[50, 51, 53, 54]. This is caused by the rotational sense of stray fields around a given disk that is opposite to that of the core gyration. A rotating field efficiently couples into the circular eigenmode of gyration when the sense of rotation of the stray field coincides with the sense of gyration. Consequently, the dipolar interaction between NN disks having the opposite polarization is stronger than that between those having the same polarization.

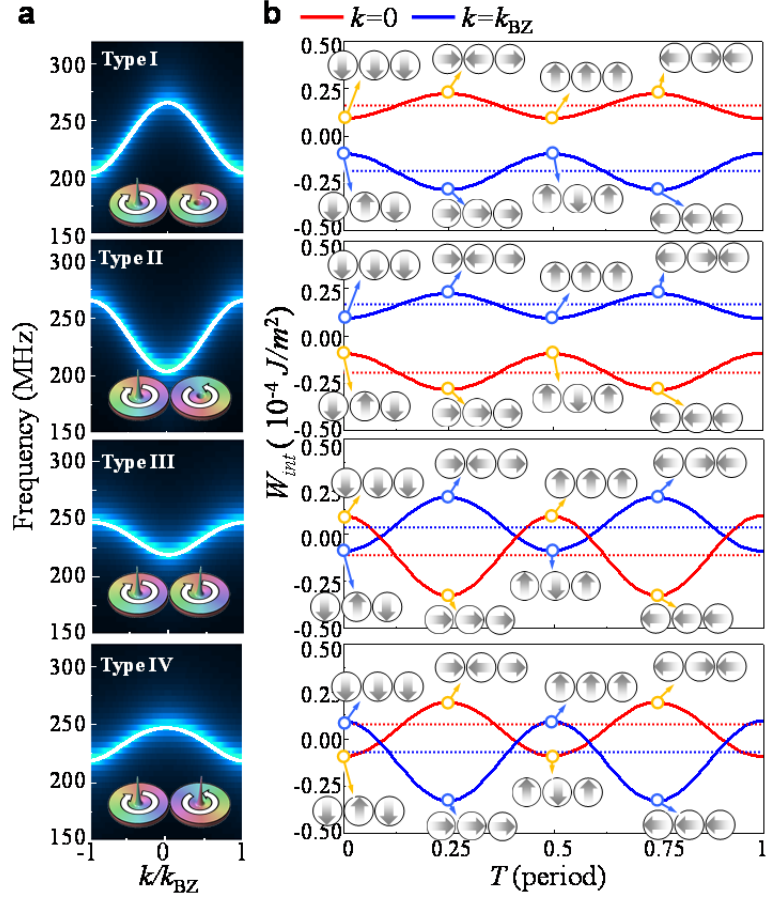


**FIG. 4.6** (a) Dispersion relations of numerical calculation (blue-color spectra) for  $N=201$  for which core gyration in the middle (101th disk) of the whole array is displaced to  $\sim 200$  nm, and of the numerical calculation (white thick lines) of the analytically derived equation for a 1D infinite array. (b) Dynamic dipolar interaction energy densities as a function of time for both  $k=0$  and  $k=k_{BZ}$ , which are obtained from the analytical form of an infinite 1D array. The gray-colored wide arrows in each disk indicate the effective net magnetizations  $\langle \mathbf{M}_n \rangle$  induced by core shifts at the given core

positions. The size does not indicate the magnitude of the dynamic effective magnetizations. Specific  $\langle \mathbf{M}_n \rangle$  configurations are indicated by three disks and corresponding gray arrows.

#### 4.7 Phase relation of the net in-plane magnetizations between the NN disks and dispersion relations

To understand the variation of dynamic dipolar interaction between the NN vortices with the  $p$  and  $C$  ordering, we qualitatively determine the phase difference between two magnetic dipoles, which is to say, the net in-plane magnetizations  $\langle \mathbf{M} \rangle$  of two NN disks. The  $\langle \mathbf{M}_n \rangle$  of a given  $n^{\text{th}}$  disk is induced by a shift of the vortex core from its center position. From earlier work[84], it can be simply expressed, in terms of chirality  $C$  and the vortex-core's position vector  $\mathbf{X} \equiv X\hat{\mathbf{x}} + Y\hat{\mathbf{y}}$ , as

$$\mathbf{m} \equiv V \cdot \langle \mathbf{M} \rangle_V \equiv \zeta C (Y\hat{\mathbf{x}} - X\hat{\mathbf{y}}) \quad (4.10)$$

where  $X$  and  $Y$  represent the  $x$  and  $y$  components of the core displacement, respectively. Then, the effective magnetization in the  $n^{\text{th}}$  disks for a certain mode of  $\omega$  has the form

$$\mathbf{m}_n = \zeta RC_n (\hat{\mathbf{x}} \sin p_n \omega t - \hat{\mathbf{y}} \cos p_n \omega t) \quad (4.11)$$

where  $p_n$  and  $\omega$  denote the vortex core's polarization in the  $n^{\text{th}}$  disk and the

angular frequency for a given mode, respectively.  $\zeta$  is the proportionality constant, which is determined by the analytical model of vortex structure, and  $R \equiv \sqrt{X^2 + Y^2}$ . For simplicity, we set the initial phase of the  $n^{\text{th}}$  disk to zero so that the initial orientation of  $\langle \mathbf{M}_n \rangle$  at  $t=0$  is in the  $-y$  (for  $C_n=+1$ ) direction, except for  $R=0$ .

From the general solutions shown in the chapter 4.3 since the phase delay of the vortex-core position between the NN disks is given as  $kd_{\text{int}}$  for a certain  $k$  value, the effective magnetization vector in the  $n+1^{\text{th}}$  disk takes the form of

$$\mathbf{m}_{n+1} = \zeta RC_{n+1} [\hat{\mathbf{x}} \sin(p_n \omega t + kd_{\text{int}}) - \hat{\mathbf{y}} \cos(p_n \omega t + kd_{\text{int}})] . \quad (4.12)$$

The phase difference  $\mathcal{G}$  between  $\mathbf{m}_n$  and  $\mathbf{m}_{n+1}$  can be obtained by the inner product of their unit vectors,  $\hat{\mathbf{m}}_n$  and  $\hat{\mathbf{m}}_{n+1}$ , and thus the phase difference can be expressed in terms of the polarization and chirality ordering between the NN disks as well as the angular frequency and wave vector of a given mode  $\hat{\mathbf{m}}_n \cdot \hat{\mathbf{m}}_{n+1} = \cos \mathcal{G} = C_n C_{n+1} \cos(kd_{\text{int}} - (p_{n+1} - p_n) \omega t)$ .

Thus,

$$\mathcal{G} = \mathcal{G}_0 - (p_{n+1} - p_n) \omega t \quad (4.13)$$

with  $\mathcal{G}_0 = kd_{\text{int}} + \pi(1 - \frac{1}{2} C_n C_{n+1})$ . For example, at  $k=0$  ( $k=k_{\text{BZ}}$ ), the initial phase difference,  $\mathcal{G}_0$ , between the neighboring disks'  $\langle \mathbf{M} \rangle$  can be simply expressed as  $\mathcal{G}_0 = \pi - \frac{\pi}{2} C_n C_{n+1}$  ( $\mathcal{G}_0 = -\frac{\pi}{2} C_n C_{n+1}$ ). Therefore, for

$k=0$ , if  $C_n C_{n+1}=1$  (-1), the initial phase difference between the neighboring disks'  $\langle \mathbf{M} \rangle$  has parallel (antiparallel) orientation along the  $y$  axis. In the case of parallel polarization ordering, since their relative phase is always the same, the neighboring disks'  $\langle \mathbf{M}_n \rangle$  are in parallel (antiparallel) orientation along both the  $x$  and  $y$  axes, and thus the average dynamic dipolar energy is at the next-lowest (next-highest) level. On the other hand, in the case of antiparallel polarization ordering, the neighboring disks'  $\langle \mathbf{M}_n \rangle$ , since their relative phase varies with time, are in parallel (antiparallel) and antiparallel (parallel) orientation along the  $y$  and  $x$  axes, respectively, and thus the average dynamic dipolar interaction energy is the highest (lowest), as clearly seen in Fig. 4.6b.

For  $k=\pi/d_{\text{int}}$ , if  $C_n C_{n+1}=1$  (-1), the neighboring disks'  $\langle \mathbf{M}_n \rangle$  are in antiparallel and parallel orientation along the  $y$  and  $x$  axes, respectively, for antiparallel polarization ordering, whereas they are in antiparallel (parallel) orientation along the two axes for the parallel polarization ordering. Thus, for the case of the antiparallel polarization ordering, the average dynamic dipolar energy is at the lowest (highest) frequency level, while it is at the next-highest (next-lowest) frequency level for the case of parallel polarization ordering.

## Chapter 5

### Collective Vortex Oscillation Modes in a 1D Chain

#### Consisting of Bi-component Constituents

Lattice vibration modes in solid crystals are strongly dependent not only on lattice symmetry and interaction strength but also on the basis consisting of a primitive unit cell. In the simplest case, that of single atoms in the primitive cell, only a single branch of dispersion appears. By contrast, bi-component atoms yield characteristic two-branch dispersions. Analogous to that, in order to investigate the effect of the constituents in the primitive unit cell on collective vortex-core gyration excitation and their dispersions in 1D array of coupled disks, we performed micromagnetic simulations in studying the effects of change in the primitive unit cells of 1D vortex arrays on collective vortex-gyration dispersion. As the primitive basis, we consider alternating constituent materials (NiMnSb vs. Permalloy) and alternating dimensions including constituent disk diameter and thickness. Furthermore, we analytically derive the dispersion relation of 1D arrays of coupled disks consisting of bi-component constituents, and compare the results with those from micromagnetic simulation.

## 5.1 Model geometry

Figures 5.1(a) and 5.1(b) show two different types of 1D vortex-state lattices comprised of 25 circular disks of single-material NiMnSb and alternating materials NiMnSb and Py, respectively. Each disk has an equal diameter ( $2R=213$  nm) and thickness ( $t=20$  nm), as well as an equal edge-to-edge distance  $d_{\text{int}}=15$  nm to its NN disks. The  $p$  and  $C$  states of the individual disks (noted as index  $n$ ) are maintained as  $[p_n, C_n]=[1,1]$ , where  $p=+1(-1)$  corresponds to the upward (downward) core magnetization and  $C=+1(-1)$  the counter-clockwise (clockwise) in-plane curling magnetization. Here the lattice constants of the two different types of the primitive basis are denoted  $a_S = 2R+d_{\text{int}}$  for the single-material array and  $a_A=2a_S$  for the alternating-material array.

On the two different bases shown in FIG. 5.1, we conducted micromagnetic numerical calculations using the OOMMF code (version, 1.2a4), in which the Landau-Lifshitz-Gilbert (LLG) equation is employed to numerically solve the motion of local magnetizations (cell size :  $3 \text{ nm} \times 3 \text{ nm} \times 20 \text{ nm}$ ). The material parameters corresponding to NiMnSb[97, 98] and Py are as follows: saturation magnetization  $M_s = 549 \times 10^3$  A/m (NiMnSb),  $860 \times 10^3$  A/m (Py); exchange stiffness constant  $A_{\text{ex}} = 1.0 \times 10^{-11}$  J/m (NiMnSb),  $1.3 \times 10^{-11}$  J/m (Py); Gilbert damping constant  $\alpha = 0.0023$

(NiMnSb), 0.01 (Py); anisotropy constant  $K = -1.0 \times 10^5 \text{ J/m}^3$  (NiMnSb), 0 (Py). To obtain all of the modes of coupled-vortex-gyration excitations in a given chain, we locally applied a static magnetic field  $H_x = 100$  Oe only to the  $n=13^{\text{th}}$  disk in the  $+x$  direction (the long axis of the chain). This local field allows the core of only the  $13^{\text{th}}$  disk to be shifted along the  $y$ -axis. After the field is turned off, a robust mechanism is set in train, whereby the vortex gyration of the  $13^{\text{th}}$  disk excites and, then, under free relaxation, immediately propagates along the long axis of the chain towards either end side. All of the simulation results noted hereafter were obtained within a time period of 200 ns after the field was turned off.

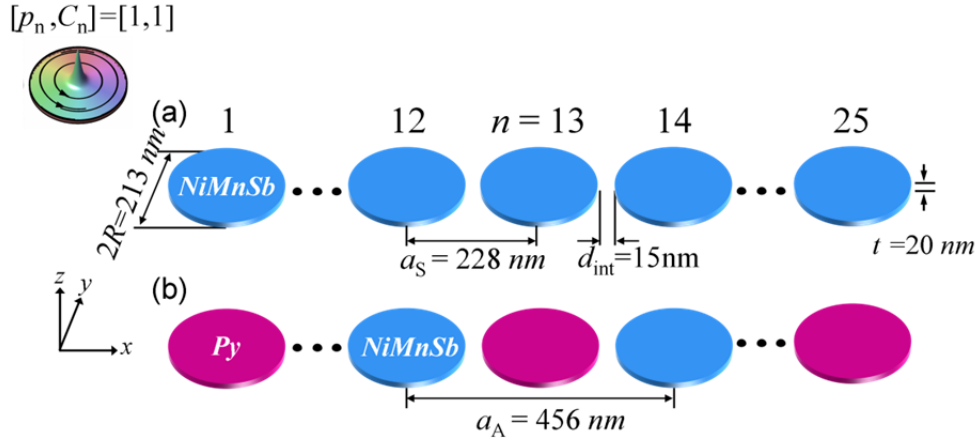


**FIG. 5.1.** Model geometry of 1D chains comprised of 25 disks of (a) single NiMnSb material and (b) alternating NiMnSb and Py materials, each disk having equal thickness  $t = 20 \text{ nm}$  and diameter  $2R = 213 \text{ nm}$ . The edge-to-edge interdistance between the nearest-neighbor (NN) disks is  $d_{\text{int}} = 15 \text{ nm}$ . The lattice constant is  $a_S = 2R + d_{\text{int}} = 228 \text{ nm}$  for the single-material array and  $a_A = 2a_S$  for the alternating-material array. Each disk has the same vortex state of upward ( $p=1$ ) and counter-clockwise ( $C=1$ ) in-plane curling magnetization, as illustrated by the perspective view of the vortex state shown in the inset.

## 5.2 Vortex-core gyration propagation in the 1D chain consisting of bi-component constituents

Figure 5.2(a) shows the simulation result of the temporal oscillations of the  $x$  and  $y$  components of the individual core-position vectors  $\mathbf{X}=(X, Y)$  for the NiMnSb single-material array shown in FIG. 5.1(a). The shifted core of the 13<sup>th</sup> disk began to gyrate with decreasing amplitude, whereas the cores in the neighboring disks exhibited gyrations of increasing amplitude followed by a decrease resulting from the transference of excited gyration to the NN disks. Beating patterns were observed in each disk, along with their modulation envelopes of the first-, second- and third-order wave packets, which maximum amplitude propagated along either side on the long axis of the given chain (in the figure, only the right-side results are shown). The beating patterns for the alternating-material array, by contrast, had a different appearance: the second- and third-order envelopes were smeared, and the oscillation frequencies in the NiMnSb disks (i.e., the 13<sup>th</sup> and 15<sup>th</sup> disks) were slower than those in the Py disks (i.e., the 14<sup>th</sup>, 16<sup>th</sup>, and 20<sup>th</sup> disks). This contrasting behavior was due to a large difference in the eigenfrequencies of the isolated disks between the two constituent materials ( $\omega_0=2\pi\times 535$  MHz for NiMnSb vs.  $2\pi\times 795$  MHz for Py). Plane-view images of the core displacements of the individual disks (see FIG. 5.2b) with

respect to distance and time clearly revealed the propagation of those vortex gyrations through the entire chains. For the case of the single-material array, two wavefronts were clearly observed, whereas for the alternative-material array, a weak and dispersive single wavefront appeared. The gyration propagation speeds were estimated from the average propagation speed of the 1<sup>st</sup> wave packet along the chains, which was  $\sim 65$  (42) m/s for the single (alternating)-material array.

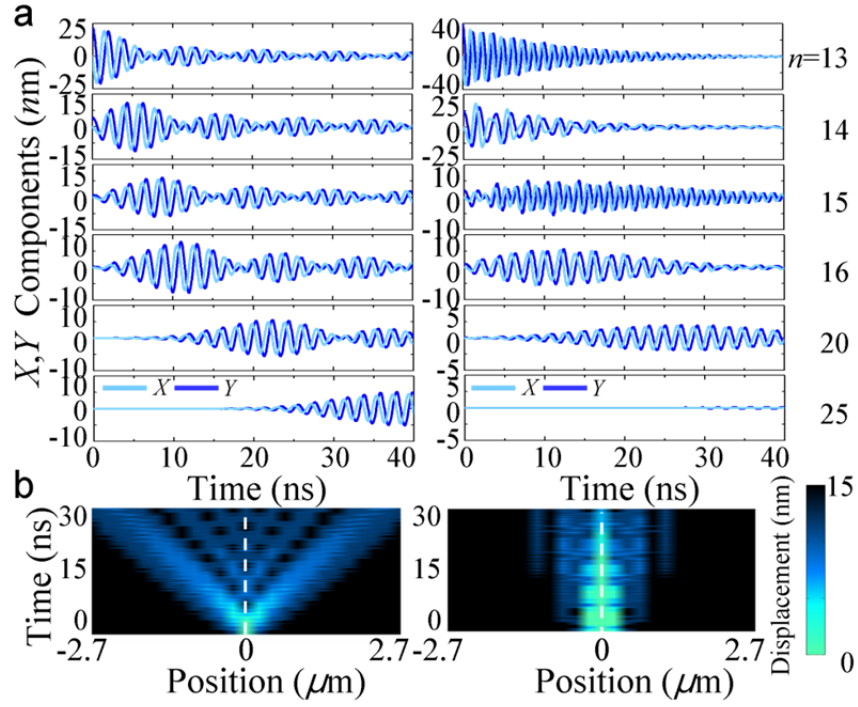


**FIG. 5.2** (a) Oscillatory  $x$  and  $y$  components of vortex-core-position vectors in given  $n^{\text{th}}$  disks, as indicated, and (b) their plane-view representations with respect to time and distance. The left and right columns correspond to the single (NiMnSb)-material and alternating (NiMnSb and Py)-material arrays, respectively. In (b), the color bar indicates the  $x$  component of the core displacements.

## 5.3 Dispersion relations in the 1D chain consisting of Bi-component Constituents

### 5.3.1 Micromagnetic simulations results

From fast Fourier transformations (FFTs) of the temporal oscillations of the core positions (here the  $x$  components) in all of the disks, shown in FIG. 2(a), we obtained the power spectra of dispersions (i.e., the  $f$ - $k$  relation), as shown in the first column of FIG. 5.3(a) and 5.3(b). In comparison, the overall shape of the dispersion curve for the single-material array was concave up; that is, the frequency was lowest at  $k=0$  and highest at  $k=k_{\text{BZ}}$ , where  $k_{\text{BZ}} = \pi/a_s$  for single-material arrays or  $\pi/a_A$  for alternating-material arrays. The band width was as wide as  $\sim 50$  MHz. By contrast, in the alternating NiMnSb and Py arrays, two distinct low and high branches in dispersion, relatively flat and of relatively narrow band width, were found. These two branches are analogous to the “*acoustic branch*” and “*optical branch*” of the lattice vibration modes of diatomic arrays.

For comparison, contrasting dispersions for the different vortex-state orderings are shown in the second, third, and last columns of FIG. 5.3(a) and 5.3(b). For both the single- and alternating-material chains, the band widths were wider for  $p_n = (-1)^{n+1}$  than for  $p_n = 1$ . This reflected the fact

that the opposite polarization between NN disks has a stronger dipolar interaction (resulting in large frequency splitting) than does the same polarization. For the single-material arrays, the overall shape of each dispersion curve depends on the sign of  $p_n p_{n+1} C_n C_{n+1}$ ; in other words, the shape is concave up for  $p_n p_{n+1} C_n C_{n+1} = 1$  and concave down for  $p_n p_{n+1} C_n C_{n+1} = -1$ . But in the alternating-material chain, the shape of the lower branch is concave up independently of the  $p$  and  $C$  orderings, while that of the higher branch varies according only to the  $p$  ordering: concave down for  $p_n p_{n+1} = -1$ , and almost flat for  $p_n p_{n+1} = +1$ . It was noticeable that as  $k$  approached  $k_{BZ}$ , the lower and higher branches approached the eigenfrequencies of the isolated NiMnSb and Py disks, specifically 535 and 795 MHz, respectively, independently of the  $p$  and  $C$  orderings. In the figures, the red dashed lines indicate the eigenfrequencies of the isolated disks.

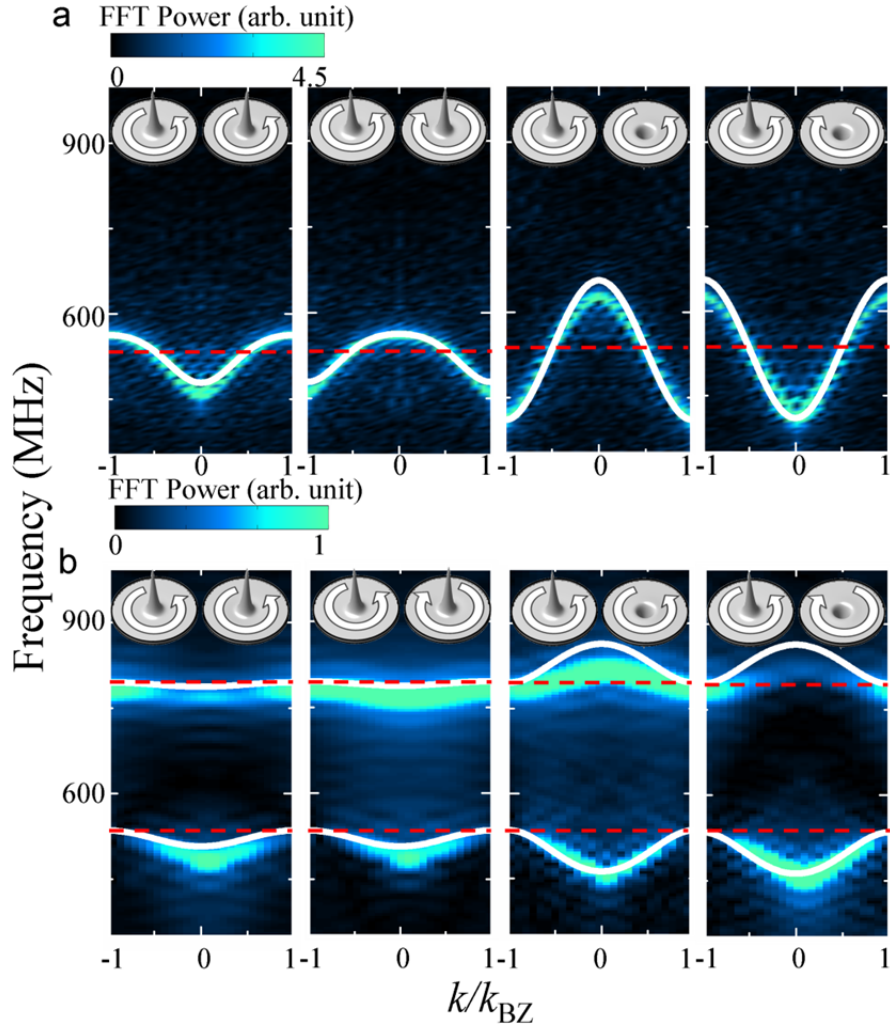


**FIG. 5.3** (color online) Dispersion relations of all collective vortexgyration excitations (using the  $x$ -component oscillations) in chains of (a) single NiMnSb material and (b) alternating NiMnSb and Py materials, for indicated four different  $[p_n, C_n]$  orderings. The white solid lines represent the numerical calculations using the explicit analytical forms for infinite chains. The red dashed lines indicate the eigenfrequencies of the isolated disks of the NiMnSb (535 MHz) and Py (795 MHz) materials.

### 5.3.2 Analytical derivation of dispersion relations

To gain more fundamental insights into the observed contrasting dispersions between the single- and alternating-material chains, including the additional degrees of freedom of the  $p$  and  $C$  orderings, we plotted the dispersion relations for infinite arrays (the white lines in FIG. 5.3), as numerically calculated from the explicit analytical forms[99]. The explicit form of dispersion relation for infinite chains composed of two A and B materials in the primitive unit cell were derived for four different  $p$  and  $C$  orderings, as  $\omega^2(k) = \xi_0(k) \mp \Delta\xi(k)$  with

$$\xi_0(k) = \frac{1}{2} \left[ \omega_{0A}^2 + \omega_{0B}^2 - 4p_A p_B \eta_{\parallel} \eta_{\perp} \frac{\omega_{0A}}{\kappa_A} \frac{\omega_{0B}}{\kappa_B} (\cos 2ka + 1) \right] \quad \text{and}$$

$$\Delta\xi(k) = \frac{1}{2} \left[ \left( \omega_{0A}^2 - \omega_{0B}^2 \right)^2 + 8 \left( \omega_{0A} \eta_{\parallel} - p_A p_B \omega_{0B} \eta_{\perp} \right) \left( \omega_{0B} \eta_{\parallel} - p_A p_B \omega_{0A} \eta_{\perp} \right) \frac{\omega_{0A}}{\kappa_A} \frac{\omega_{0B}}{\kappa_B} (\cos 2ka + 1) \right]^{1/2}$$

where  $\kappa_{A(B)}$  and  $\omega_{0A(B)}$  are the stiffness coefficient and angular eigenfrequency for an isolated A-(B-) material disk, respectively. The  $\eta_{\parallel}$  and  $\eta_{\perp}$  represent the dipolar interaction coefficient along the  $x$  (here  $x$  is the bonding axis)- and  $y$ -axes, respectively. The explicit analytical form for the alternating constituent materials has two frequency values at the given  $k$  values. Note that the previous report in Ref. [99] found that for a single material chain consisting of  $N$  identical disks, there exist  $N$  distinct modes of

corresponding angular frequency  $\omega$  and wave vector  $k$ . Accordingly, each single branch in dispersion that consists of  $N$  collective vortex-gyration modes is present. For the case of an alternating-material chain, at each of the  $N$  discrete values of  $k$ , there are two corresponding frequencies, leading to a total of  $2N$  normal modes, as is appropriate given the  $2N$  degrees of freedom. Also, the analytical forms tell us that the overall shape of dispersion curves varies only by the  $p$  ordering, not also by the  $C$  ordering, whereas for single-material arrays, the overall shape is determined by  $p_n p_{n+1} C_n C_{n+1}$ , as explained in FIG. 5.3. This is due to the fact that, for the case of alternating-material arrays, the two coupled vortex cores in the primitive unit cell move as a whole satisfying certain phase relation with its neighboring cells, i.e., they are in phase (out-of-phase) with its neighboring cells at  $k = 0$  ( $k = k_{BZ}$ ).

Next, we analyzed band widths according to the difference between  $\omega(k=0)$  and  $\omega(k=k_{BZ})$ .

For  $k=0$ , the  $\xi_0$  and  $\Delta\xi$  can be simplified as

$$\xi_0(k=0) = \frac{1}{2} \left[ \omega_{0A}^2 + \omega_{0B}^2 - 8p_A p_B \eta_{\parallel} \eta_{\perp} \frac{\omega_{0A}}{\kappa_A} \frac{\omega_{0B}}{\kappa_B} \right]$$

$$\Delta\xi(k=0) = \frac{1}{2} \left[ \left( \omega_{0A}^2 - \omega_{0B}^2 \right)^2 + 16 \left( \omega_{0A} \eta_{\parallel} - p_A p_B \omega_{0B} \eta_{\perp} \right) \left( \omega_{0B} \eta_{\parallel} - p_A p_B \omega_{0A} \eta_{\perp} \right) \frac{\omega_{0A}}{\kappa_A} \frac{\omega_{0B}}{\kappa_B} \right]^{1/2}$$

For  $k=k_{BZ}$ , those two values are simplified as  $\xi_0(k=k_{BZ}) = \frac{1}{2} (\omega_{0A}^2 + \omega_{0B}^2)$

and  $\Delta\xi(k=k_{BZ}) = \frac{1}{2} (\omega_{0A}^2 - \omega_{0B}^2)$ , so that  $\omega(k=k_{BZ})$  has both values of

$\omega_{0,A}$  and  $\omega_{0,B}$ , corresponding to the eigenfrequencies of the isolated disks of each of the A and B materials, respectively. On the basis of the result, the band gap can be derived as a form of  $\omega|_{k=0}^{higher} - \omega|_{k=k_{BZ}}^{lower}$  (for  $p_n=1$ ), and of  $\omega|_{k=k_{BZ}}^{higher} - \omega|_{k=k_{BZ}}^{lower}$  (for  $p_n = (-1)^{n+1}$ ), where  $\omega|_{k=k_a}^{higher(lower)}$   $\omega|_{k=k'}$  denotes the higher (lower) angular frequency at  $k=k'$ . For the case of  $p_n=1$ , since the width of the higher branch is so narrow,  $\omega|_{k=0}^{higher}$  approximates to  $\omega_{0,A}$  (or  $\omega_{0,B}$ ). Then, the band gap between two branches can be simply rewritten as  $|\omega_{0,A} - \omega_{0,B}|$ , irrespective of the  $p$  ordering. This means that the band gap can be determined mainly by the eigenfrequencies of each of the isolated disks.

## 5.4 Spatial profiles of coupled core motions for specific collective gyration modes

Next, we plot the spatial distributions of the collective vortex-gyration modes in two specific cases, of  $k=0$  and  $k = k_{\text{BZ}}$ . For a single-material chain in the simple case of  $[p_n, C_n]=[+1,+1]$ , synchronized coherent motion of all of the disks' vortex cores occurs for the  $k=0$  mode, as shown in FIG. 5.4(a)'s standing-wave motions of collective core motions with  $k= k_{\text{BZ}}$ . In the case of the chain with alternating NiMnSb and Py, at  $k=0$ , the vortices in the neighboring disks move in-phase (out-of-phase) with a large NiMnSb (Py)/Py (NiMnSb) gyration amplitude ratio for the lower (higher) branch. Such behaviors are quite similar to lattice vibration in the diatomic linear chain, where, in the acoustic mode, all ions within a primitive cell move in-phase or, in the optical mode, out-of-phase with one another. In the  $k=k_{\text{BZ}}$  mode, the collective vortex gyration behaves as a standing wave, of which nodes are located on the center of the Py (NiMnSb) disks for the lower (higher) branch. We here elucidate the underlying physics of contrasting dispersion as dependent on constituent-material ordering. Such characteristic band structures can be understood by the relative phase between the NN disks' effective magnetization  $\langle \mathbf{M}_n \rangle$  and their dynamic dipolar interaction energy, as discussed in Ref. [99]. As seen in FIG. 4, in

the case of the lower branch, at  $k=0$ , the initial relative phase of the NN disks'  $\langle \mathbf{M}_n \rangle$  is in the parallel orientation along the  $x$ -axis. Thus, for  $p_n=1$ , the NN disk's  $\langle \mathbf{M}_n \rangle$  is always in the parallel orientation along both the  $x$  and  $y$  axes, whereas for  $p_n=(-1)^{n+1}$ , the NN disk's  $\langle \mathbf{M}_n \rangle$  is in the parallel (antiparallel) orientation along the  $x$  ( $y$ ) axis. Then, their average dynamic dipolar energy is at the next-lowest and lowest level, respectively, and thus, the shape of the lower branch is concave up for both  $p$  orderings. In the case of the higher branch, however, when  $p_n=1$ , though the NN disk's  $\langle \mathbf{M}_n \rangle$  is in the antiparallel orientation along both the  $x$  and  $y$  axes, the dispersion curve is concave downward. This is due to the orbital shape of NiMnSb disks' vortex-core gyration, which is much elongated along the  $x$ -axis. Accordingly, the dipolar interaction energy in the antiparallel orientation along the  $y$ -axis plays a more dominant role in determining the average dipolar interaction energy than that in the antiparallel orientation along the  $x$ -axis.

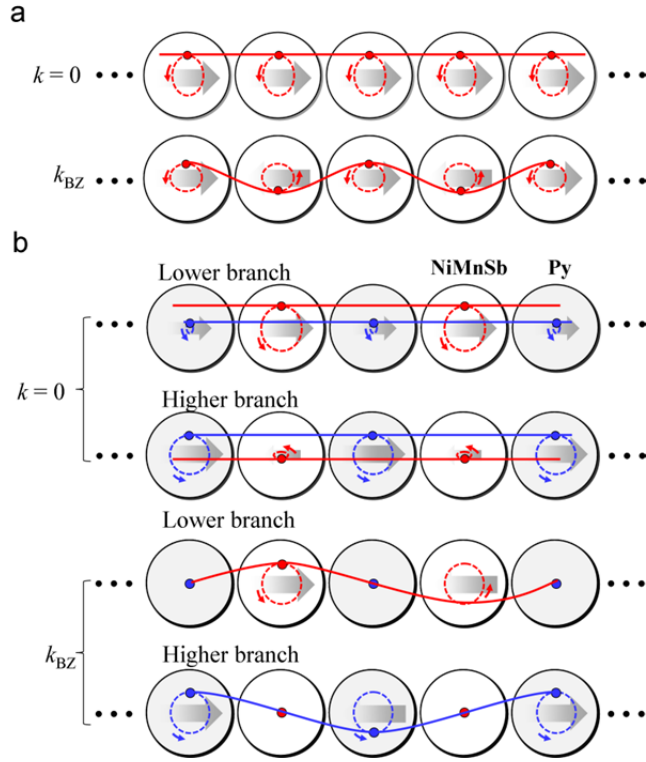


**FIG. 5.4** Spatial profiles of coupled core motions for specific collective gyration modes (e.g.,  $k = 0$  and  $k=\pi/a$ ) for (a) single-material and (b) alternating-material chains of given vortex state  $[p_n, C_n]=[1,1]$ . The core trajectories noted by the red (NiMnSb disks) and blue (Py disks) dashed lines inside the individual disks are the results of numerical calculations using the analytical forms for infinite 1D arrays. Each dot on each trajectory represents the core position in the given disk, which was plotted on the  $y$ -axis. The gray wide arrows indicate the net in-plane magnetizations induced by core shifts from the individual center positions. The gray arrows' size does not indicate the magnitude of the net in-plane magnetizations.

## 5.5 Different types of basis and their dispersion relations

It is well known that the eigenfrequency of isolated disks is given as  $\omega_0 = \kappa/G$  and that the gyrovector constant  $G$  and stiffness coefficient  $\kappa$  can be expressed in terms of disk dimensions  $\beta = t/R$  [75]. Thus, engineering the dimensions of constituent disks in the primitive unit cell would also give rise to two-branch dispersion, according to the derived explicit form of dispersion. We therefore conducted further simulations on chains comprising disks of (a) alternating diameter and (b) alternating thickness. Here, for simplicity, we consider only one specific vortex state of consistent disks, denoted as  $[p_n, C_n] = [1, 1]$ , in order to examine only the effect of alternating dimensions on band structures. As expressed in  $\omega(k) = \sqrt{\xi_0(k) \mp \Delta\xi(k)}$ , two branches appear at  $\omega_{R_1} = 2\pi \times 620$  and  $\omega_{R_2} = 2\pi \times 480$  MHz, which correspond to the angular eigenfrequencies of an isolated NiMnSb disk of  $2R_1 = 183$  and  $2R_2 = 243$  nm, respectively, and at  $\omega_{t_2} = 2\pi \times 870$  and  $\omega_{t_1} = 2\pi \times 535$  MHz, corresponding to the angular eigenfrequency of  $t_2 = 40$  nm and  $t_1 = 20$  nm, as represented by the dotted red lines in FIG. 5. Also, the shape of both the lower and higher branches is concave up, and the dispersion curves approach the eigenfrequencies of the isolated constituent disks as  $k$  approaches the first Brillouine zone (1st BZ) boundary, as seen in FIG. 5.4. The band gap between the higher and lower

branches is larger in the case of alternating thickness than in that of alternating diameters, since the band gap between the lower and higher branches is predominantly due to the gap in the eigenfrequencies of isolated constituent disks, as predicted in Eq. (2).

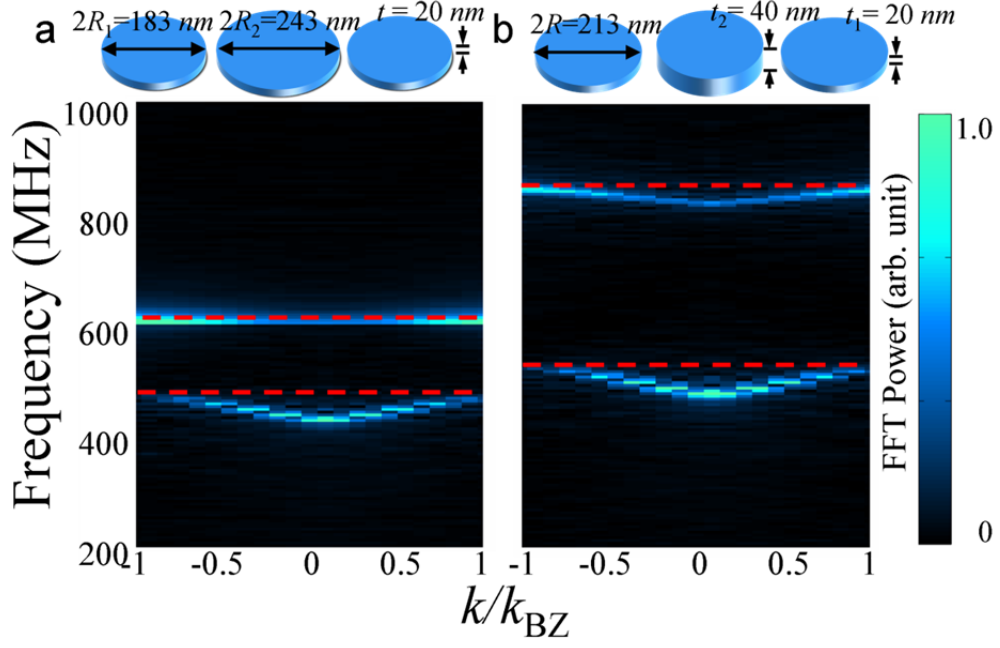


**FIG. 5.5** Dispersions of all excited collective vortex-gyration modes (using  $x$ -component oscillations) in chains comprised of disks of (a) alternating diameters ( $2R_2=183 \text{ nm}$  and  $2R_1=243 \text{ nm}$ ) with constant  $t=20 \text{ nm}$  and (b) alternating thickness ( $t_2=40 \text{ nm}$  and  $t_1=20 \text{ nm}$ ) with constant  $2R=213 \text{ nm}$ , as obtained from micromagnetic numerical simulations of 25 circular disks of single NiMnSb material and the same vortex state  $[p_n, C_n] = [+1, +1]$ . The red dashed lines correspond to the eigenfrequencies of an isolated single disk of given dimensions  $\omega/2\pi = 480, 620, 535, \text{ and } 870 \text{ Hz}$  for  $(2R_2=243, t=20)$ ,  $(2R_1=183, t=20)$ ,  $(2R=213, t_2=40)$ , and  $(2R=213, t_1=20) \text{ nm}$ , respectively.

## Chapter 6

### **Bias field control of $N$ -body coupled vortex oscillation**

In the previous chapters, we found that the eigenfrequencies of coupled vortex gyration as well as their dispersion relation in the two or more coupled-vortex oscillator can be tailored through their constituent materials, the isolated disks' dimension as well as vortex-polarization ( $p$ ) and chirality ( $C$ ) orderings between the nearest-neighboring (NN) disks.[99, 100]. However, those parameters are intrinsic for a given system, accordingly it is not easy to control the parameters for the given systems. Thus, finding a way to manipulate its dynamics with external parameters, meanwhile, remains a challenge.

Loubens *et al.*[97] and Yoo *et al.*[101] individually reported an experimental observation and numerical studies, respectively, about the effect of perpendicular bias magnetic field on the eigenfrequency  $\omega_0$  of vortex gyration in a isolated disk. These results showed that the parameters in Thiele equation (such as gyrovector  $G$  and stiffness coefficient  $\kappa$ ) as well as its resultant eigenfrequency are controllable by means of polarization,  $p$ , and the strength of the static magnetic field  $H_p$ . This finding provides a possible way to effectively tune the intrinsic parameters of the magnetic vortex via the external magnetic field.

In this chapter, we investigate the effect of perpendicular bias magnetic field on the dynamics in a pair and 1D arrays of dipolar-coupled vortices by means of analytical approach and micromagnetic simulations, and propose an efficient means of dynamic manipulation of the dispersion relation in vortex-state-disk-array magnonic crystals as well as the signal transfer speed through the coupled-vortex gyration.

## 6.1 Perpendicular bias field effect on an isolated disk

In order to obtain the numerical values of perpendicular-field-dependent parameters [97, 101], the micromagnetic simulations on an isolated disk was performed prior to the main calculations. For the simulations, we employed the OOMMF code which incorporates the Landau-Lifshitz-Gilbert (LLG) equation of motion of magnetization :  $\partial\mathbf{M}/\partial t = -\gamma\mathbf{M}\times\mathbf{H}_{\text{eff}} + (\alpha/M_s)\mathbf{M}\times\partial\mathbf{M}/\partial t$ , where  $\mathbf{H}_{\text{eff}}$  is the total effective field, which in the present case includes the demagnetization, exchange and external static perpendicular fields. Here, we used a permalloy (Py: Ni<sub>80</sub>Fe<sub>20</sub>) nanodisk of 303 nm radius and 30 nm thickness [FIG. 6.1(a)]. The typical Py material parameters of saturation magnetization  $M_s = 860\times 10^3$  A/m, exchange stiffness constant  $A_{\text{ex}} = 1.3\times 10^{-11}$  J/m, and Gilbert damping constant  $\alpha = 0.01$  were employed. Uniform static fields were applied perpendicularly to the disk plane, the strength of which fields varied from  $H_p = -15\text{kOe}$  to  $+15\text{kOe}$  at an interval of 100Oe. The positive (negative) sign corresponds to the parallel (antiparallel) orientation of the vortex-core magnetization (polarization  $p$ ) in the field direction.

Figure 6.1 (b) shows a numerically calculated typical hysteresis loop. As reported earlier, when the perpendicular field is introduced, the in-plane magnetizations in the initial ground state of the vortex structure begins

to be deviated from the in-plane at the edge and the intermediate area around the core due to the Zeeman energy term of the perpendicular field, and the vortex structure vanishes completely when the magnetic field reaches the saturation field  $H_s=9300\text{Oe}$ . The frequency spectrum and  $\kappa$  value as a function of  $H_p$  were plotted in FIG. 6.1(c) and (d), respectively. The value of  $\omega_0/2\pi$  at  $H_p=0$  is approximately 789 MHz, which increases monotonically to 970 MHz at  $H_p=2$  kOe and decreases to 605 MHz at  $H_p=-2$  kOe. The inset of FIG. 6.1(b) clearly reveals its linear dependence on  $H_p$ . Our simulation results and the analytical expression,  $\omega_0(H_p) = \omega_0(0) \left[ 1 + p(H_p/H_s) \right]$  were found to be in general agreement except for small difference in the slopes. The value of  $\kappa$  at  $H_p=0$  estimated to  $\sim 4.66 \times 10^{-3} \text{ J/m}^2$  decreases with increasing  $|H_p|$  as a parabolic shape [see FIG. 6.1 (d)]. The simulation results are somewhat asymmetric at about  $H_p=0$  in contrast to the explicit parabolic expression (solid line) of  $\kappa_0(H_p) = \kappa_0(0) \left[ 1 - (H_p/H_s)^2 \right]$ . The asymmetry of our result is due to the difference in the  $m_z$  profile of the vortex core between  $H_p$  and  $-H_p$ , as reported in Ref. [101].

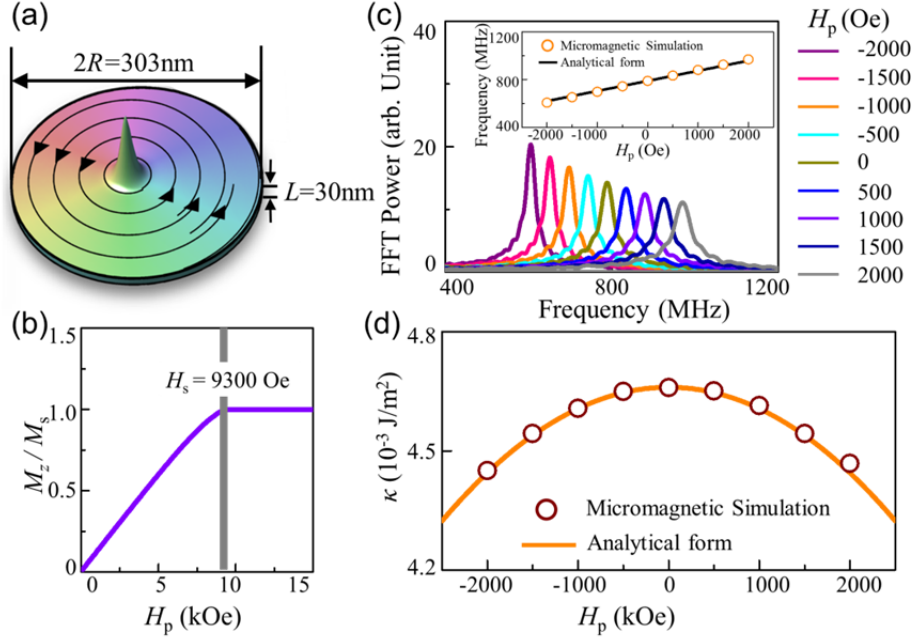


**FIG. 6.1** (a) Geometrical configuration of a vortex-state disk of diameter  $2R$ , thickness  $L$  with upward core magnetization and counter-clockwise (CCW) in-plane curling magnetization. The colors and heights represent the local in- and out-of-plane magnetization components, respectively. (b) Hysteresis curve of  $M_z/M_s$  under perpendicular bias fields of indicated strength  $H_p$ . (c) FFT power spectra for different  $H_p$  values, obtained from FFTs of vortex core positions over  $t=0-1000\text{ns}$  range.

## 6.2 Dipolar interaction and interaction integrals under the influence of perpendicular bias field

We next turn to the coupled vortex pair system under the influence of perpendicular bias field. For the case of coupled vortex oscillator system, not only the gyrovector  $G$  and stiffness coefficient  $\kappa$ , but also the interaction integrals[43], which represent the strength of the dipolar coupling between disks, can be affected by the applied field. To investigate the effect of perpendicular field on the dipolar interaction energy and interaction integral, we start from the magnetostatic interaction between two magnetic elements with nonuniform magnetization distributions  $\mathbf{M}(\mathbf{r})$ , in general, which can be expressed in terms of two different fictitious magnetic charges, a magnetic volume charge,  $\rho(\mathbf{r}) = -M_s \nabla \cdot \mathbf{m}(\mathbf{r})$  and surface charge  $\sigma(\mathbf{r}) = M_s \mathbf{n} \cdot \mathbf{m}(\mathbf{r})$ , as follow[86] :

$$W_{\text{int}} = \int dV dV' \frac{\rho(\mathbf{r}_1) \rho'(\mathbf{r}_2)}{|\mathbf{r}_1 - \mathbf{r}_2|} + \int dS dS' \frac{\sigma(\mathbf{r}_1) \sigma'(\mathbf{r}_2)}{|\mathbf{r}_1 - \mathbf{r}_2|} \quad (6.1)$$

Here,  $\mathbf{m} = \mathbf{M}/M_s$  is the magnetization unit vector,  $\mathbf{n}$  is the unit vector normal to the surface of elements,  $M_s$  is the saturation magnetization. The  $\mathbf{r}_{1,2}$  is radius vector in the local frames of the first and second elements. For the case of a vortex-state disk, the magnetic charges can be calculated through the two different magnetic configuration models: ‘‘rigid vortex model’’,

describing the static susceptibility and “side-surface charge free model” assuming the magnetization structure with no surface magnetic charges on the cylinder side. For the calculation of the magnetic charges, we employed, here, the *surface-charge free model*, because it is known that the surface-charge free model, in general, returns more a realistic value than the rigid vortex model. Then, the magnetization distribution  $\mathbf{m}(x,y)$  at  $H_{\text{perp}}=0$  are given by

$$m_z = p(1 - w\bar{w})/(1 + w\bar{w}), \quad m_x + im_y = 2w/(1 + w\bar{w}) \quad (6.2)$$

Here, the  $w$  is given by  $w(\zeta, \bar{\zeta}) = f(\zeta)/f(\bar{\zeta})$  with  $f(\zeta) = -iC(\zeta - s)(\bar{s}\zeta - 1)/c(1 + |s|^2)$ , where  $C$  is the chirality,  $p$  is the polarization,  $\zeta = (x + iy)/R$ , and  $x$  and  $y$  are Cartesian coordinates in the cylinder plane. The real parameter  $c = R_c/R$  is the reduced radius of vortex core. The displacement of the vortex core from its equilibrium position, here the centre of disks, is described by a complex parameter  $s = s_x + is_y$ , where  $s_x$  and  $s_y$  are the coordinates for vortex core position in the units of disk’s radii  $R$ [84].

For the present model, the coupling between disks can be represented as the sum of contributions from the volume and face-surface magnetic charges. Because the face surface charges are mainly induced from small size of the vortex core region, the contribution of the face-surface charges to magnetostatic energy is usually ignorable, hence, Eq. (6.2)

can be simplified as  $m_z = 0$  and  $m_x + im_y = w$ . In the presence of perpendicular field, the magnetization component  $m_z$  linearly which increases with increasing perpendicular field strength, but in-plane magnetization components  $m_x$  and  $m_y$  decreases, as shown in FIG. 6.1(b). Then, the field evolution of out-of- and in-plane component of magnetization in each disk can be approximately expressed as  $m_z = (H_p/H_s)$ ,  $m_x + im_y = 2\sqrt{1-(H_p/H_s)^2} w$ . According to that, the magnetic volume charge, defined as  $\text{div}\mathbf{m} = \partial w/\partial\zeta$ , can be simply given by  $\text{div}\mathbf{m}(x, y) = 2C\sqrt{1-(H_p/H_s)^2} (s_x y - s_y x)/|\zeta|$  for small oscillation amplitude regime. By inserting this into Eq. (6.1), one can obtain the dipolar interaction energy between two vortex-state disks in the form of

$$W_{\text{int}}(s_x, s_y, s_{x'}, s_{y'}) = 2C_1 C_2 \left[ 1 - (H_p/H_s)^2 \right] (\eta_{\parallel} s_x s_{x'} - \eta_{\perp} s_y s_{y'}) \quad (6.3)$$

where  $\eta_{\parallel} = M_s^2 R^3 \int (\sin\varphi \sin\varphi')/|\mathbf{r}_1 - \mathbf{r}_2| dV dV'$  and  $\eta_{\perp} = M_s^2 R^3 \int (\cos\varphi \cos\varphi')/|\mathbf{r}_1 - \mathbf{r}_2| dV dV'$ . Accordingly, the interaction integral under the perpendicular bias field can be re-expressed as  $\eta_{\parallel}(H_p) = \eta_{\parallel}(0) [1 - (H_p/H_s)^2]$ ,  $\eta_{\perp}(H_p) = \eta_{\perp}(0) [1 - (H_p/H_s)^2]$ .

### 6.3 Normal modes in two coupled vortex oscillator under the influence of perpendicular bias field

On the basis of above results, we analytically derive the angular eignefrequency of two coupled vortex oscillator under the influence of the perpendicular bias field. The normal modes for coupled vortex oscillator can be obtained from linearized Thiele equations taking into account the potential energy modified by dipolar interaction between disks. The corresponding force-balance equation for the  $n^{\text{th}}$  disk is given as

$$-\mathbf{G}_n \times \dot{\mathbf{X}}_n - \hat{D}_n \dot{\mathbf{X}}_n + \partial W_n / \partial \mathbf{X}_n = 0 \quad (6.4)$$

where  $\mathbf{X}_n = (X_n, Y_n)$  is the core position vector in the  $n$ th disk, i.e., for two coupled vortex oscillators,  $n=1$  and  $2$ , based on the collective coordinate ansatz.  $\mathbf{G}_n = -G_n p_n \hat{\mathbf{z}}$  is the gyrovector with its constant,  $\hat{D}_n = D_n \hat{I}$  is the damping tensor with the identity matrix  $\hat{I}$  and the damping constant  $D_n$ [102]. The  $p_n$  represents the vortex core polarization in the  $n$ th disk. The total potential energy is given as  $W = W(0) + \sum_{n=1} \frac{1}{2} \kappa_n |\mathbf{X}_n|^2 + W_{\text{int}}$ , where  $W(0)$  is the potential energy for  $\mathbf{X}_n=(0,0)$ , the second term is that for off-centered vortex core with the stiffness coefficient  $\kappa_n$  for isolated  $n$ th disk, and the  $W_{\text{int}}$  is the dipolar interaction energy between neighbouring disks as noted in Eq. (6.4).

We stress here that the parameters in Thiele equation, i.e.,  $G$  and  $\omega_0$ , respond quite differently to the perpendicular bias field in an isolated disk depending on the relative orientation of the vortex-core magnetization in the applied field direction. This result leads to the contrasting behaviours reliant to the relative polarization between NN disks in the pair or chains of coupled-vortex oscillators. Figure 6.2 shows the schematic representation of the effect of the relative polarization configuration between NN disks on the coupled-vortex system under the perpendicular bias field. For simplicity, here, we assume that there is no dipolar coupling between NN disks. For  $p_1 p_2 = 1$ , when the perpendicular bias parallel (anti-parallel) to vortex-core magnetization is turned on, the eigenfrequency in the both disks is raised (lowered) to the same value [see FIG. 6.2(b)]. Whereas,  $p_1 p_2 = -1$ , the eigenfrequency is raised (lowered) for the disk with  $p$  parallel (anti-parallel) to the applied field direction. Then, though any dipolar-coupling between disks is not taken into account, the eigenfrequency (black solid lines) splits into two, solely due to the perpendicular field. This indicates that, for the case of antiparallel polarization ordering, the perpendicular field can lift the degeneracy of states. Accordingly, the system can be treated as the 1D arrays consisting of bi-component constituents.

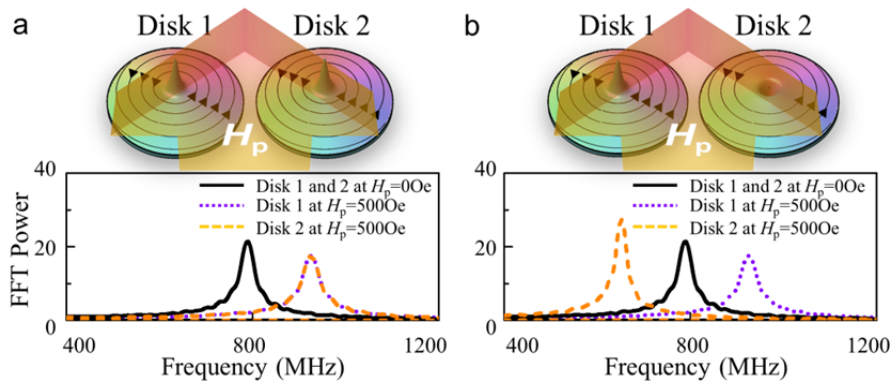


**FIG. 6.2** Schematic representation of contrasting response to the perpendicular bias field in the coupled-vortex system for parallel (a) and anti-parallel (b) polarization configurations.

Based on the results, we now analyze the coupled-vortex oscillation according to the  $p$  ordering, i.e., parallel polarization and antiparallel polarization.

First, for the case of parallel polarizations, since two identical disks has the same values of  $G$  and  $\kappa$  under the influence of the perpendicular field, Eq. (6.4) is given by a simple form of  $2 \times 2$  matrix, as reported in Ref.[50]. Then, the angular eigenfrequencies of the coupled vortex oscillation are

$$\text{Re}[\omega_{1,2}(H_p)] = \omega_0(H_p) \left( \sqrt{(1 \pm C_1 C_2 \eta_{\parallel}(H_p)/\kappa(H_p))(1 \mp C_1 C_2 \eta_{\perp}(H_p)/\kappa(H_p))} \right) \quad (6.5)$$

By inserting the field-dependent parameters of Thiele equation into Eq. (6.5), it can be rewritten as

$$\text{Re}[\omega_{1,2}(H_p)] = \omega_0(0) \left( 1 + p H_p / H_s \right) \sqrt{(1 \pm C_1 C_2 \eta_{\parallel}(0)/\kappa(0))(1 \mp C_1 C_2 \eta_{\perp}(0)/\kappa(0))} \quad (6.6)$$

This explicit analytical form shows that the angular eigenfrequency of coupled vortex oscillator under the influence of the perpendicular field is proportional to that of isolated disk. Accordingly, the angular frequency difference  $\Delta\omega_{1,2}$ , defined as  $\text{Re}(\omega_1) - \text{Re}(\omega_2)$ , for  $p_1 p_2 = 1$ , can be expressed as

$$\Delta\omega_{1,2}(H_p) = \Delta\omega_{1,2}(0) \left( 1 + p H_p / H_s \right) \quad (6.7)$$

For the case of anti-parallel polarization, as describe in above, the system has two different degrees of freedom. Then, the general solutions of

the system can be expressed in terms of  $X_{1,2} = \bar{X}_{1,2}e^{i\omega t}$ ,  $Y_{1,2} = \bar{Y}_{1,2}e^{i(\omega t - p_1\pi/2)}$ .

Taking into account the general solution, one can rewrite the force-balance equation into

$$\begin{bmatrix} -D_1i\omega + \kappa_1 & -p_1|G_1|i\omega & C_1C_2\eta_{\parallel} & 0 \\ p_1|G_1|i\omega & -D_1i\omega + \kappa_1 & 0 & -C_1C_2\eta_{\perp} \\ C_1C_2\eta_{\parallel} & 0 & -D_2i\omega + \kappa_2 & -p_2|G_2|i\omega \\ 0 & -C_1C_2\eta_{\perp} & p_2|G_2|i\omega & -D_2i\omega + \kappa_2 \end{bmatrix} \begin{bmatrix} \bar{X}_1 \\ \bar{Y}_1 \\ \bar{X}_2 \\ \bar{Y}_2 \end{bmatrix} = \begin{bmatrix} 0 \\ 0 \\ 0 \\ 0 \end{bmatrix} \quad (6.8)$$

Using the condition that the determinant of the  $4 \times 4$  matrix is zero, and assuming zero damping constant, the angular eigenfrequency for antiparallel  $p$  ordering, is given by

$$\text{Re}[\omega(H_p)] = \sqrt{\delta_1(H_p) \mp \delta_2(H_p)} \quad (6.9)$$

$$\delta_1(H_p) = \omega_0^2 \left\{ \left[ 1 + (H_p/H_s)^2 \right] + \left[ \eta_{\parallel}\eta_{\perp} \left\{ 1 - (H_p/H_s)^2 \right\} \right] / \kappa_0^2(0) \right\}$$

Then, angular frequency difference  $\Delta\omega_{1,2}$ , for  $p_1p_2=-1$ , is

$$\Delta\omega_{1,2}(H_p) = \left| \sqrt{\delta_1(H_p) + \delta_2(H_p)} - \sqrt{\delta_1(H_p) - \delta_2(H_p)} \right| \quad (6.10)$$

The upper panel of FIG. 6.3 shows the angular frequency difference of two coupled vortex oscillator according to  $H_p$ , as obtained from the micromagnetic simulations (open circle) and analytical calculations (solid lines) of Eqs. 6.7 (for  $p_1p_2=1$ ) and 6.10 (for  $p_1p_2=-1$ ). The analytical results are in a good agreement with the micromagnetic simulation results for both  $p$  ordering. For  $p_1p_2=1$ , the values of  $\Delta\omega$  linearly increase with increasing  $H_p$ , while those for  $p_1p_2=-1$  increases with increasing  $|H_p|$  as a parabolic shape.

We note that the energy exchange rate  $\tau_{\text{ex}}$  between coupled vortex oscillators, defined as the time period required for transferring the potential energy stored in a disk completely to the adjacent disk, and is inversely proportional to  $\Delta\omega$  [51]. This means that the  $\tau_{\text{ex}}$ , one of the most essential factors in information-signal processing, can be manipulated by means of the bias field. To verify this, we plotted  $\tau_{\text{ex}}$  vs.  $H_p$  (lower panel in FIG. 6.3). The solid lines and open circles correspond to the analytical calculation and micromagnetic simulation results, respectively, as obtained from the explicit form of  $\tau_{\text{ex}} = \pi/\Delta\omega$ . The inverted triangles indicate the micromagnetic simulation results extracted from a characteristic periodicity of temporal oscillation of vortex displacement in a left disk. Both results as obtained from micromagnetic simulations and the analytical calculations were found to be in perfect agreement. For  $p_1 p_2 = 1$ , the  $\tau_{\text{ex}}$  is inversely proportional to  $H_p$ , while, for  $p_1 p_2 = -1$ , the value of  $\tau_{\text{ex}}$  which is at maximum for  $H_p = 0$  decreases with increasing  $|H_p|$ . Accordingly, for both  $p$  orderings, we can obtain higher signal transfer speed as increasing  $H_p$ .

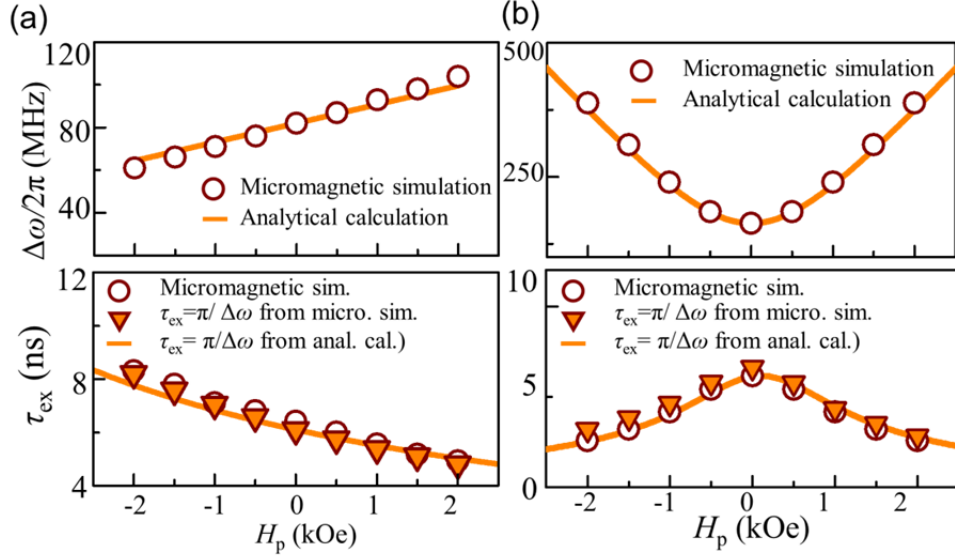


**FIG. 6.3** The angular frequency difference  $\Delta\omega$  (top panel) and the energy exchange rate  $\tau_{ex}$  (bottom panel) in dipolar-coupled two vortex oscillator as a function of the strength of perpendicular bias field, for parallel (a) and antiparallel (b) polarization ordering. The solid lines and open circles correspond to the analytical calculation and micromagnetic simulation results, respectively, as obtained from the explicit form of  $\tau_{ex} = 1/\Delta\omega$ . The inverted triangles indicate the  $\tau_{ex}$  directly extracted from a characteristic periodicity of temporal oscillation of vortex displacement in a left disk.

## 6.4 Dispersion relation of 1D arrays of coupled vortex oscillators under the influence of perpendicular bias field

Using the analysis described in detail in Ref. [99] and [100], one can derive the dispersion relation of 1D arrays of vortex-state disks under the perpendicular bias field with parallel and antiparallel  $p$  ordering, respectively. Taking into account the field-dependent parameters, the dispersion relation can be given by

$$\omega^2(k, H_p) = \omega_0^2(0)[1 + p(H_p/H_s)]^2 \zeta_{\parallel}^2(k, H_p) \zeta_{\perp}^2(k, H_p) \quad (6.11) \text{ with}$$

$$\zeta_{\parallel}^2 = 1 + 2C_n C_{n+1} (\eta_{\parallel}(0)/\kappa_0(0)) \cos(ka) \quad \text{and} \quad \zeta_{\perp}^2 = 1 - 2C_n C_{n+1} (\eta_{\perp}(0)/\kappa_0(0)) \cos(ka)$$

for parallel  $p$  ordering, and

$$\omega^2(k, H_p) = \xi_0(k, H_p) \mp \Delta\xi(k, H_p) \quad (6.12) \text{ with}$$

$$\xi_0(k, H_p) = \omega_0^2(0) \left[ \left[ 1 + (H_p/H_s)^2 \right]^2 + 2\eta_{\parallel}(0)\eta_{\perp}(0) \left\{ \left[ 1 - (H_p/H_s)^2 \right] / \kappa_0^2(0) \right\} (\cos 2ka + 1) \right]$$

and

$$\Delta\xi(k) = \omega_0^2(0) \left[ \begin{aligned} & 4(H_p/H_s)^2 + 2\{[1 + (H_p/H_s)]\eta_{\parallel} + [1 - (H_p/H_s)]\eta_{\perp}\} \times \\ & \left\{ [1 - (H_p/H_s)]\eta_{\parallel} + [1 + (H_p/H_s)]\eta_{\perp} \right\} \left\{ \left[ 1 - (H_p/H_s)^2 \right] / \kappa_0^2(0) \right\} (\cos 2ka + 1) \end{aligned} \right]^{1/2}$$

for antiparallel  $p$  ordering.

From fast Fourier transformations (FFTs) of the temporal oscillations of the core positions (here the  $x$  components) in all of the disks, we obtained the power spectra of dispersions (i.e., the  $f$ - $k$  relation) of 1D

arrays of vortex-state disks with two different polarization ordering,  $p_n=1$  and  $(-1)^{n+1}$ , as shown in FIG. 6.4 (a) and 6.4(b), respectively. The dispersion relations as obtained from the explicit analytical forms for two different polarization ordering are displayed by the white lines. Those analytical calculation results are in excellent agreement with the dispersion spectrum from micromagnetic simulation except for the intensity of each mode. The band widths were wider for  $p_n=(-1)^{n+1}$  than for  $p_n=1$  at  $H_p=0$ , due to the stronger dipolar coupling between NN for antiparallel than parallel  $p$  ordering case. The general shape of the branches at  $H_p=0$  is concave up (down) for parallel (antiparallel)  $p$  ordering for the same chirality configuration. In the presence of perpendicular bias field, the position and width of a single branch monotonically increase with the increasing  $H_p$ , for  $p_n=1$ . By contrast, for the case of  $p_n=(-1)^{n+1}$ , a single branch splits into two distinct branches at non-zero  $H_p$ , analogous to those for 1D arrays of vortex-state disks comprised of alternating materials[100]. This splitting is due to contrasting response to the relative orientation of the vortex-core magnetization in the applied field direction, as described in the previous section. The band structures for antiparallel  $p$  ordering are symmetric with respect to the sign of the bias field. The band gap between two branches increases with increasing the strength of the bias field,  $|H_p|$ . This result provides an efficient way for dynamic control of collective vortex gyration.

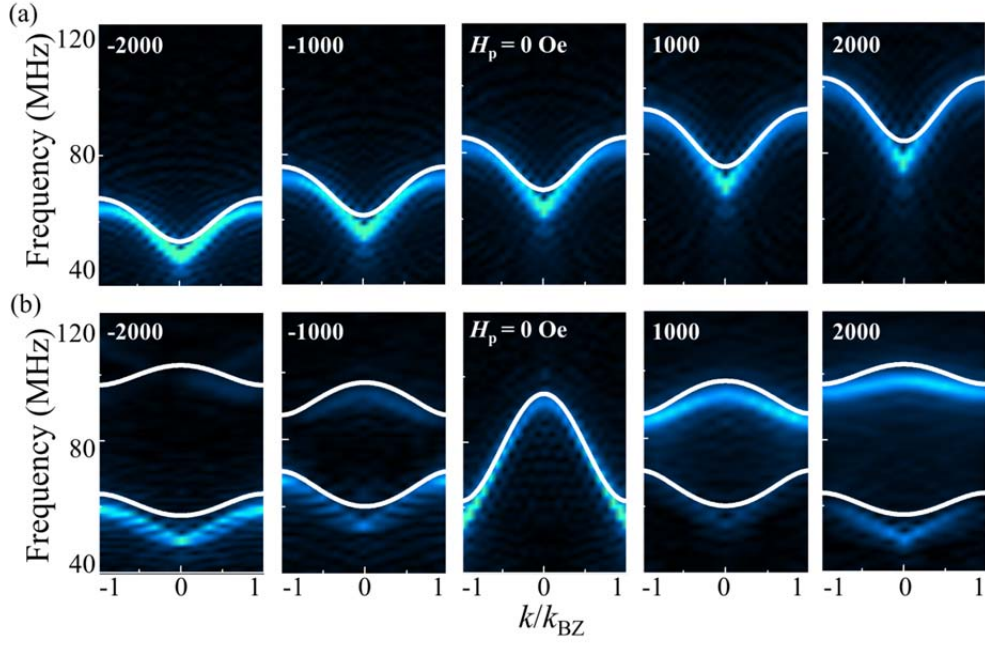


**FIG. 6.4** Dispersion relations for 1D arrays of vortex-state disks as a function of perpendicular field strength with (a) parallel and (b) antiparallel polarization ordering, as obtained from the FFTs of the numerically calculated vortex-core position vectors  $\mathbf{X}_n$ , for which core gyration is excited in the center disk of the array. The white line indicates the analytical form of Eq. 6.9 and 6.10.

## Chapter 7

### Summary

In this thesis, we investigated the collective vortex-gyration in dipolar-coupled 1D arrays of magnetic disks with the help of the state-of-the-art time-resolved full-field magnetic transmission soft X-ray microscope, scanning transmission x-ray microscopy, micromagnetic simulation, and analytical derivation.

In the first part, we experimentally observed the wave modes of collective vortex-core gyration excitation along with their quantization and their dispersions in the array of five coupled disks. By means of analytical derivation, numerical calculation of coupled Thiele equation and micromagnetic simulation, we found that those discrete modes can be explained in terms of the relative orientations of rotating effective in-plane magnetizations and the dynamic dipolar interaction between the individual disks. Furthermore, additional degrees of freedom of vortex-state ordering, including polarization and chirality, dramatically affect the phase relation of the dynamic dipolar interaction, thereby leading to changes in dispersion.

In the second part, we studied the effects of various lattice bases of 1D vortex arrays on collective vortex-gyration dispersion. As a result, it was found that the resultant band structures and gaps were characteristic and

controllable by employing alternating constituent materials and alternating dimensions of a single material. Accordingly, and promisingly, the propagation property of the coupled gyrations can be manipulated by the selection of constituent materials, the vortex-state ordering, the dimensions of each disk, as well as the NN disks' separation distance.

In the last part, we investigated the effect of perpendicular bias field on collective vortex gyration modes in 1D arrays of magnetic disks. The study reveals that the interaction coefficients and characteristic parameters for the magnetic vortex dynamics are controllable by the strength as well as direction of the perpendicular field. More interestingly, for the case of antiparallel polarization ordering, a single branch splits into two different branches, and thus band gap opening occurs under the influence of the perpendicular bias field. This substantial work provide methods for dynamic manipulation of the dispersion relation in vortex-state-disk-array magnonic crystals as well as the signal transfer speed through the coupled-vortex gyration.

This work on 1D magnonic crystal of coupled vortices constitutes a milestone towards the practical achievement of this new class of MCs harnessing their advantages and opens a way in the signal processing device with the advantages of low-power consumption, and dynamically controllable states.

## Appendix

### A. Experimental Setup

#### A.1 Thin film deposition

The deposition of multilayer of magnetic thin film are prepared by using a cluster chamber system consisting of 4 E-beam evaporation sources (EFM4, Omicron), 7-gun metal sputtering sources (A320, AJA international Inc.), 1 RF sputtering source, and a pulsed laser deposition chamber (PLD). In the load-lock chamber, two 2-inch wafer and two piece types of samples can be loaded at the same time. In typical processes, metallic thin films, such as Py, Cu, CoFeB, and CoFe, are prepared in DC magnetron sputtering UHV chamber with a base pressure below of  $3 \times 10^{-9}$  Torr and partial pressure of 1m Torr of Ar. The film thickness can be controlled by manipulating deposition time, DC power, and distance between targets to substrates. The physical properties of the deposited films can be monitored by using X-ray reflectivity measurement (X'pert Pro, PANalytical) and *in-situ* magneto-optical Kerr effect (MOKE) measurement system installed on the e-beam evaporator chamber.

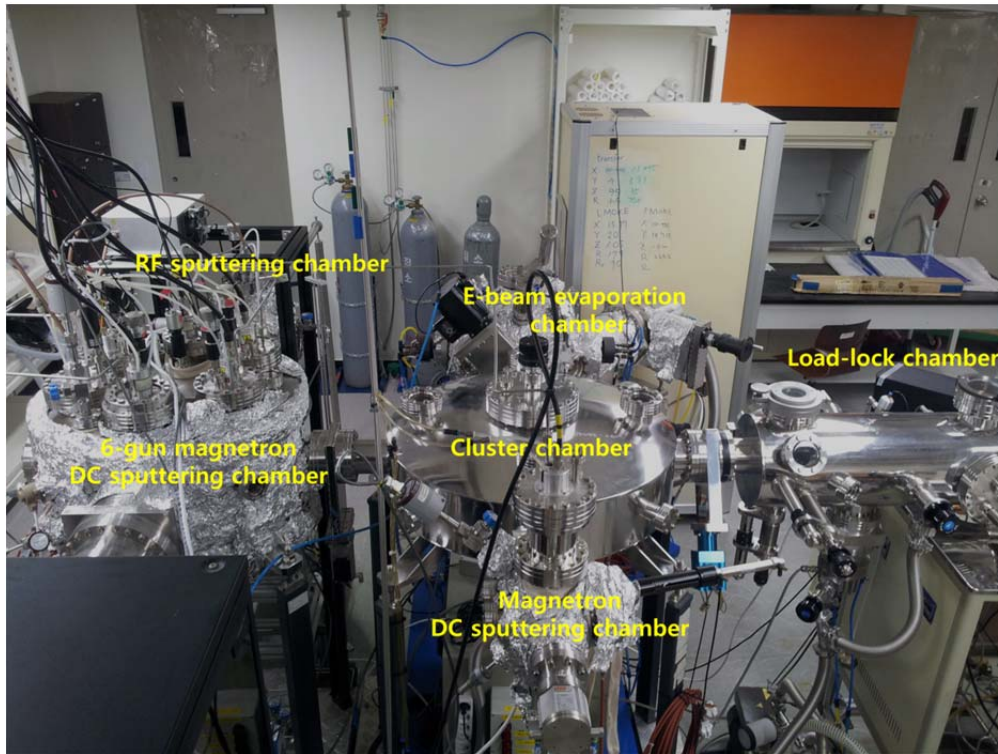


**FIG A.1** Photograph of the experimental setup of the deposition of magnetic thin films.

## A.2 Lithography

Typical patterning processes are carried out at Korea Advanced Nano Fab Center (KANC) in Suwon, Gyeonggi, South Korea. Magnetic elements and electrodes are fabricated by means of photolithography (Mask aligner EVG620, EVG), electron-beam lithography (JBX6000, Jeol) and lift-off processes. Photolithography is primarily used before electron-beam lithography process to draw alignment markers and electrode pads whose sizes are on the order of hundreds of micrometers. In the optical lithography process, a photomask glass coated with chrome, which are responsible for the casting of shadow during exposure, is used for a patterning mask. The mask aligner with UV lamp power of 500W allows a minimum line width of  $0.7\sim 1.0\mu\text{m}$  and align accuracy of  $0.5\mu\text{m}$ . The electron-beam lithography is used for small patterned disks and electrodes. Table 1 shows typical electron beam lithography and lift-off process for the disk-shaped patterning. A bilayer resist technique is used to achieve undercut profile that improves the metal liftoff. For the micron-sized disk patterning, for example, we use LOR1A (Micro. Chem. Corp.) and PMMA A3 950K (Micro. Chem. Corp.) as bottom and top resist layers, respectively. The LOR1A dropped onto a wafer is spin coated at a speed of 2000 rpm during 40 seconds, and soft-baked on hot plate at  $190^{\circ}\text{C}$  to dry off solvents in the resist. The top resist

layer of PMMA 950K A3 is coated on LOR1A resist at 3000rpm during 40 seconds, and baked at 170°C. Electron-beam exposure process is carried out with JBX600 which operates at 50kV and provides electron beam currents from 100pA to 5nA. The dosage of exposure is predetermined by the dosage test; the patterning process is repeated several times varying size of patterns and dosage of exposure, and then the most suitable patterning conditions can be obtained through inspection in scanning electron microscopy. After exposure, the sample is immersed in a developer to dissolve the fragments. Methyl isobutyl ketone (MIBK)/isopropyl alcohol (IPA) solution is used as developer for PMMA. We vary the concentration of the solution depending on the dimension of patterns, i.e., we use MIBK:IPA=1:3 solution with lower concentration for the fabrication of narrow patterns. The sample in a developer is rinsed in IPA, followed by blowing with N<sub>2</sub> gas. AZ300MIF (AZ Electronic Materials USA Crop.) is used to dissolve the LOR1A resist, and de-ionized (DI) water is used for rinsing the sample. Magnetic thin films are deposited on the patterned resists through magnetron DC sputter and electron evaporators. After metal deposition, the deposited sample is lift-offed in acetone and AZ300MIF. Figure A.2, for example, shows scanning electron microscope (SEM) and transmission electron microscopy (TEM) images of the sample as prepared following the procedure in Tabel A.1.

Step #	Description	Equipment	Parameter	Time
<b>1</b>	<b>RESIST COATING : Bilayer- LOR 1A/ PMMA 950K A3 (150nm)</b>			
1.1	LOR 1A	Spin coater	2000RPM	40 sec
1.2	Soft bake	Hot plate	190°C	300 sec
1.3	Cooling	in air		5 min
1.4	PMMA 950K A3	Spin coater	3000RPM	40 sec
1.5	Soft bake	Hot plate	170°C	300 sec
1.6	Cooling	in air		5 min
<b>2</b>	<b>E-BEAM WRITING : Dot</b>			
2.1	Exposure	JBX6000	850 $\mu$ C/cm <sup>2</sup> , 50kV	
2.2	Develop : (MIBK : IPA =1:3)	in wet bench		2 min
2.3	Rinse IPA	in wet bench		30 sec
2.4	N <sub>2</sub> blow			
2.5	Develop : AZ 300MIF	in wet bench		10 sec
2.6	Rinse DI water	in wet bench		30 sec
2.7	N <sub>2</sub> blow			
2.8	Inspection	Optical Microscope		
<b>3</b>	<b>METAL DEPOSITION</b>			
3.1	E-beam evaporation	DC Sputter		
<b>4</b>	<b>Lift-off</b>			
4.1	Acetone	in wet bench		1hr
4.2	Rinse IPA	in wet bench		30 sec
4.3	N <sub>2</sub> blow			
4.4	AZ300MIF	in wet bench		20min
4.5	Rinse DI water	in wet bench		30 sec
4.6	N <sub>2</sub> blow			
4.7	Inspection	Optical Microscope		

**TABLE A.1** A typical electron-beam lithography procedure for a disk-shaped patterning.

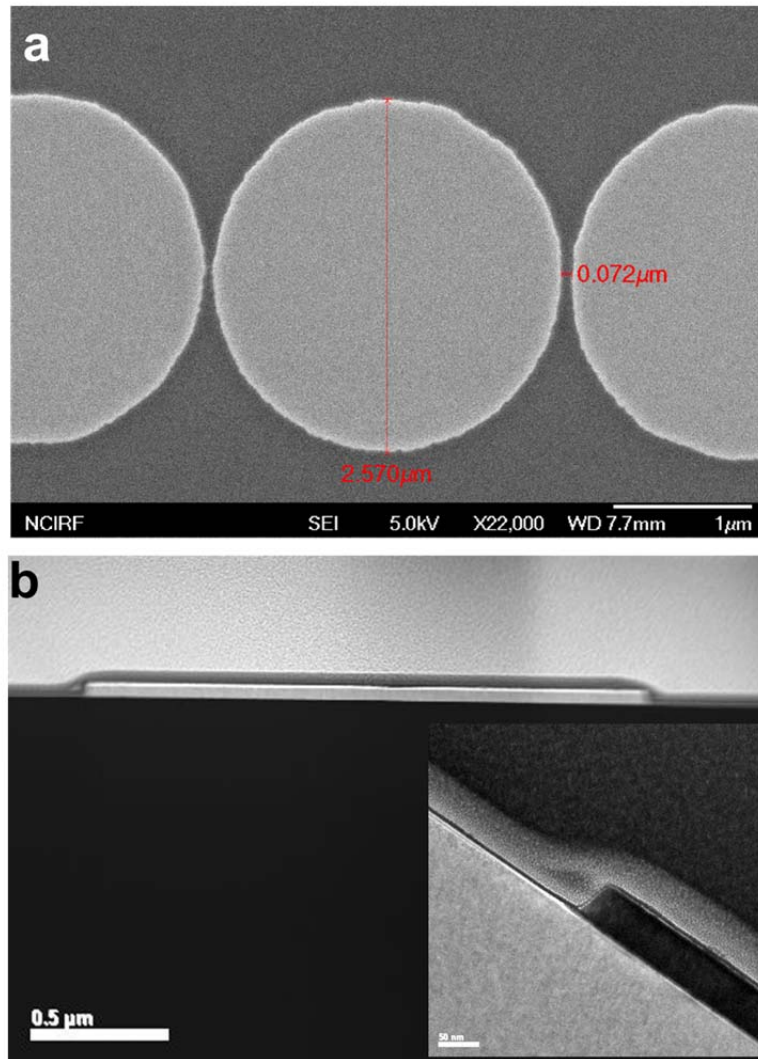


**FIG A.2** (a) Patterned disks of Ni (50nm)/Au (3nm) as observed from a scanning electron microscope (SEM). (b) Transmission electron microscopy (TEM) image of cross-sectional area of patterned disk prepared by focused-ion beam milling.

### **A.3 Electrical measurement setup**

For the measurement of electrical signal in magnetic materials, we set up all-electrical spin dynamics spectroscopy system. The measurements are performed in a modified probestation (MS Tech, MST 8000C) [See FIG. A.3]. The probe station consists of electromagnets connected to DC power supply, DC and RF probes, DC to broadband microwave electronics, and remote-controlled data acquisition software. The home-made electromagnets provides XY in-plane magnetic field up to  $\sim 10000\text{Oe}$ . The two electromagnets pair are arranged perpendicularly and controlled independently with two different DC power supply (PBZ 40-10, Kikusui) to allow application of H at an arbitrary in-plane angle. Water cooling pads are attached onto the electromagnets to cool down the heated electromagnets. Two DC probes and four RF probes can be used to contact to devices at the same time. The probes have bandwidth of dc $\sim$ 500MHz (GGB Industries, Model 12C) or dc-40GHz (GGB Industries, customized for the probestation). The probes are connected to the electronics as follows: a sourcemeter (Sourcemeter 2400, Keithley Instruments Inc.), two real-time oscilloscopes (DSO-X 4104A and DSO91304A, Agilent Tech.), a vector network analyzer (PNA E8362C Agilent Tech.), a lock-in amplifier (SR830 DSP Lock-In Amplifier, Stanford Research Systems), an arbitrary function generator (81150A, Agilent Tech.), and a signal generator (E8257D Agilent

Tech.) [See FIG. A.4].. Each electronics is connected via 50ohm impedance matched RF coaxial cables (BNC terminated for DC to 4GHz, SMA for DC to 18GHz, and 2.92mm SMK for DC to 46GHz). An automatic data acquisition and remote control of electronics run on PC equipped with a GPIB interface card, a serial bus (RS232), and with the LabView 2010 software installed on the PC.

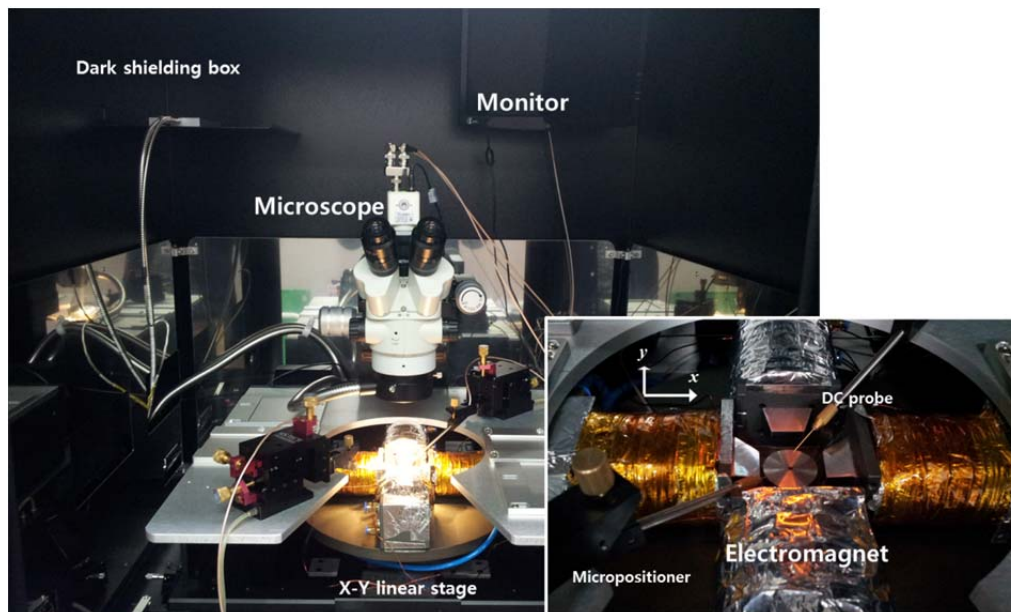


**FIG A.3** Photograph of the experimental setup of a probe station.

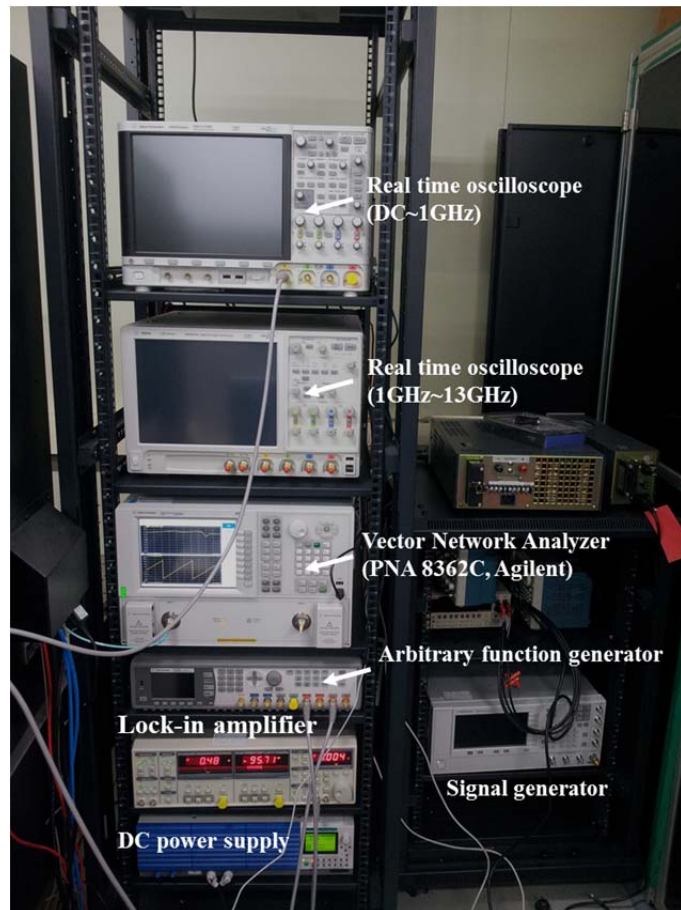


**FIG A.4** Photograph of DC and microwave electronics in a lab.

## Bibliography

- [1] V. V. Kruglyak, S. O. Demokritov, and D. Grundler, *Journal of Physics D-Applied Physics* **43**, 264001 (2010).
- [2] S. K. Kim, *Journal of Physics D-Applied Physics* **43**, 264004 (2010).
- [3] M. N. Baibich, J. M. Broto, A. Fert, F. N. Vandau, F. Petroff, P. Eitenne, G. Creuzet, A. Friederich, and J. Chazelas, *Physical Review Letters* **61**, 2472 (1988).
- [4] P. M. Levy, S. F. Zhang, and A. Fert, *Physical Review Letters* **65**, 1643 (1990).
- [5] M. Julliere, *Physics Letters A* **54**, 225 (1975).
- [6] T. Miyazaki and N. Tezuka, *Journal of Magnetism and Magnetic Materials* **139**, L231 (1995).
- [7] J. C. Slonczewski, *Journal of Magnetism and Magnetic Materials* **159**, L1 (1996).
- [8] L. Berger, *Physical Review B* **54**, 9353 (1996).
- [9] H. Ohno, *Journal of the Physical Society of Japan* **77**, IV (2008).
- [10] A. Fert, *Thin Solid Films* **517**, 2 (2008).
- [11] S. D. Bader and S. S. P. Parkin, in *Annual Review of Condensed Matter Physics, Vol 1*, edited by J. S. Langer (Annual Reviews, Palo Alto,

2010), pp. 71.

[12] C. Chappert, A. Fert, and F. N. Van Dau, *Nature Materials* **6**, 813 (2007).

[13] W. C. Black and B. Das, *Journal of Applied Physics* **87**, 6674 (2000).

[14] A. Ney, C. Pampuch, R. Koch, and K. H. Ploog, *Nature* **425**, 485 (2003).

[15] M. Hayashi, L. Thomas, R. Moriya, C. Rettner, and S. S. P. Parkin, *Science* **320**, 209 (2008).

[16] S. S. P. Parkin, M. Hayashi, and L. Thomas, *Science* **320**, 190 (2008).

[17] S. S. P. Parkin *et al.*, *Journal of Applied Physics* **85**, 5828 (1999).

[18] J. G. Zhu, Y. F. Zheng, and G. A. Prinz, *Journal of Applied Physics* **87**, 6668 (2000).

[19] J. M. Daughton, *Journal of Magnetism and Magnetic Materials* **192**, 334 (1999).

[20] P. P. Freitas, R. Ferreira, S. Cardoso, and F. Cardoso, *Journal of Physics-Condensed Matter* **19**, 165221 (2007).

[21] S. Neusser and D. Grundler, *Advanced Materials* **21**, 2927 (2009).

[22] A. A. Serga, A. V. Chumak, and B. Hillebrands, *Journal of Physics D-Applied Physics* **43**, 264002 (2010).

[23] S. V. Vasiliev, V. V. Kruglyak, M. L. Sokolovskii, and A. N. Kuchko,

Journal of Applied Physics **101**, 113919 (2007).

[24] A. Khitun, D. E. Nikonov, M. Bao, K. Galatsis, and K. L. Wang, Nanotechnology **18**, 465202 (2007).

[25] K. S. Lee and S. K. Kim, Journal of Applied Physics **104**, 053909 (2008).

[26] A. Khitun, M. Bao, J. Y. Lee, K. L. Wang, D. W. Lee, S. X. Wang, and I. V. Roshchin, Journal of Nanoelectronics and Optoelectronics **3**, 24 (2008).

[27] T. Schneider, A. A. Serga, B. Leven, B. Hillebrands, R. L. Stamps, and M. P. Kostylev, Applied Physics Letters **92**, 022505 (2008).

[28] Y. N. Wu, M. Q. Bao, A. Khitun, J. Y. Kim, A. Hong, and K. L. Wang, Journal of Nanoelectronics and Optoelectronics **4**, 394 (2009).

[29] A. Khitun, M. Q. Bao, and K. L. Wang, Journal of Physics D-Applied Physics **43**, 264005 (2010).

[30] S. K. Kim, K. S. Lee, and D. S. Han, Applied Physics Letters **95**, 082507 (2009).

[31] K. S. Lee, D. S. Han, and S. K. Kim, Physical Review Letters **102**, 127202 (2009).

[32] A. V. Chumak, A. A. Serga, B. Hillebrands, and M. P. Kostylev, Applied Physics Letters **93**, 022508 (2008).

[33] A. V. Chumak *et al.*, Applied Physics Letters **95**, 262508 (2009).

[34] A. V. Chumak, A. A. Serga, S. Wolff, B. Hillebrands, and M. P.

- Kostylev, *Applied Physics Letters* **94**, 172511 (2009).
- [35] J. Ding, M. Kostylev, and A. O. Adeyeye, *Physical Review Letters* **107**, 047205 (2011).
- [36] A. V. Chumak, V. S. Tiberkevich, A. D. Karenowska, A. A. Serga, J. F. Gregg, A. N. Slavin, and B. Hillebrands, *Nature Communications* **1**, 141 (2010).
- [37] A. V. Chumak, V. I. Vasyuchka, A. A. Serga, M. P. Kostylev, V. S. Tiberkevich, and B. Hillebrands, *Physical Review Letters* **108**, 257207 (2012).
- [38] A. D. Karenowska, J. F. Gregg, V. S. Tiberkevich, A. N. Slavin, A. V. Chumak, A. A. Serga, and B. Hillebrands, *Physical Review Letters* **108**, 015505 (2012).
- [39] H. Puzkarski and M. Krawczyk, in *Interfacial Effects and Novel Properties of Nanomaterials*, edited by W. Lojkowski, and J. R. Blizzard (Trans Tech Publications Ltd, Zurich-Uetikon, 2003), pp. 125.
- [40] S. Tacchi, G. Duerr, J. W. Klos, M. Madami, S. Neusser, G. Gubbiotti, G. Carlotti, M. Krawczyk, and D. Grundler, *Physical Review Letters* **109**, 137202 (2012).
- [41] M. Krawczyk, S. Mamica, M. Mruczkiewicz, J. W. Klos, S. Tacchi, M. Madami, G. Gubbiotti, G. Duerr, and D. Grundler, *Journal of Physics D-Applied Physics* **46**, 495003 (2013).
- [42] S. Neusser, G. Duerr, H. G. Bauer, S. Tacchi, M. Madami, G.

- Woltersdorf, G. Gubbiotti, C. H. Back, and D. Grundler, *Physical Review Letters* **105**, 067208 (2010).
- [43] J. Shibata, K. Shigeto, and Y. Otani, *Physical Review B* **67**, 224404 (2003).
- [44] J. Shibata, K. Shigeto, and Y. Otani, *Journal of Magnetism and Magnetic Materials* **272**, 1688 (2004).
- [45] J. Shibata and Y. Otani, *Physical Review B* **70**, 012404 (2004).
- [46] H. Jung *et al.*, *Applied Physics Letters* **97**, 222502 (2010).
- [47] A. Vogel, A. Drews, T. Kamionka, M. Bolte, and G. Meier, *Physical Review Letters* **105**, 037201 (2010).
- [48] A. Barman, S. Barman, T. Kimura, Y. Fukuma, and Y. Otani, *Journal of Physics D-Applied Physics* **43**, 422001 (2010).
- [49] S. Barman, A. Barman, and Y. Otani, *Ieee Transactions on Magnetics* **46**, 1342 (2010).
- [50] K. S. Lee, H. Jung, D. S. Han, and S. K. Kim, *Journal of Applied Physics* **110**, 113903 (2011).
- [51] H. Jung *et al.*, *Scientific Reports* **1**, 59 (2011).
- [52] A. Vogel, M. Martens, M. Weigand, and G. Meier, *Applied Physics Letters* **99**, 042506 (2011).
- [53] A. Vogel, T. Kamionka, M. Martens, A. Drews, K. W. oll, T. Tyliczszak, H. Stoll, B. Van Waeyenberge, and G. Meier, *Physical Review Letters* **106**, 137201 (2011).

- [54] S. Sugimoto, Y. Fukuma, S. Kasai, T. Kimura, A. Barman, and Y. Otani, *Physical Review Letters* **106**, 197203 (2011).
- [55] J. H. Kim, K. S. Lee, H. Jung, D. S. Han, and S. K. Kim, *Applied Physics Letters* **101**, 092403 (2012).
- [56] A. Vogel, A. Drews, M. Weigand, and G. Meier, *Aip Advances* **2**, 042180 (2012).
- [57] H. Jung, Y. S. Choi, K. S. Lee, D. S. Han, Y. S. Yu, M. Y. Im, P. Fischer, and S. K. Kim, *Acs Nano* **6**, 3712 (2012).
- [58] L. D. L. Landau, E. M., *Phys. Z. Sowjetunion* **8**, 1935 (1935).
- [59] W. F. Brown, Jr. , *Micromagnetics* (Wiley, New York, 1963).
- [60] W. Heisenberg, *Zeitschrift für Physik* **38**, 411 (1926).
- [61] S. Chikazumi, *Physics of magnetism* (John Wiley & Sons, Inc., New York, 1964).
- [62] G. T. Rado and J. R. Weertman, *Journal of Physics and Chemistry of Solids* **11**, 315 (1959).
- [63] T. L. Gilbert, *Ieee Transactions on Magnetism* **40**, 3443 (2004).
- [64] A. Wachowiak, J. Wiebe, M. Bode, O. Pietzsch, M. Morgenstern, and R. Wiesendanger, *Science* **298**, 577 (2002).
- [65] M. S. Cohen, *Journal of Applied Physics* **36**, 1602 (1965).
- [66] A. Tonomura, T. Matsuda, J. Endo, T. Arii, and K. Mihama, *Physical Review Letters* **44**, 1430 (1980).
- [67] S. Kasai, P. Fischer, M.-Y. Im, K. Yamada, Y. Nakatani, K.

- Kobayashi, H. Kohno, and T. Ono, *Physical Review Letters* **101**, 237203 (2008).
- [68] T. Shinjo, T. Okuno, R. Hassdorf, K. Shigeto, and T. Ono, *Science* **289**, 930 (2000).
- [69] F. Boust and N. Vukadinovic, *Physical Review B* **70**, 172408 (2004).
- [70] B. A. Ivanov and C. E. Zaspel, *Journal of Applied Physics* **95**, 7444 (2004).
- [71] C. E. Zaspel, B. A. Ivanov, J. P. Park, and P. A. Crowell, *Physical Review B* **72**, 024427 (2005).
- [72] K. W. Chou *et al.*, *Applied Physics Letters* **90**, 202505 (2007).
- [73] K. S. Lee and S. K. Kim, *Applied Physics Letters* **91**, 132511 (2007).
- [74] K. S. Lee and S. K. Kim, *Physical Review B* **78**, 014405 (2008).
- [75] K. Y. Guslienko, B. A. Ivanov, V. Novosad, Y. Otani, H. Shima, and K. Fukamichi, *Journal of Applied Physics* **91**, 8037 (2002).
- [76] L. Giovannini, F. Montoncello, F. Nizzoli, G. Gubbiotti, G. Carlotti, T. Okuno, T. Shinjo, and M. Grimsditch, *Physical Review B* **70**, 172404 (2004).
- [77] J. P. Park and P. A. Crowell, *Physical Review Letters* **95**, 167201 (2005).
- [78] K. Y. Guslienko, A. N. Slavin, V. Tiberkevich, and S. K. Kim, *Physical Review Letters* **101**, 247203 (2008).

- [79] F. G. Aliev, J. F. Sierra, A. A. Awad, G. N. Kakazei, D. S. Han, S. K. Kim, V. Metlushko, B. Ilic, and K. Y. Guslienko, *Physical Review B* **79**, 174433 (2009).
- [80] A. A. Thiele, *Physical Review Letters* **30**, 230 (1973).
- [81] D. L. Huber, *Physical Review B* **26**, 3758 (1982).
- [82] N. A. Usov and S. E. Peschany, *Journal of Magnetism and Magnetic Materials* **118**, L290 (1993).
- [83] K. Y. Guslienko, V. Novosad, Y. Otani, H. Shima, and K. Fukamichi, *Applied Physics Letters* **78**, 3848 (2001).
- [84] K. L. Metlov and K. Y. Guslienko, *Journal of Magnetism and Magnetic Materials* **242**, 1015 (2002).
- [85] A. Y. Galkin, B. A. Ivanov, and C. E. Zaspel, *Physical Review B* **74**, 144419 (2006).
- [86] O. V. Sukhostavets, J. Gonzalez, and K. Y. Guslienko, *Physical Review B* **87**, 094402 (2013).
- [87] S. Jain, V. Novosad, F. Y. Fradin, J. E. Pearson, V. Tiberkevich, A. N. Slavin, and S. D. Bader, *Nature Communications* **3**, 1330 (2012).
- [88] K. Y. Guslienko, K. S. Buchanan, S. D. Bader, and V. Novosad, *Applied Physics Letters* **86**, 223112 (2005).
- [89] K. W. Chou *et al.*, *Journal of Applied Physics* **99**, 08f305 (2006).
- [90] N. Locatelli *et al.*, *Applied Physics Letters* **98**, 062501 (2011).
- [91] G. Schütz, W. Wagner, W. Wilhelm, P. Kienle, R. Zeller, R. Frahm,

- and G. Materlik, *Physical Review Letters* **58**, 737 (1987).
- [92] J. Stohr, H. A. Padmore, S. Anders, T. Stammler, and M. R. Scheinfein, *Surface Review and Letters* **5**, 1297 (1998).
- [93] W. Kuch, *Physica Scripta* **T109**, 89 (2004).
- [94] P. Fischer, T. Eimuller, G. Schutz, P. Guttmann, G. Schmahl, K. Pruegl, and G. Bayreuther, *Journal of Physics D-Applied Physics* **31**, 649 (1988).
- [95] U. Wiesemann, Ph. D, Georg-August-Universitat zu Gottingen, 2003.
- [96] See <http://math.nist.gov/oommf/>
- [97] G. de Loubens *et al.*, *Physical Review Letters* **102**, 177602 (2009).
- [98] A. V. Khvalkovskiy, A. N. Slavin, J. Grollier, K. A. Zvezdin, and K. Y. Guslienko, *Applied Physics Letters* **96**, 022504 (2010).
- [99] D. S. Han *et al.*, *Scientific Reports* **3**, 2262 (2013).
- [100] D. S. Han, H. B. Jeong, and S. K. Kim, *Applied Physics Letters* **103**, 112406 (2013).
- [101] M. W. Yoo, K. S. Lee, D. S. Han, and S. K. Kim, *Journal of Applied Physics* **109**, 063903 (2011).
- [102] K. Y. Guslienko, *Applied Physics Letters* **89**, 022510 (2006).

## Publication List

- (1) **D.-S. Han**, Y.-J. Cho, and S.-K. Kim in preparation  
“Bias field control of N-body vortex oscillation in coupled modes.”
- (2) J. Lee, M.-W. Yoo, **D.-S. Han**, and S.-K. Kim, Phys. Rev. B (submitted)  
“Size-selective resonant excitation of soft magnetic nano-spheres of three-dimensional magnetic vortex”

---

- (3) K.-S. Lee, **D.-S. Han**, and S.-K. Kim, Phys. Rev. Lett. 111, 149702 (2013).  
Reply to Comment on "Physical Origin and Generic Control of Magnonic Band Gaps of Dipole-Exchange Spin Waves in Width-Modulated Nanostrip Waveguide"
- (4) **D.-S. Han**, H.-B. Jeong, and S.-K. Kim, Appl. Phys. Lett. 103, 112406 (2013)  
“Contrasting vortex-gyration dispersions for different lattice bases in one-dimensional vortex arrays”
- (5) **D.-S. Han**, A. Vogel, H. Jung, K.-S. Lee, M. Weigand, H. Stoll, G. Schütz, P. Fischer, G. Meier, and S.-K. Kim, Sci. Rep. (Nature Publishing Group), **3**, 2262 DOI:10.1038/srep02262 (2013)  
“Wave modes of collective vortex gyration in dipolar-coupled-dot-array magnonic crystals”

- 
- (6) Y.-S. Yu, **D.-S. Han**, M.-W. Yoo, K.-S. Lee, Y.-S. Choi, H. Jung, J. Lee, M.-Y. Im, P. Fischer, and S.-K. Kim, Sci. Rep. (Nature Publishing Group) **3** 1301 DOI: 10.1038/srep01301 (2013)  
“Resonant amplification of vortex-core oscillations by coherent magnetic-field pulses”
- 
- (7) J.-H. Kim, K.-S. Lee, H. Jung, **D.-S. Han** and S.-K. Kim, Appl. Phys. Lett. **101**, 092403 (2012)  
“Information-signal-transfer rate and energy loss in coupled vortex-state networks”
- 
- (8) H. Jung, Y.-S. Choi, K.-S. Lee, **D.-S. Han**, Y.-S. Yu, M.-Y. Im, P. Fischer, and S.-K. Kim ACS Nano **6**, 3712 (2012).  
“Logic Operations Based on Magnetic-Vortex-State Networks”
- 
- (9) K.-S. Lee, H. Jung, **D.-S. Han**, and S.-K. Kim J. Appl. Phys. **110**, 113903 (2011).  
“Normal modes of coupled vortex gyration in to spatially separated magnetic nanodisks”
- 
- (10) H. Jung, K.-S. Lee, D.-E. Jeong, Y.-S. Choi, Y.-S. Yu, **D.-S. Han**, A. Vogel, L. Bocklage, G. Meier, M.-Y. Im, P. Fischer and S.-K. Kim, Sci. Rep. (Nature Publishing Group) **1**, 59; DOI:10.1038/srep00059 (2011)  
“Tunable negligible-loss energy transfer between dipolar-coupled magnetic disks by stimulated vortex gyration”
-

---

(11) Y.-S. Yu, K.-S. Lee, H. Jung, Y.-S. Choi, M.-W. Yoo, **D.-S. Han**, M.-Y. Im, P. Fischer, and S.-K. Kim

“Polarization-selective vortex-core switching by tailored orthogonal Gaussian-pulse currents”

⇒ Selected for the Virtual Journal of Nanoscale Science & Technology

[May 30, 2011, Volume 23, Issue 21]

---

(12) D.-E. Jeong, **D.-S. Han** and S.-K. Kim Spin **1**, 27 (2011)

“Refractive index and Snell’s law for dipole-exchange spin waves in restricted geometry”

---

(13) M.-W. Yoo, K.-S. Lee, **D.-S. Han** and S.-K. Kim J. Appl. Phys. **109**, 063903 (2011)

“Perpendicular-bias-field-dependent vortex-gyration eigenfrequency”

---

(14) S.-K. Kim, K.-S. Lee, and **D.-S. Han**, Appl. Phys. Lett. 95, 082507 (2009).

“A giga-hertz-range spin-wave filter composed of width-modulated nanostrip magnonic-crystal waveguides”

⇒ Selected as the cover of the 24 August 2009 issue

⇒ Selected for the Virtual Journal of Nanoscale Science & Technology

[Sep. 7, 2009, Volume 20, Issue 10]

---

---

(15) F. G. Aliev, J. F. Sierra, A. A. Awad, G. N. Kakazei, **D.-S. Han**, S.-K. Kim, V. Metlushko, B. Ilic and K. Y. Guslienko Phys. Rev. B. **79**, 174433 (2009)  
“Spin waves in circular soft magnetic dots at the crossover between vortex and single domain state”

(16) **D.-S. Han**, S.-K. Kim, J.-Y. Lee, S. J. Hermsdoerfer, H. Schultheiss, B. Leven, B. Hillebrands Appl. Phys. Lett. **94**, 112502 (2009)  
“Magnetic domain-wall motion by propagating spin waves”  
⇒ Selected for the Virtual Journal of Nanoscale Science & Technology  
[Mar. 30, 2009, Volume 19, Issue 13]

(17) K.-S. Lee, **D.-S. Han**, and S.-K. Kim, Phys. Rev. Lett. **102**, 127202 (2009)  
“Physical origin and generic control of magnonic band gaps of dipole-exchange spin waves in width-modulated-nanostrip waveguides”  
⇒ Selected for the Virtual Journal of Nanoscale Science & Technology  
[Apr. 6, 2009, Volume 19, Issue 4]

---

(18) S.-K. Kim, S. Choi, K.-S. Lee, **D.-S. Han**, D.-E. Jung, and Y.-S. Choi, Appl. Phys. Lett. **92**, 212501 (2008)  
“Negative refraction of dipole-exchange spin waves through a magnetic twin interface in restricted geometry”

---

## Patent List

- 
- (1) S.-K. Kim , K.-S. Lee, **D.-S. Han**  
“Magnonic crystal spin wave device capable of controlling spin wave frequency”  
Korean Patent No. 10-0947582 (April. 8, 2010).  
PCT/KR2009/002850
- 
- (2) S.-K. Kim, **D.-S. Han**, K.-S. Lee, H. Jung  
자기소용돌이 구조를 갖는 자성 박막을 이용한 신호 전달 소자 및 방법  
Korean Patent No. 10-0141234 (Sep.,17, 2013).
- 
- (3) S.-K. Kim, H. Jung, **D.-S. Han**  
자기소용돌이 네트워크 기반의 논리연산 및 소자  
Korean Patent No. 10-2012-0052378 (May. 2012) (Submitted).
-

## International Conference Presentations

---

- (1) [2009] IEEE International Magnetism Conference (INTERMAG 2009), 04-08 May, 2009, Sacramento, CA, USA

**D.-S. Han**, S.-K. Kim, J.-Y. Lee, S. J. Hermsdoerfer, H. Schultheiss, B. Leven, B. Hillebrands, and S.-K. Kim

“Magnetic domain wall movements by interaction with propagating spin waves”

---

- (2) [2010] 11th Joint MMM/Intermag Conference, 18- 22 Jan., 2010, Washington D.C., USA,

**D.-S. Han**, K.-S. Lee, and S.-K. Kim

“Width-modulated nanostrip magnonic-crystal waveguides.”

---

- (3) [2010] International Conference of AUMS (ICAUMS 2010), 5 - 8 Dec., 2010, Jeju, Korea,

**D.-S. Han**, S.-K. Kim, J.-Y. Lee, S. J. Hermsdoerfer, H. Schultheiss, B. Leven, B. Hillebrands, and S.-K. Kim

“Domain Wall Motions Driven by Propagating Spin Waves”

---

---

(4) [2011] 2nd International workshop on Magnonics, 7 -10 Aug., 2011, Recife, PE, Brazil.

**D.-S. Han**, D.-E. Jeong, and S.-K. Kim

“Vortex gyratons in magnonic crystals of dipolar coupled magnetic nanodisks”

---

(5) [2011] 56th Annual Conference on Magnetism and Magnetic Materials, 30 Oct.–3 Nov. 2011, Scottsdale, Arizona, USA

**D.-S. Han**, D.-E. Jeong, and S.-K. Kim

“Collective vortex-gyration modes in magnonic crystals”

---

(6) [2012] The 19<sup>th</sup> International Conference on Magnetism with Strongly Correlated Electron Systems (ICM), 8-13, July, 2012, Busan, Korea

**D.-S. Han**, K.-S. Lee, H. Jung, and S.-K. Kim

“Vortex-gyration-mediated magnonic crystals”

---

(7) [2013] Magnonics 2013, 4-8 Aug. 2013, Varberg, Sweden.

**D.-S. Han**, A. Vogel, H. Jung, K.-S. Lee, M. Weigand, H. Stoll, G. Schütz, P. Fischer, G. Meier and S.-K. Kim

“Wave modes of collective vortex gyration in dipolar-coupled-dot-array magnonic crystals”

---

---

(8) [2013] 58th Annual Conference on Magnetism and Magnetic Materials, 4 – 8, Nov., 2013, Denver, CO, USA.

**D.-S. Han**, A. Vogel, H. Jung, K.-S. Lee, M. Weigand, H. Stoll, G. Schütz, P. Fischer, G. Meier and S.-K. Kim

“One-dimensional magnonic crystals of dipolar coupled vortex lattice”

---

(9) [2013] The 8<sup>th</sup> International Conference on Advanced Materials and Devices, 11-13 Dec., 2013, Jeju, Korea.

**D.-S. Han**, A. Vogel, H. Jung, K.-S. Lee, M. Weigand, H. Stoll, G. Schütz, P. Fischer, G. Meier and S.-K. Kim

“Wave modes of collective vortex gyration in coupled-dot-array magnonic crystals”

---

## Domestic Conference

- 
- (1) [2009] 한국자기학회 2009 년도 임시총회 및 하계학술연구발표회,  
31 May -2 June, 2009, 안면도, 대한민국
- D.-S. Han**, S.-K. Kim, J.-Y. Lee, S. J. Hermsdoerfer, H. Schultheiss, B. Leven, B. Hillebrands, and S.-K. Kim
- “Magnetic domain wall movements by interaction with propagating spin waves”
- 
- (2) [2010] 한국자기학회 2010 임시총회 및 하계학술연구대회, 10-12  
June, 2010, 원주, 대한민국
- D.-S. Han**, K.-S. Lee, and S.-K. Kim
- “Magnonic Band Structures in Two-dimensional Magnonic Crystals of Square-shape Antidot Array”
- 
- (3) [2011] 한국자기학회 2011 임시총회 및 하계학술연구대회, 9 - 11  
June, 2011, 천안, 대한민국
- D.-S. Han**, S.-K. Kim, J.-Y. Lee, S. J. Hermsdoerfer, H. Schultheiss, B. Leven, B. Hillebrands, and S.-K. Kim
- “Interaction between spin waves and domain walls in magnetic nanowires”
-

---

(4) [2012] 한국자기학회 2012 임시총회 및 하계학술연구대회, 24-25

May, 2012, 대전, 대한민국

**D.-S. Han**, A. Vogel, H. Jung, K.-S. Lee, M. Weigand, H. Stoll, G. Schütz,

P. Fischer, G. Meier and S.-K. Kim

“일차원 원판형-자성박막 사슬 구조 내 자기소용돌이-회전운동

모드의 실험적 관측”

---

(5) [2013] 2013 대한금속 재료학회 추계학술대회, 24-25 Oct. 2013, 광주,

대한민국

**D.-S. Han**, A. Vogel, H. Jung, K.-S. Lee, M. Weigand, H. Stoll, G. Schütz,

P. Fischer, G. Meier and S.-K. Kim

“One-dimensional magnonic crystals of coupled vortex lattice”

⇒ Best Poster Award

---

## 국문 초록

고체 내 주기적으로 배열된 원자 및 분자 격자 구조는 각 원자 및 분자간의 상호작용을 통해 집단적인 격자 운동을 가진다. 상기 격자 진동은 고체 내에서 열, 전기 등 운반에 있어서 중요한 요소이다. 유사한 방식으로, 자기소용돌이 자화 구조를 가진 원통형 자성박막이 주기적으로 배열된 구조에서 집단적인 자기소용돌이 회전 운동과 이를 활용한 신호 전달에 관한 연구가 예측되었다. 본 학위 논문은 일차원 강자성 나노 디스크 배열구조에서 자기소용돌이 회전 운동 기반의 마그논 현상을 이론, 전산모사 및 실험을 통해 살펴보고, 이를 바탕으로 자기소용돌이 기반의 마그논 제어 방법을 제시한다.

일차원 강자성 디스크 배열구조에서 자기소용돌이의 집단적 운동 및 과동 모드를 연자기 X-선 현미경을 통해 실험적으로 관측하고, 이를 이론 및 전산모사를 통해 분석한다. 상기 구조 내 자기소용돌이 기반의 마그논 분산 관계는 자기소용돌이 수직 및 수평 자화 성분의 배열 구조, 강자성 나노 디스크의 구조 및 배열 간격 등에 따라 크게 달라진다. 한편, 일차원 격자 구조를 구성하는 기저에 따른 자기소용돌이 기반의 마그논 변화 양상을 전산모사 및 이론을 통해 살펴본다. 이때 단위 격자 기저로 서로 다른 두께, 직경 및 물질로

구성된 두 개의 나노디스크 자성박막을 고려한다. 그 결과, 단일 물질로 구성된 일차원 격자 구조에서 한 갈래의 분산 곡선을 가지는 반면, 두께, 직경 및 물질이 다른 나노디스크 자성박막 격자 구조에서는 두 갈래의 분산 곡선을 가진다. 또한, 두 분산 곡선의 형태 및 두 갈래간의 밴드갭은 기저의 종류에 따라 달라진다.

상기 결과와 더불어, 외부 수직 자기장을 이용한 자기소용돌이 기반의 마그논 특성 제어 방법을 제시하고, 이를 전산모사 및 이론을 통해 구현한다. 상기 결합된 자기소용돌이 회전운동의 주파수 및 분산 관계가 수직 자기장의 세기 및 방향에 따라 크게 의존한다, 특히 자기소용돌이 핵의 자화방향이 반평행한 격자 구조에서는 단일 분산 곡선이 외부 수직자기장에 의해 두 개의 분산 곡선으로 갈라지며 밴드갭이 형성된다..

본 연구 결과는 반영구적으로 자화를 제어하고, 신호를 전달할 수 있으며, 낮은 전력으로 신호를 동작 시킬 수 있는 자기소용돌이 기반의 신호 처리 소자로써의 응용 가능성을 보여준다.

주요어: 자기소용돌이, 자기소용돌이 동역학, 결합된 역학, 스핀동역학, 마그논 결정, 스핀파

학번: 2008-20696

## 감사의 글

부족함을 채우고 싶다는 일념으로 시작한 6 여년간의 대학원 생활이 어느덧 마무리를 향해 간다고 생각하니 많은 아쉬움이 남습니다. 아직 제가 가고자 하는 길에 대한 확신은 서지 않았지만, 연구실 생활을 하면서 배운 경험들은 분명 제 앞으로의 삶에서 큰 힘이 될 것이라고 믿어 의심치 않습니다. 대학원 생활 동안, 즐거운 시간도 있었고 때론 힘들기도 하였지만 이 시간들을 함께 공유한 많은 분들은 항상 저에게 소중한 추억을 남을 것 입니다.

우선 연구실 생활 동안, 부족한 저를 보살펴 주시고 많은 애정을 가지고 지도해주신 김상국 교수님께 감사 드립니다. 학부 시절 처음 연구실에 들어올 때부터 막내라는 이유로 좀 더 많은 관심과 애정을 가져주시고 항상 챙겨주신 점 잊지 않고 있습니다. 또한, 박사과정 동안 연구에 대한 확신이 서지 않을 때, 저에게 용기 주시기 위해 배려해주시는 모습 제가 그 동안 교수님께 표현하지는 못하였지만 항상 감사하게 생각하였습니다. 무엇보다도, 뜻대로 되지 않는 연구과정 속에서 놓치고 있었던 하나님에 대한 믿음을 다시금 붙잡을 수 있는 계기를 마련해 주셔서 감사합니다. 어느 순간부터 제 힘으로 문제를 해결하려고 노력하면서, 가장 중요한 것을 잊고 있었는데 교수님과의

대화를 통해 다시 깨닫게 되는 계기가 되었습니다. 아직 많이 부족하여 때론 교수님 기대에 부응을 못하여 실망을 드리지만 앞으로는 좀 더 나은 모습을 보이는 제자가 될 수 있도록 노력하겠습니다. 바쁘신 시간을 내어 주시고 논문 심사를 해주신 한승우 교수님, 황철성 교수님, 김미영 교수님, 민병철 박사님께도 감사 드립니다. 특히, 이번 졸업실험을 하는데 있어서 도움을 주시기 위해 바쁘신 와중에도 시간을 내주시고, 항상 빌 때마다 좋은 말씀해 주신 민병철 박사님 감사합니다. 박사님께서 주신 말씀들 정말 저에게 많은 도움이 되었습니다.

연구실 생활 동안 함께 동거동락 하였던 많은 선배님들과 후배님들께 감사 드립니다. 저에게는 롤모델 이었던 정대은 박사님, 항상 형을 보면서 항상 부족한 제 자신을 채찍질할 수 있었고, 단편적인 지식이 아닌 근본적인 답을 구하는 방법들을 부족하나마 배울 수 있었습니다. 제 사수이자 연구하는 방법들을 가르쳐주신 이기석 교수님께도 감사 드립니다. 형을 보면서 연구자의 자세를 배울 수 있었습니다. 형과 함께 가까이서 연구를 할 수 있었던 시간들은 저의 연구자로서의 인생에서 정말 소중한 경험이 될 것입니다. 칠부지 막내였던 저에게 애정을 가지고 대해주셨던 유영상 박사님, 형은 존재만으로도 저에게는 정말 든든한 버팀목이었습니다. 감사합니다. 저의 신앙적 멘토인 장재완 박사님. 돌이켜 보면 형과 진욱이와 함께 했던 시간들은 제 대학원 생활의 가장 소중한 시간이었던 것 같습니다.

항상 앞으로도 계속 독실한 신앙으로 승승장구 하는 삶이 있길 기도합니다. 항상 곁에서 세심하게 저를 챙겨주신 정현성 박사님, 말로 표현은 못하였지만 형이 저를 진심으로 챙겨 주시고 아껴주신 점 잊지 않고 있습니다. 은영누나와 함께 평생 행복한 가정 꾸리시길 바랍니다. 항상 유쾌한 바이러스로 연구실 분위기를 이끌어 가셨던 최윤석 박사님, 개인적인 고민까지도 항상 귀 기울여 주시고 신경 써 주신 점 감사합니다. 저의 기숙사 룸메이트였으며, 저에게 진심 어린 충고를 해주셨던 이준영 예비 박사님. 많은 어려움 속에서도 성실함과 우직함으로 헤쳐나간 형의 모습은 정말 저에게 많은 가르침이 되었습니다. 형의 인생에 항상 행복만이 가득하시길 기원합니다. 항상 미소로 대해 주셨던 이제현 박사님, 저에게 항상 많은 도움을 주셨는데 제가 큰 도움을 드리지 못한 것 같아서 아쉽기도 하고 죄송합니다. 그리고 지금은 연구실을 떠나 서로 각자의 길을 가고 있는 작은 윤석형, 종우형, 상국형에게도 감사 드립니다. 특히 작은 윤석형, 종우형과 함께 했던 즐거웠던 기억은 영원히 추억으로 남을 것 같습니다. 조만간 박사가 되실 유명우 예비 박사님, 형의 성실한 모습은 저에게 많은 귀감이 되었습니다. 앞으로도 그 성실함으로 좋은 연구 결과가 있길 기대합니다. 많은 시간을 함께하지는 못하였지만, 잠시나마 연구실에서의 기억을 공유한 진욱이, 인혁이, 태헌이 에게도 감사함을 전합니다. 후배를 대하는데 있어 많이 미숙하여 고생했을 연구실

후배들에게도 감사합니다. 우선 졸업한 지혜와 하연이, 잘 따라줘서 고맙고 많이 잘해주지 못해서 미안하구나. 많이 외롭고 어려울 텐데 곳곳이 잘 하고 있는 민관이, 앞으로도 충분히 잘 헤쳐 나갈 것을 믿는다. 보성이와 준희, 너희들이 연구실에서 정말 수고하고 있는 것을 알고 있단다. 조금 만 더 참고 노력하면 너희들에게 좋은 결과가 있을 것을 확신한다. 앞으로 방장으로 고생할 영준이, 너는 현명하니 조금만 더 노력하면 좋은 연구자가 될 수 있을 거다. 그리고 연구실에 막내로 들어와 고생하고 있는 한별이, 재혁이, 재학이, 앞으로 힘든 일이 있더라도 지금처럼 열심히 하면 충분히 잘 할 수 있을 거라 믿는다.

실험에 많은 도움을 주시고 조언을 아끼지 않으셨던 임미영 박사님, 피터 피셔 박사님께도 감사의 말을 전합니다. 힘든 학위과정을 함께 거친 재료공학부 동기들에게도 감사함과 축하를 보냅니다.

바쁘다는 핑계로 소홀했던 친구들, 동화, 치현이, 두진이, 그리고 윤석이 에게도 감사함을 전합니다. 모두 항상 행복하고 건강하길 기원한다.

항상 나에게 힘이 되는 사랑하는 가족에게 감사함을 전합니다. 항상 걱정과 사랑을 보살펴 주신 부모님 감사합니다. 앞으로 걱정보다는 믿음직스러운 아들의 모습이 될 수 있도록 하겠습니다. 항상 멀리서 응원해준 큰누나, 작은 누나, 매형께도 감사함을 전합니다. 그리고

사랑하는 해림이 에게도 감사함을 전합니다. 지난 4 년 6 개월 동안  
힘들고 즐거웠던 모든 시간을 함께 할 수 있었음에 감사합니다.

일일이 언급하지 못했지만 제게 많은 도움을 주시고 사랑을  
주신 모든 분들께 감사 드립니다.

마지막으로, 무엇보다 지난 6 여년 동안 삶에서 지혜를  
허락해주시고, 좋은 사람들로 주변을 채워주신 하나님께 감사 드립니다.